CERN LINAC4 BEAM DYNAMICS STUDIES AND COMMISSIONING UP TO 12 MeV

by

Veli Yıldız

B.S., Physics, Boğaziçi University, 2008

M.S., Physics, Boğaziçi University, 2011

Submitted to the Institute for Graduate Studies in
Science and Engineering in partial fulfillment of
the requirements for the degree of
Doctor of Philosophy

Graduate Program in Physics
Boğaziçi University
2015

CERN LINAC4 BEAM DYNAMICS STUDIES AND COMMISSIONING UP TO 12 MeV

APPROVED BY:

Assoc. Prof. Erkcan Özcan (Thesis Supervisor)	. . . .
Prof. Metin Arık (Thesis Co-supervisor)	. . . .
Prof. Serkant Ali Çetin	. . . .
Prof. Erhan Gülmez	. . . .
Prof. Tonguç Rador	. . . .
Prof. Teoman Turgut	. . . .

DATE OF APPROVAL: 27.07.2015

ACKNOWLEDGEMENTS

First and foremost, I would like to express my sincere appreciation to my CERN supervisor Alessandra Lombardi who gave me the opportunity to be a part of the Linac4 beam dynamics group. I am deeply grateful for her continuous support and guidance.

I am also thankful to my university supervisors Metin Arık and Erkcan Özcan for having confidence in me and helping me to continue my research on accelerator physics.

I would also like to thank my colleagues Jean-Baptiste Lallement and Piero Posocco for sharing their valuable experience with me and finding time for me whenever I needed their guidance.

Last but not least, I would like to thank all members of the Linac4 team for their pleasant collaboration through which I learned many other aspects of accelerators.

ABSTRACT

CERN LINAC4 BEAM DYNAMICS STUDIES AND COMMISSIONING UP TO 12 MeV

Linac4 is a normal conducting, 160 MeV H$^-$ ions accelerator that is being constructed within the scope of the LHC Injectors Upgrade project. Linac4 will be connected to the Proton Synchrotron Booster during the next long LHC shutdown and it will replace the current 50 MeV proton linac, Linac2.

Linac4 is being commissioned progressively with the installation of the accelerating structures into the Linac4 tunnel. Movable diagnostic benches, with various instruments, are used at each step to allow the detailed characterization of operational parameters that will play a key role in the overall future performance. The first three stages of the commissioning, up to 12 MeV beam energy, were completed by the end of 2014 with a temporary version of the ion source. Using the permanent diagnostic instruments and a movable diagnostic bench, the Low Energy Beam Transport (LEBT) at 45 keV, the Radio Frequency Quadrupole (RFQ) and Medium Energy Beam Transport (MEBT) at 3 MeV, as well as the first tank of the Drift Tube Linac (DTL) at 12 MeV were fully characterized.

ÖZET

LINAC4 DEMET DİNAMİĞİ ÇALIŞMALARI VE 12 MeV ENERJİLİ KISMIN İŞLEME SOKULMASI

Linac4, LHC enjektörlerini geliştirme projesi kapsamında kurulan, H^- iyonlarını 160 MeV'ye kadar çıkaracak bir doğrusal hızlandırıcıdır. Linac4, LHC'nin bir sonraki uzun kapatma süresi sırasında Proton Synchrotron Booster'a bağlanacak ve şu anda kullanılan 50 MeV'lik proton hızlandırıcısı Linac2'nin yerini alacaktır.

Linac4'ün işleme sokulma süreci, hızlandırıcı yapılarının tünele yerleştirilmesi ile paralel bir şekilde devam etmektedir. Her adımda, hızlandırıcının performansı için önemli olacak parametrelerin nitelendirilmesinde, üzerlerinde birçok demet tanı cihazı bulunduran hareketli ölçüm tezgahları kullanılmaktadır. 2012 yılı sonuna kadar, iyon kaynağının geçici bir modeli kullanılarak, 12 MeV'lik kısmın işleme sokulma süreci tamamlanmıştır. Kalıcı demet tanı cihazları ve hareketli bir ölçüm tezgahı üzerinde bulunan tanı cihazları kullanılarak, 45 keV'de Düşük Enerjili Demet Aktarım Hattı, 3 MeV'de Radyo Frekansı Dört Kutuplusu ve Orta Enerjili Demet Aktarım Hattı ve aynı zamanda 12 MeV'de Sürüklenme Tüplü Doğrusal Hızlandırıcı yapısının ilk tankının bütün özellikleri belirlenmiştir.

TABLE OF CONTENTS

LIST OF FIGURES

LIST OF TABLES

LIST OF SYMBOLS/ABBREVIATIONS

$\vec{B}$	Magnetic field
$\vec{E}$	Electric field
$\vec{J}$	Current density
M	Mismatch factor
N_l^{sc}	Number of longitudinal space charge mesh intervals
N_r^{sc}	Number of radial space charge mesh intervals
$\vec{x}$	Position
$\vec{v}$	Velocity
α	One of the beam Twiss parameters
α_{bend}	Angle of deflection
β	One of the beam Twiss parameters
β_r	Relativistic parameter, beta
γ	One of the beam Twiss parameters
γ_r	Relativistic parameter, gamma
ΔE	Energy difference between a particle and the synchronous particle
$\Delta\phi$	Phase difference between a particle and the synchronous particle
ϵ	Emittance
ρ	Charge density

BCT	Beam Current Transformer
BPM	Beam Position Monitor
BSM	Bunch Shape Monitor
CERN	European Organization for Nuclear Research
DESY	Deutsches Elektronen-Synchrotron
DTL	Drift Tube Linac
CCDTL	Cell-Coupled Drift Tube Linac
GUI	Graphical User Interface

LEBT	Low Energy Beam Transport
LHC	Large Hadron Collider
Linac	Linear Accelerator
MEBT	Medium Energy Beam Transport
PIMS	Pi-Mode Structure
PMQs	Permanent Magnet Quadrupoles
PS	Proton Synchrotron
PSB	Proton Synchrotron Booster
RF	Radio Frequency
RFQ	Radio Frequency Quadrupole
SEM	Secondary Electron Emission
ToF	Time-of-Flight

1. LINAC4 PROJECT AT CERN

CERN, the European Organization for Nuclear Research, is the largest particle physics laboratory in the world. The particles are accelerated through a series of accelerators and sent to various experimental areas for fundamental research.

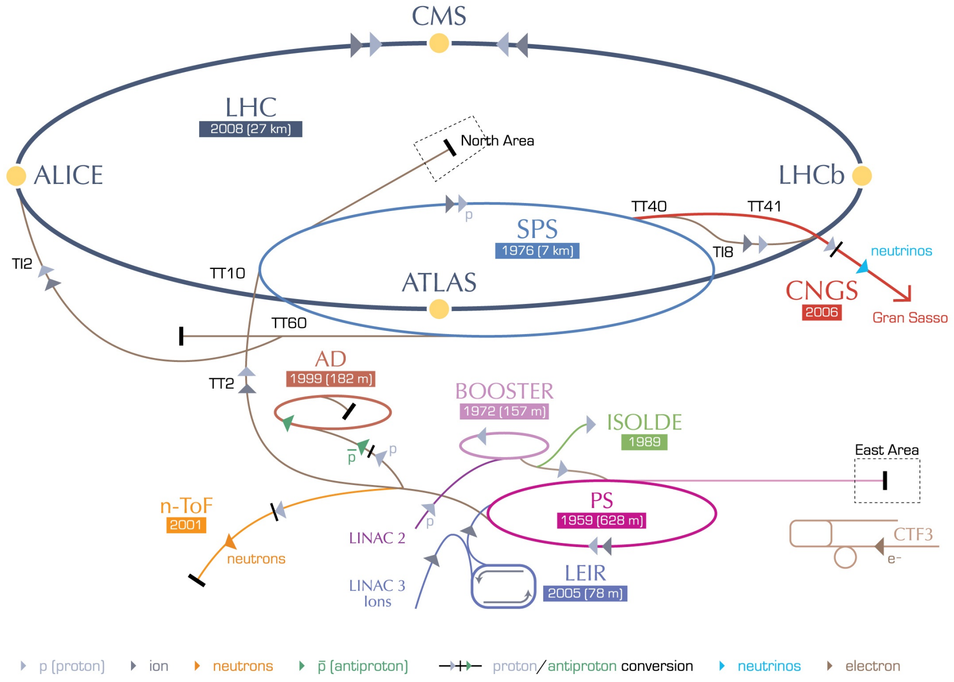

Figure 1.1. CERN's accelerator complex [1].

Figure 1.1 shows a schematic view of CERN's accelerator complex. The first stage of acceleration both for protons and ions takes place in linear accelerators (Linac2 for protons and Linac3 for ions). Afterwards, the particles are injected to circular machines for further acceleration.

The current hadron linac, Linac2, was commissioned in 1978 [2] and since then it has been the primary source of protons for CERN's accelerator complex. With the improvements on the machine, the beam current delivered to Proton Synchrotron Booster (PSB) increased to 180 mA in late 90's [3].

The reliability of the linac is crucial for CERN's accelerator complex as a failure in the operation of the linac would mean shutting down all the other machines. Even if the reliability of Linac2 improved during 80's and 90's, over the years important vacuum leaks appeared on the accelerating tanks [2, 4]. The possible vacuum leaks that may lead to significant periods of beam downtime [5] have been causing concern for future operation.

In the late 90's, a new linac, Superconducting Proton Linac (SPL), was proposed [6] and in 2000, the conceptual design report of a 2.2 GeV H^- linac was published [7]. The proposed linac would produce a low-intensity and high-brightness beam in the Proton Synchrotron (PS) for the Large Hadron Collider (LHC) and also accelerate high intensity beams for some other applications, like a neutrino factory [4].

As a future upgrade to LHC injector chain, Linac2 was proposed to be replaced by the initial 160 MeV part of SPL [8]. The proposed linac, Linac4, would accelerate H^- ions up to 160 MeV for injection into the PSB. With a higher output energy and charge exchange injection, Linac4 would increase the luminosity in the LHC.

The construction of Linac4 was approved by the CERN Council in June 2007 and the project started officially in January 2008 [9].

1.1. LINAC4: The Accelerator

Linac4 is an 86 m long normal conducting linac which will accelerate H^- ions up to 160 MeV. The operational RF frequency of the linac is 352.2 MHz. Figure 1.2 shows the basic architecture of Linac4. It is composed of an H^- source, a Low Energy Beam Transport (LEBT), a Radio Frequency Quadrupole (RFQ), a Medium Energy

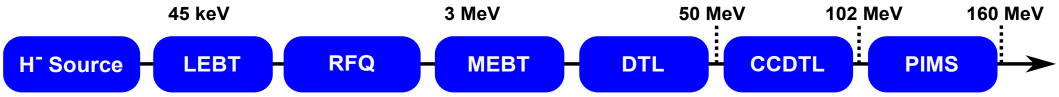

Figure 1.2. Basic architecture of Linac4.

Beam Transport (MEBT), a Drift Tube Linac (DTL), a Cell-Coupled Drift Tube Linac (CCDTL) and a Pi-mode structure (PIMS).

Linac4 will accelerate 400 μs long pulses at 40 mA average pulse current [10]. The pulse repetition rate is 1 Hz, therefore, the duty cycle is 0.04 per cent. The design value for the transverse rms emittance after the PIMS is 0.32 mm.mrad.

The following sections summarize the properties of the Linac4 structures.

1.1.1. The 3 MeV Front End

The Linac4 3 MeV front end consists of an H^- ion source, a Low Energy Beam Transport (LEBT), a Radio Frequency Quadrupole (RFQ) and a Medium Energy Beam Transport (MEBT).

1.1.1.1. Ion Source. The design specifications of the H^- ion source for Linac4 are as follows [11]:

- Pulse duration: 500 μs.
- Pulse repetition rate: 2 Hz.
- Beam intensity: 80 mA.
- Energy: 45 keV.
- Normalized rms emittance: 0.25 mm.mrad.

By the time of Linac4 technical design, the above specifications could not be met by any of the existing sources [4]. Therefore, it was foreseen that the design and construction of the ion source would require a long development time. The approach for Linac4 was to copy an existing source with close specifications and improve it. The RF volume source developed at DESY was chosen as a starting point [4].

Several H^- ion source prototypes were designed, produced and tested. The prototype (based on the concept developed at DESY) producing a current of around 20 mA was operational in the Linac4 tunnel and used for the commissioning of the linac up to 12 MeV. Also, a cesiated surface ion source could deliver a current of 40-50 mA [11].

1.1.1.2. Low Energy Beam Transport. The LEBT houses two solenoid magnets which are used for the beam matching from the ion source to the RFQ. There are several diagnostic instruments installed in the LEBT for monitoring the beam parameters during operation (see Section 6.1).

1.1.1.3. Radio Frequency Quadrupole. RFQ is the first accelerating structure of Linac4. It bunches and accelerates the beam to 3 MeV in three meters. The design transmission efficiency of the Linac4 RFQ is 95 per cent for a beam with normalized transverse rms emittance of 0.25 mm.mrad [12].

1.1.1.4. Medium Energy Beam Transport. MEBT line contains the beam chopping system which is essential for preparing the bunch structure for the injection to the PSB [4]. The chopping system consists of a double meander structure printed on an alumina substrate for the deflecting plates [13]. Each chopper unit is integrated in a

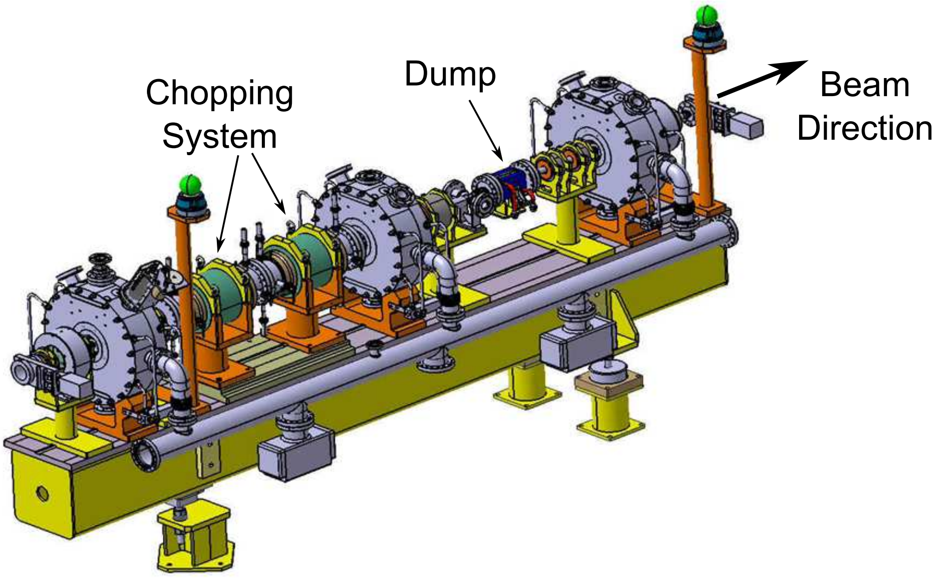

Figure 1.3. Drawing of the MEBT and its support [4].

quadrupole magnet (see Figure 1.3). The bunches deflected by the chopper plates are absorbed by the MEBT internal dump located one meter downstream of the second chopper unit [4].

MEBT line has 11 quadrupole magnets and three RF cavities. The first seven quadrupole magnets, which are located upstream of the dump, play an important role on chopping. The last four quadrupoles and the RF cavities are used for matching the beam to the drift tube linac in transverse and longitudinal planes, respectively.

1.1.2. Drift Tube Linac

The Linac4 drift tube linac (DTL), which consists of three tanks [14], will accelerate the beam from 3 MeV to 50 MeV. Table 1.1 shows some parameters of the DTL tanks. Due to the small size of the drift tubes, permanent magnet quadrupoles (PMQs) were chosen for transverse focusing.

Table 1.1. DTL parameters [14].

Parameter	Tank 1	Tank 2	Tank 3
Cavity length (m)	3.90	7.34	7.25
Cell per tank	39	42	30
Average accelerating field (MV/m)	3.1	3.3	3.3
Synchronous phase (deg)	-35 to -24	-24	-24
Focusing scheme	FFDD	FFDD	FFDD
Quadrupole magnet length (mm)	45	80	80

1.1.3. Cell-Coupled Drift Tube Linac

Cell-coupled drift tube linac (CCDTL) will accelerate the beam from 50 MeV to 102 MeV. Figure 1.4 shows a schematic view of a CCDTL module which is composed of three short DTL tanks. Each tank contains two empty drift tubes. The tanks are connected by off axis coupling cells. The quadrupole magnets for transverse focusing are placed between the tanks (PMQs) and between the modules (electromagnets). Linac4 CCDTL consists of seven modules with a total length of 25 meters.

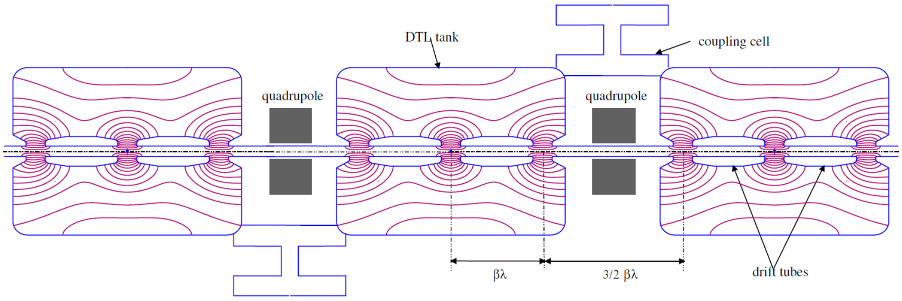

Figure 1.4. A CCDTL module with three DTL tanks [4].

When compared to the DTL, above 50 MeV, the main advantages of CCDTL are lower price, less demanding quadrupole alignment tolerances, easy access to the quadrupoles, simpler construction of the small tanks [4].

1.1.4. Pi-Mode Structure

Pi-mode structure (PIMS) is the last step of acceleration at Linac4. The PIMS will bring the beam to 160 MeV with 12 accelerating cavities in 21.5 m. Each cavity consists of seven cells [15]. The electromagnet quadrupoles will be used between the cavities for transverse focusing. Figure 1.5 shows a schematic view of a PIMS cavity.

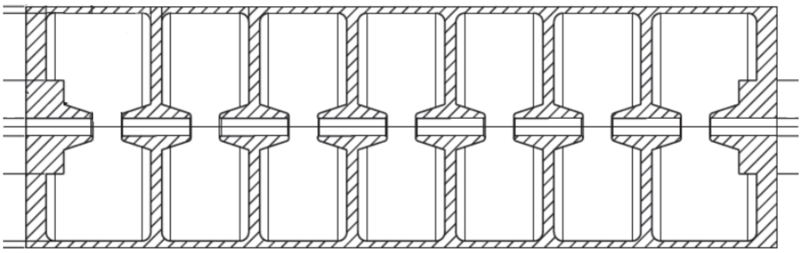

Figure 1.5. Schematic view of a PIMS cavity with seven cells.

1.1.5. Status and Commissioning Plan

Linac4 is at its commissioning phase. The accelerator is being commissioned progressively with the installation of the accelerating structures into the Linac4 tunnel. The first three stages of commissioning, which focused mainly on the characterization of the RFQ (3MeV), the validation of the chopping system and the characterization of the first DTL tank (12MeV), have been successfully performed by the end of 2014 [16].

The next beam commissioning stage at 50 MeV will start in September 2015 after the installation of the second and third DTL tanks. After commissioning the DTL with a beam, the 100 and 160 MeV stages will follow for the commissioning of the CCDTL and PIMS.

After reaching the final energy, there will be a year-long reliability run before connecting Linac4 to the CERN's accelerator complex [17]. Linac4 will be connected to the PSB during the next long LHC shutdown and it will replace Linac2.

2. BASICS OF BEAM DYNAMICS

This chapter presents some basic concepts in beam dynamics which will be used later in this thesis. The discussion in this chapter (also in the thesis) will be mostly based on the description of a bunch as an ensemble of particles.

2.1. Energy Gain in an RF Cavity

This section presents the derivation of the expression for energy gain through a pillbox cavity considering a particle traveling on axis.

For a cylindrically symmetric cavity, longitudinal component of the time dependent electric field can be expressed as in Equation 2.1. The energy gain on axis (for $r = 0$) can be calculated by integrating the expression for the infinitesimal energy gain given in Equation 2.2.

$$E_z(r, z, t) = E(r, z) cos\,(\omega t + \phi) \tag{2.1}$$

$$dW = qE_z(0, z, t)dz \tag{2.2}$$

The variables t and z can be related to each other by $v(z) = dz/dt$ where $v(z)$ is the speed of the particle. Therefore, time can be expressed as a function of z by $t(z) = \int_0^z dz/v(z)$ where we choose $t = 0$ at $z = 0$.

Let us consider the pillbox cavity shown in Figure 2.1a where origin of the z coordinate is at the center of the cavity. Figure 2.1b shows the field distribution at $r = 0$ along the z axis. The total energy gain of the particle through the cavity can be calculated by inserting Equation 2.1 into Equation 2.2 and integrating from -L/2 to L/2 as shown in Equation 2.3 .

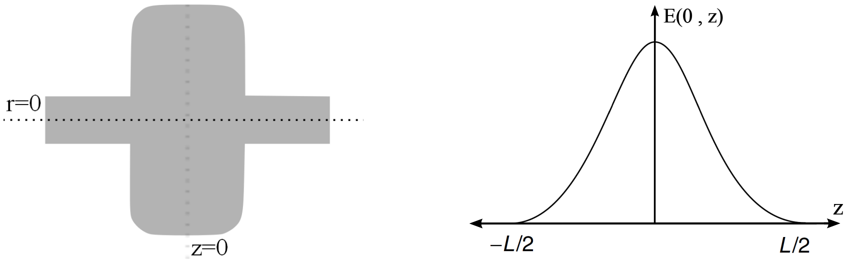

(a) (b)

Figure 2.1. (a) An RF pillbox cavity. (b) Axial field of the RF cavity with an extend of $\pm L/2$ in z direction.

$$\Delta W = q \int_{-L/2}^{L/2} E(0,z) cos\left(\omega t + \phi\right) dz \tag{2.3}$$

Using the relevant trigonometric identity Equation 2.3 can be written as in Equation 2.4

$$\Delta W = q \int_{-L/2}^{L/2} E(0,z) \left[cos\omega t cos\phi - sin\omega t sin\phi\right] dz \tag{2.4}$$

As it can be seen in Figure 2.1b, E(0,z) is symmetric about the geometric center of the cavity, therefore it is an even function (this is usually the case for most of the accelerating structures). However, $sin\omega t$ is an odd function. Therefore, in Equation 2.4, the contribution of the second term in the square brackets is zero which simplifies the energy gain equation as in Equation 2.5 .

$$\Delta W = q cos\phi \int_{-L/2}^{L/2} E(0,z) cos\omega t dz \tag{2.5}$$

By defining V_0 and T as in Equations 2.7 [18] and 2.8, the relation for energy gain can be written in a more practical form as in Equation 2.6.

$$\Delta W = qV_0 T cos(\phi) \tag{2.6}$$

In Equation 2.6, ϕ is the phase of the RF relative to crest when the particle is at the center of the cavity.

$$V_0 \equiv \int_{-L/2}^{L/2} E(0,z)dz \tag{2.7}$$

V_0 is the axial RF voltage and T is the transit time factor. V_0 is the voltage gain through the cavity if the electric field was not changing in time. T introduces the effect of the changing fields. V_0T is called effective axial RF voltage (see also Section 7.3.2).

$$T \equiv \frac{\int_{-L/2}^{L/2} E(0,z)cos\omega tdz}{\int_{-L/2}^{L/2} E(0,z)dz} \tag{2.8}$$

2.2. Lorentz Force

The force on a particle with charge q and velocity $\vec{v}$, due to electric and magnetic fields, can be calculated from Lorentz force equation (Equation 2.9) where $\vec{E}$ and $\vec{B}$ are electric and magnetic fields, respectively.

$$\vec{F} = q\left(\vec{E} + \vec{v} \times \vec{B}\right) \tag{2.9}$$

The relation between the force and the rate of change of momentum is given in Equation 2.10. The momentum is defined as $\vec{p} = \gamma_r m\vec{v}$, where γ_r is the relativistic factor and m is the rest mass.

$$F = \frac{d\vec{p}}{dt} = m\frac{d(\gamma_r\vec{v})}{dt} \tag{2.10}$$

By inserting Equation 2.10 into Equation 2.9, the basic equation which describes the dynamics of particles in electric and magnetic fields can be written as in Equation 2.11.

$$m\frac{d\left(\gamma_r\vec{v}\right)}{dt} = q\left(\vec{E} + \vec{v} \times \vec{B}\right) \tag{2.11}$$

2.3. Coordinate System and Phase Space Plots

When a bunch of particles is described, the coordinates of each particle are given relative to the reference particle. Figure 2.2 shows a co-moving right-handed coordinate system whose origin moves with the reference particle with momentum $\vec{p_0}$ which defines the direction of the z axis. Throughout this thesis, subindex “0” will indicate that the property belongs to the reference particle.

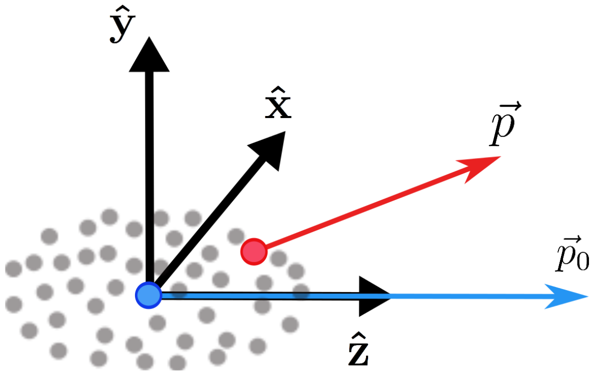

Figure 2.2. The co-moving coordinate system.

Any particle in the bunch can be defined in a six dimensional phase space as in Equation 2.12.

$$\vec{\boldsymbol{X}} = \begin{bmatrix} x \\ x' \\ y \\ y' \\ z \\ \frac{\Delta p}{p_0} \end{bmatrix} \tag{2.12}$$

The coordinates x, y, z represent the position of the particle relative to the reference particle. x', y' and $\Delta p/p_0$ are defined as in Equations 2.13, 2.14 and 2.15.

$$x' = \frac{dx}{dz} \tag{2.13}$$

$$y' = \frac{dy}{dz} \tag{2.14}$$

$$\frac{\Delta p}{p_0} = \frac{p - p_0}{p_0} \tag{2.15}$$

For the last two parameters, it is also common to use $\Delta\phi$ and ΔW which are phase and energy difference between a particle and the reference particle. Equations 2.16 and 2.17 [19] shows the relationship between two sets of coordinates.

$$z = -\frac{\beta_r \lambda}{360} \Delta\phi \tag{2.16}$$

In the equations, β_r, is relativistic parameter and λ is the free space wavelength of the RF.

$$\frac{\Delta p}{p_0} = \left(\frac{\gamma_r}{\gamma_r + 1}\right) \frac{\Delta W}{W_0} \tag{2.17}$$

2.3.1. Phase Space Plots and Emittance

During the beam dynamics studies, it is more practical to work with two dimensional phase space projections of the beam which are x-x' (horizontal), y-y' (vertical), and $\Delta\phi$-ΔW (longitudinal). For instance, Figure 2.3 shows the particle distribution in horizontal phase space. The graph is called phase space plot of the beam. In a phase space plot, each dot represents a particle.

In each phase space, one can define a parameter called emittance, ϵ, which shows the quality of the beam. For an ensemble of particles it is most common to define rms emittance which is based on second moments of the distributions. The concept of rms emittance in a phase space for an ensemble of particles was first introduced by

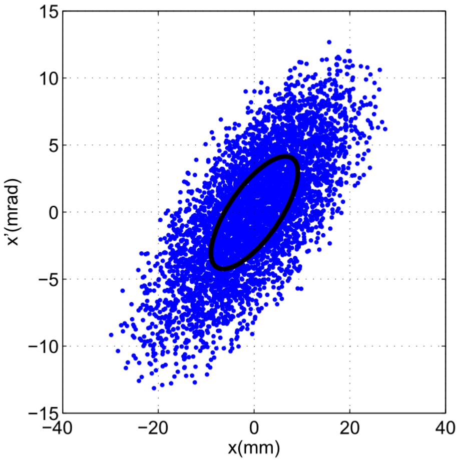

Figure 2.3. Horizontal phase space and rms envelope ellipse.

Lapostolle [20] and Sacherer [21] in 1970.

In x-x' phase space, the rms emittance for a particle bunch is defined as in Equation 2.18 where each parameter under the square root is calculated using Equations 2.19, 2.20 and 2.21.

$$\epsilon_{rms} = \sqrt{< x^2 >< x'^2 > - < xx' >^2} \tag{2.18}$$

The terms in Equations 2.20 and 2.21 are related to the root mean square (rms) of one dimensional distribution of x and x', where $x_{rms} = \sqrt{< x^2 >}$ and $x'_{rms} = \sqrt{< x'^2 >}$.

$$< x^2 > = \frac{1}{N}\sum_{i=1}^{N}(x_i - < x >)^2 \tag{2.19}$$

$$< x'^2 > = \frac{1}{N}\sum_{i=1}^{N}(x'_i - < x' >)^2 \tag{2.20}$$

$$< xx' > = \frac{1}{N}\sum_{i=1}^{N}(x_i - < x >)(x'_i - < x' >) \tag{2.21}$$

The rms emittance can be considered as a statistical mean area that is a measure of the spread of the particles around their barycenter [22].

The emittance itself does not give all the information about the distribution in a phase space. It is also useful to know the shape and orientation of the particle distribution in a phase space. This information can also be obtained from the second order moments of the distributions.

The equation of the rms envelope ellipse shown in Figure 2.3 can be defined as in Equation 2.22 where the area of the ellipse is given by $A = \pi\epsilon$. The major axis of the ellipse defines a direction where the rms of the distribution is maximized. Likewise along the minor axis of the ellipse the rms of the distribution is minimum.

$$\gamma x^2 + 2\alpha x x' + \beta x'^2 = \epsilon \tag{2.22}$$

The parameters of the ellipse α, β and γ are called as beam Twiss parameters and they are not independent. β and γ are related to x_{rms} and x'_{rms} as in Equations 2.23 and 2.24. Parameter α can be calculated using Equation 2.25.

$$\begin{aligned} x_{rms} &= \sqrt{\beta\epsilon} && (2.23) \\ x'_{rms} &= \sqrt{\gamma\epsilon} && (2.24) \\ \gamma &= \frac{1+\alpha^2}{\beta} && (2.25) \\ & && (2.26) \end{aligned}$$

One can define a two by two matrix which describes the rms envelop ellipse of the beam in a phase space as in Equation 2.27. The matrix $\boldsymbol{\sigma}$ is called sigma or beam matrix.

$$\boldsymbol{\sigma} = \epsilon \begin{bmatrix} \beta & -\alpha \\ -\alpha & \gamma \end{bmatrix} \tag{2.27}$$

Figure 2.4 shows the relationship between the rms envelope ellipse and beam Twiss parameters.

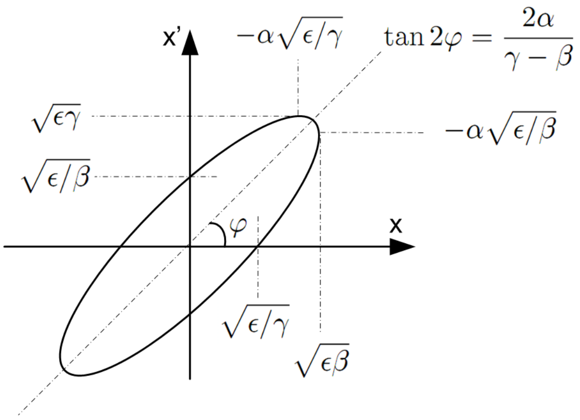

Figure 2.4. The relationship between the ellipse and beam Twiss parameters.

2.3.1.1. Normalized Emittance. Liouville's theorem states that, under the influence of conservative forces, the particle density in phase space is invariant [23]. It follows that ϵ_{rms} of the distribution in a phase space is constant. However the transverse phase spaces introduced in Section 2.3.1 are not ordinary phase spaces with position and momentum conjugate to it. The transverse emittance of the beam in a phase space described by position and divergence (x-x') is called unnormalized emittance and it is conserved only if the energy is constant.

The divergence angle x' is related to the conjugate momentum p_x as in Equation 2.28. As it seems in the equation $\gamma\beta x'$ is directly proportional to p_x.

$$p_x = \gamma_r m \beta_r c x' \tag{2.28}$$

One can introduce a normalized emittance which is proportional to the area in x-p_x canonical phase space as in Equation 2.29, where ϵ_n and ϵ_{un} are normalized and unnormalized emittance, respectively.

$$\epsilon_n = \gamma_r \beta_r \epsilon_{un} \tag{2.29}$$

2.4. Matrix Formalism in Linear Beam Dynamics

In most cases (especially for low intensity beams) the motion of the particles in three planes can be decoupled and treated separately. In this chapter, the equation of motion for a quadrupole magnet will be solved for transverse planes and the transfer matrix formalism will be introduced.

Starting with Equation 2.11 one can find consider only magnetic field and find the equation of motion in transverse planes for quadrupole, dipole and drift space. The derivation of equation of motion can be found in [23, 24]. An alternative derivation of the equation of motion (for positively charged particles) through a quadrupole magnet is presented in Appendix A.

Equations 2.30 and 2.31 shows the equation of motion through a quadrupole magnet in horizontal and vertical plane, where k is the quadrupole strength (see Appendix A).

$$x'' + k^2 x = 0 \tag{2.30}$$

$$y'' - k^2 y = 0 \tag{2.31}$$

The solution of the equation of motion for horizontal plane is given in Equations 2.32 and 2.33.

$$x(z) = Acos(kz) + Bsin(kz) \tag{2.32}$$

$$x'(z) = -kAsin(kz) + kBcos(kz) \tag{2.33}$$

The constants A and B can be determined by introducing the initial conditions and solving Equations 2.32 and 2.33 together. Let us denote the initial coordinates at $z = 0$ by x_0 and x'_0. After introducing the initial conditions one obtains $A = x_0$ and $B = x'_0/k$. After inserting the values of constants, let us consider a quadrupole magnet with a length l_q and write Equations 2.32 and 2.33 as in Equations 2.34 and 2.35 where the final coordinates after the quadrupole are denoted by x_f and x'_f.

$$\begin{aligned} x_f &= x_0 cos(kl_q) + \frac{x'_0}{k} sin(kl_q) && (2.34) \\ x'_f &= -kx_0 sin(kl_q) + x'_0 cos(kl_q) && (2.35) \end{aligned}$$

Equations 2.34 and 2.35 can be written in a matrix form as in Equation 2.36.

$$\begin{bmatrix} x_f \\ x'_f \end{bmatrix} = \begin{bmatrix} cos(kl_q) & \frac{1}{k} sin(kl_q) \\ -ksin(kl_q) & cos(kl_q) \end{bmatrix} \begin{bmatrix} x_0 \\ x'_0 \end{bmatrix} \tag{2.36}$$

Equation 2.31 can also be solved in the same way and Equation 2.37 can be obtained for the vertical plane.

$$\begin{bmatrix} y_f \\ y'_f \end{bmatrix} = \begin{bmatrix} cosh(kl_q) & \frac{1}{k} sinh(kl_q) \\ ksinh(kl_q) & cosh(kl_q) \end{bmatrix} \begin{bmatrix} y_0 \\ y'_0 \end{bmatrix} \tag{2.37}$$

The two by two matrices in Equations 2.36 and 2.37 are called transfer matrices and will be represented by $\boldsymbol{R}$ in this thesis. The one in Equation 2.36 is for a focusing magnet and the one in Equation 2.37 is for a defocusing magnet. The field pattern of the magnet shown in Figure A.1 resulted in focusing in horizontal and defocusing in vertical plane. However if it is rotated 90° around the z axis it would be defocusing in horizontal plane and focusing in vertical plane. Therefore, the transfer matrices are common for both transverse planes.

Such transfer matrices can be derived for each accelerator element and used for particle tracking. Let $\vec{\boldsymbol{x}}$ be the column vector which defines the coordinates of the particle in a phase space. Transfer matrix of an element relates the coordinates at the beginning ($\vec{\boldsymbol{x}}_{\mathbf{0}}$) and at the exit ($\vec{\boldsymbol{x}}_{\mathbf{1}}$) of the element as shown in Equation 2.38.

$$\vec{\boldsymbol{x}}_{\mathbf{0}} = \boldsymbol{R}\vec{\boldsymbol{x}}_{\mathbf{0}} \tag{2.38}$$

If there are N consecutive elements in a beam line, the coordinates before and after the beam line can be related by Equation 2.39 where $\boldsymbol{R}_1$ and $\boldsymbol{R}_N$ are the transfer matrices of the first and the last elements, respectively.

$$\vec{\boldsymbol{x}}_{\mathbf{1}} = \boldsymbol{R}_N\boldsymbol{R}_{N-1}\boldsymbol{R}_{N-2}\cdots\cdot\boldsymbol{R}_2\boldsymbol{R}_1\vec{\boldsymbol{x}}_{\mathbf{0}} \tag{2.39}$$

One can also calculate the evolution of the beam matrix which describes the rms properties of the distribution as in Equation 2.40 [23].

$$\boldsymbol{\sigma}_{\mathbf{1}} = \boldsymbol{R}\boldsymbol{\sigma}_{\mathbf{0}}\boldsymbol{R}^T \tag{2.40}$$

Computer codes for particle tracking like (Trace 3-D [19]) use matrix formalism for computation of the evolution of beam properties through a beam line. Complete set of 6-D transfer matrices can be found in [19].

2.5. Particle Tracking Codes

The matrix formalism introduce in the previous section applies to linear beam optics. When the nonlinear forces (like space-charge) are introduced, the dynamics calculations are not straightforward. In that case, computer simulation codes can be used for modeling the dynamics of the particle beam through the accelerator. Especially for the low energy part of the high-intensity linacs where the space charge forces are dominant, an accurate tracking code is vital for the design.

There are several codes available for particle tracking through hadron linacs which take into account the space charge forces. For instance Trace 3-D [19] calculates the evolution of rms envelope ellipse by assuming a uniform charge distribution in space for linearizing the space-charge forces.

Nowadays, it is more common to use multi-particle tracking codes where one does not need to make an assumption about the particle distribution. For instance, Parmteqm [25] can be used for tracking multi-particle beams through an RFQ. Likewise, PATH and TraceWin [26] can be used for the rest of the linac.

PATH is a package of codes which includes Travel [27] for tracking a multi-particle beam and Delta [28] for studying the errors. PATH was used for most of the beam dynamics simulations presented in this thesis.

3. TRANSVERSE AND LONGITUDINAL ACCEPTANCE STUDIES

Acceptance is an important figure of merit for accelerators. It is defined as the area in phase space within which charged particles can be transported without loss. Acceptance is usually referred to the injection point of the linac and compared to the emittance of the injected beam [29]. As Linac4 is at its commissioning period, it is important to evaluate the acceptance of each individual section in order to identify bottlenecks and the sections that need to be adjusted more carefully during the installation process. Using multi-particle tracking codes, simulations were performed in order to determine the acceptance of each section of Linac4. The following sections present the method adopted for the simulations and the results of the transverse and longitudinal acceptance studies for Linac4.

3.1. Method for Acceptance Studies

The acceptance plot in a phase space can be defined as the representation of the coordinates of all the particles that can be received by a section of an accelerator and transported until the end without loss [30]. In order to obtain the acceptance plot with a multi-particle tracking code, one can use an input beam which occupies a big area in a phase space and simulate it through the accelerator part under study. Depending on the size of the input beam, some particles will be lost along the beam line. The initial coordinates of the surviving particles will give the acceptance plot. In order not to underestimate the acceptance, the input beams for the simulations must be chosen big enough to include all the particles that can survive until the end. Figure 3.1a compares the input beam for simulations and the acceptance plot for PIMS in horizontal phase space. The shape and orientation of the acceptance plot in a phase space depend on the structure. Figure 3.1b shows the acceptance plot of PIMS in the horizontal plane. As it can be seen from the figure, the shape of the acceptance plot is not necessarily an ellipse. However, the beam mostly forms an ellipse in a phase space. Therefore, for the

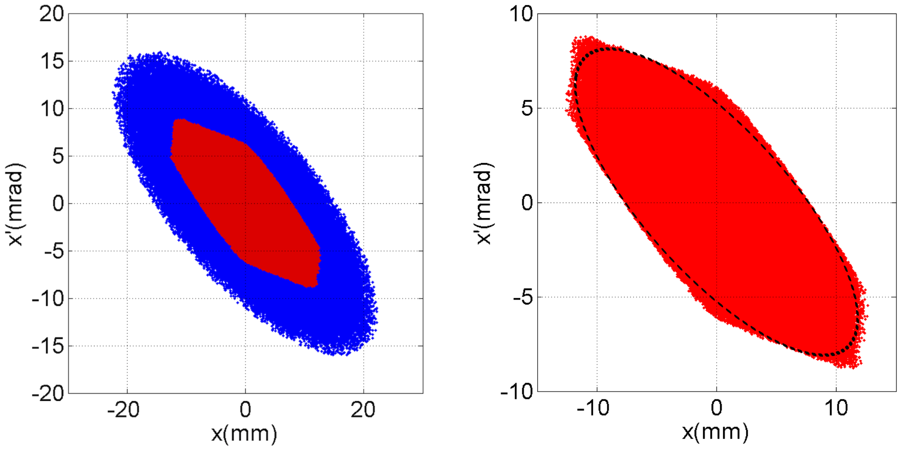

(a) (b)

Figure 3.1. (a) Comparison of the input beam phase space and the acceptance plot. (b) Acceptance plot and the biggest emittance ellipse that fits inside it.

quantitative comparison of the beam emittance with acceptance, it is more practical to check the area of the biggest ellipse that fits inside the acceptance plot (dotted black line in Figure 3.1b). Therefore, for convenience, acceptance will be determined by the area of the biggest ellipse inside an acceptance plot. Acceptance should be specified independently for the longitudinal and the two transverse phase spaces.

Transverse acceptance is an important figure of merit for the focusing lattice in accelerators. Comparison of the transverse acceptance with the transverse emittance of the injected beam gives an indication of the safety margin available to compensate for transverse emittance growth, misalignment and beam steering [29]. Because linacs are basically composed of a series of accelerating structures and relatively short matching sections between them, the longitudinal acceptance is an important figure of merit for linacs. Comparison of the longitudinal acceptance of an element and longitudinal emittance of the injected beam gives an indication of the safety margin available to compensate for longitudinal emittance growth, field errors and phase jitter along the upstream elements.

Simulations for the Linac4 acceptance studies were performed with multi-particle tracking codes PATH and Parmteqm (see Section 2.5). Parmteqm was used only for the

RFQ simulations. The rest of the linac was studied using PATH which has a feature to plot the initial coordinates of the particles which survive until a specified point along the beam line.

The method for the transverse and longitudinal acceptance studies (except for the RFQ) are explained in the following sections. The method for the RFQ acceptance studies will be explained in 3.2.2.

3.1.1. Method for the Transverse Acceptance Studies

The transverse acceptance can be determined by checking the area of the biggest ellipse that fits inside the acceptance plot in a transverse phase space. Depending on the structure, acceptance in two transverse planes can be the same or different, so acceptance must be specified independently for two transverse phase spaces. When space charge effects are included in the calculation, the acceptance depends on the input beam distribution and the beam current. In this case, one would obtain different acceptance plots with different input particle distributions and beam currents. To avoid this dependence, one can run the simulations with zero beam current and obtain the zero current acceptance plots. The zero current acceptance is a property of the structure only and does not depend on the input beam that is used for the simulations. Throughout this thesis acceptance will refer to the zero current acceptance.

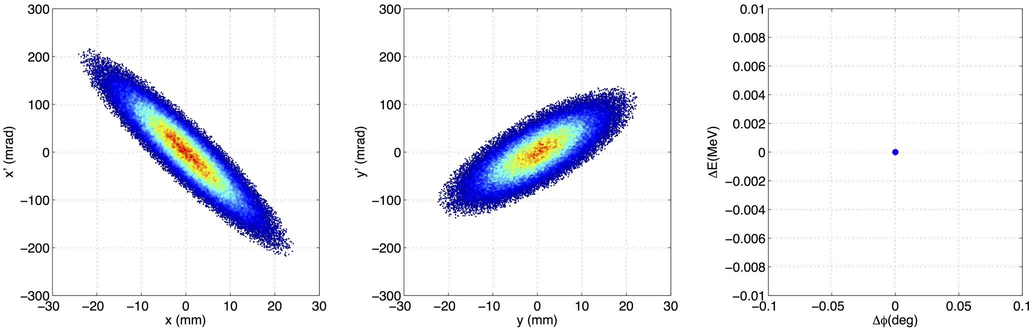

(a) (b) (c)

Figure 3.2. Phase space plots of a Gaussian input beam for transverse acceptance studies.

For the transverse acceptance studies, two different types of input beam have been used. These input beams have been created using PATH. Figure 3.2 shows an example of the first type which has a Gaussian distribution in two transverse phase spaces and no longitudinal phase or energy spread ($\Delta E = 0, \Delta\phi = 0$). Throughout this thesis, this type of input beam will be addressed as Gaussian input beam. Using a Gaussian input beam, one can obtain the acceptance plots for both transverse phase spaces with only one simulation. Because I_{Beam} is zero for the simulations, the particle distribution is irrelevant for the result. However, since the particles are populated at the center of the beam in the transverse planes, acceptance plots will contain large number of particles easing the plotting and data extraction.

Figure 3.3 shows an example of the second type of input beam which has a uniform particle distribution in only one of the two transverse phase spaces. Throughout this thesis, this type of input beam will be addressed as uniform input beam. The beam shown in Figure 3.3 can be used only for the horizontal plane acceptance studies. In the horizontal phase space, the beam has a certain emittance. However, in the vertical and longitudinal phase spaces, all the coordinates of all the particles are zero, which makes the emittance zero in these phase spaces. Having a zero emittance in the other planes ensures that the particle losses would be only due to the motion of the particles in the horizontal plane. For the vertical plane acceptance studies, the uniform input beam should have a certain emittance in the vertical phase space with a uniform particle distribution and zero emittance in the horizontal and in the longitudinal phase spaces.

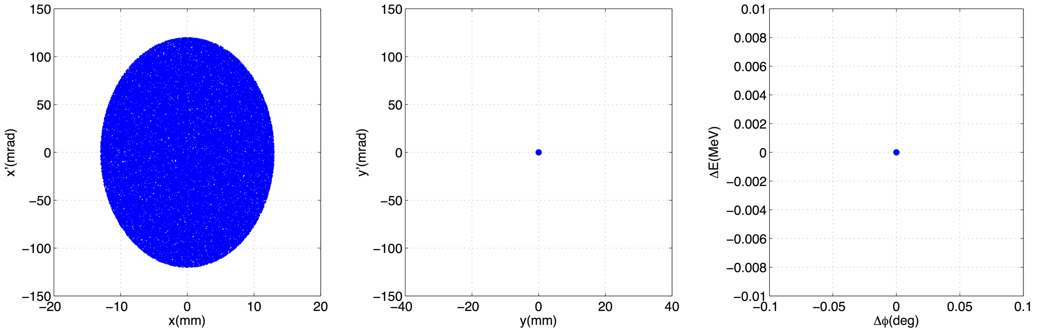

(a) (b) (c)

Figure 3.3. Phase space plots of a uniform input beam.

The simulation results show that, even if the beam current is zero, the choice of the input beam has an effect on the acceptance plot. The acceptance plots from a Gaussian input beam and a uniform input beam may have slight differences. The effect of the input particle distribution on the acceptance plot and the choice of the input beam types for the acceptance studies are discussed in [30].

3.1.1.1. The Effect of Errors on Transverse Acceptance. Machining errors during the production or alignment errors during the installation process may have some effects on the characteristics of the accelerator. Because of these errors, the structure along Linac4 may have small differences compared to the original design. Alignment and field error tolerance for the Linac4 accelerating structures is defined in [31]. Not all the structures along Linac4 have the same sensitivity to alignment errors. Therefore, the effect of alignment errors on the transverse acceptance has been studied for each individual structure of Linac4 in order to determine the sections that need to be adjusted more carefully during the installation process.

The choice of the input beam for the simulations is important for the method adopted to determine the effect of alignment errors on the transverse acceptance. The horizontal and the vertical planes have been studied independently using different uniform input beams. Using a uniform input beam ensures that the particle losses are only due to motion of the particles in the plane under study. Figure 3.4 compares the horizontal phase space of two different input beams and the acceptance plots obtained using each beam. The result presented in Figure 3.4a has been obtained using an input beam with a large emittance in both transverse phase spaces while the result in Figure 3.4b has been obtained using an input beam with a large emittance only in the horizontal phase space (see Figure 3.3). Both of the input beams have zero emittance in the longitudinal phase space. In both cases, the shape, orientation and the area of the acceptance plots are the same. However, as it can be seen from Figure 3.4a , when the input beam has large emittance in both transverse phase spaces, some particles (blue spots inside the red area) are lost even if they are inside the horizontal acceptance plot. These particles have not been accepted by the structure in the vertical plane.

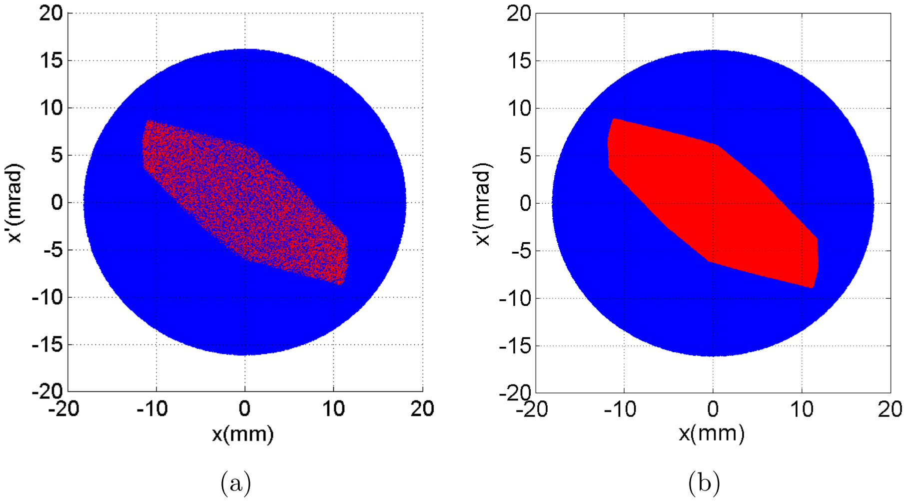

(a) (b)

Figure 3.4. The comarison of the input beam and acceptance plot in the horizontal phase space (a) when the input beam has big emittance in both transverse planes and (b) when the input beam has big emittance only in the horizontal plane.

However, when the input beam has zero emittance in the vertical phase space, all the particles inside the horizontal acceptance plot are transmitted through the structure (see Figure 3.4b). The use of the input beam presented in the Figure 3.3, allows one to calculate the area occupied by the acceptance plot in a phase space using only the emittance of the input beam and the transmission efficiency with Equation 3.1 , where A is the area occupied by the acceptance plot, ϵ_{Total} is the total emittance of the input beam and T is the transmission efficiency (normalized to one) from the simulation.

$$A = \epsilon_{Total}T \tag{3.1}$$

In order to study the effect of misalignment, 2000 simulations with different misalignment were run for each transverse plane of each structure of Linac4. For each simulation, the change in acceptance was estimated by checking the change in the area of the acceptance plot, calculated with Equation 3.1. The results from all the simulations were analyzed and the cumulative probability for the change of acceptance was obtained . The plot of cumulative probability vs. change in acceptance for a structure gives an indication of how sensitive it is to errors (see Section 3.2).

3.1.2. Method for the Longitudinal Acceptance Studies

The longitudinal acceptance can be determined by checking the area of the biggest ellipse that fits inside the acceptance plot in the longitudinal phase space. As in the case of transverse acceptance, throughout this document, longitudinal acceptance will refer to the zero current longitudinal acceptance. The input beams for the longitudinal acceptance studies have a small transverse emittance in both planes. In longitudinal phase space, they have ±180° phase spread and a large energy spread with a uniform particle distribution. Figure 3.5 shows an example of the input beams used for the longitudinal acceptance studies.

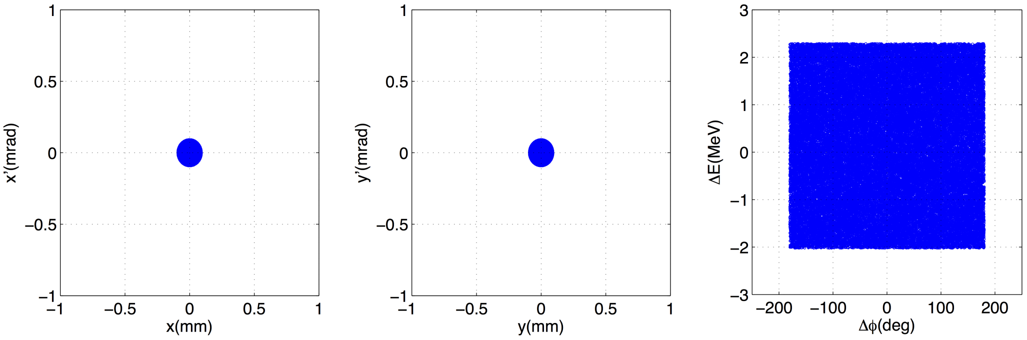

(a) (b) (c)

Figure 3.5. Phase spaces of an input beam for the longitudinal acceptance studies.

When such an input beam is simulated through an accelerating structure, the big initial longitudinal emittance and small transverse emittance will caus the output particle distribution to have a long tail in longitudinal phase space (see Figure 3.6a). At the end of an accelerating structure, the output beam should be properly bunched, so the particles forming the tail must be filtered out. In order to determine the longitudinal acceptance, simulations were performed in two steps:

- Simulate the input beam (Figure 3.5) and check the output particle distribution in the longitudinal phase space.
- Use filters for the energy and the longitudinal phase [27] at the end of the beam line file to ensure that only the particles with energy around the design output

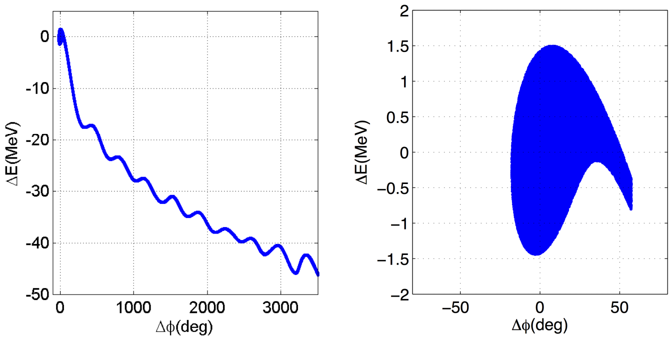

(a) (b)

Figure 3.6. Longitudinal phase space of the output beams from the longitudinal acceptance studies: (a)without phase and energy filter, (b)with phase and energy filter.

energy and with reasonable longitudinal phase survive until the end. Then, run the simulation again and obtain the longitudinal acceptance plot.

Figure 3.6 shows longitudinal phase spaces of two output beams obtained simulating the same input beam through the same structure with (Figure 3.6b) and without (Figure 3.6a) the energy and phase filters.

3.2. Results

3.2.1. Low Energy Beam Transport

The transverse acceptance of the LEBT is 22.5 mm.mrad in both transverse planes. Figure 3.7 compares the LEBT acceptance plots and the nominal LEBT input beam[1] in the transverse phase spaces. Two solenoid magnets are the only focusing elements on the LEBT. Because the solenoid magnetic fields have radial symmetry, the acceptance plots in the horizontal plane and in the vertical plane are identical.

LEBT transports continuous beam from the source to the RFQ, so a longitudinal

---

[1] The nominal input beam for the LEBT is extracted from IBSimu [32] simulations. The input beam for the other structures are obtained by tracking this beam forward to the injection point of the structure.

acceptance study is irrelevant for the LEBT.

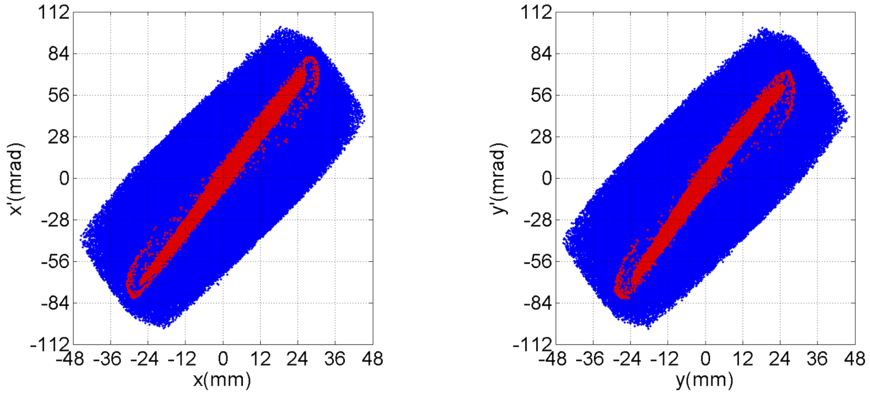

(a) (b)

Figure 3.7. Phase spaces of the nominal input beam and LEBT acceptance plots: (a)horizontal plane, (b)vertical plane.

3.2.2. Radio Frequency Quadrupole

The simulations of the RFQ were performed with Parmteqm. Because Parmteqm does not have a feature to plot initial coordinates of the output particles, a different method had to be adopted for the RFQ acceptance studies. In order to obtain the acceptance plot, the single particle run feature of Parmteqm was used. Using a program written in C++ language, particles with different coordinates in the transverse or longitudinal phase spaces were generated at the injection point of the RFQ and simulated. For each input particle, the program varies the initial coordinates (x, x′, y, y′, phase and energy) and writes an input file for Parmteqm. After preparing the Parmteqm input file, the program runs Parmteqm. At the end of each run, if the particle is alive, input parameters and output parameters of the particle are recorded into a text file. If the particle is lost, it is indicated in the text file with the initial parameters of the particle.

By lotting the initial coordinates of the particles that come out of the RFQ around the design energy (3 MeV), a phase space was constructed at the injection point of the RFQ and the acceptance plot was obtained.

<u>3.2.2.1. Transverse Acceptance of the RFQ.</u> Acceptance of the RFQ in two transverse phase spaces was studied independently. During the simulations while changing the position and angle to scan the transverse phase space in one plane, for the other plane, both position and angle were set to zero. The Linac4 RFQ is designed for the input energy of 45 keV, so for simulations all the input particles had an energy of 45 keV and the longitudinal phase of the input particles was set to zero. Figure 3.8 compares the RFQ input beam with the RFQ acceptance plots in both transverse phase spaces. Acceptance of the RFQ is 2.6 mm.mrad in both transverse planes for the nominal vane voltage of 79 kV.

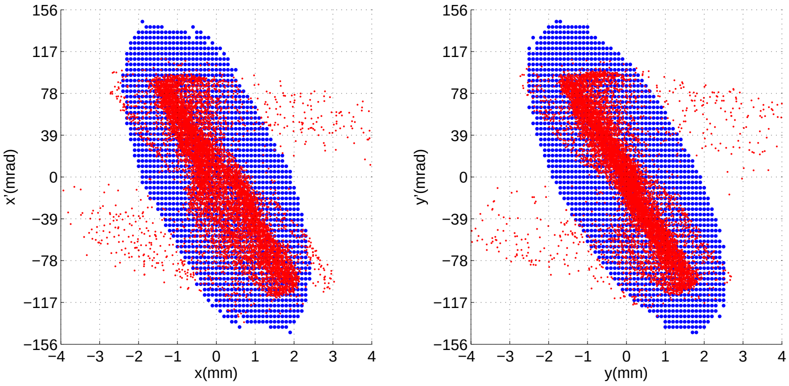

(a) (b)

Figure 3.8. Phase spaces of the nominal input beam and RFQ acceptance plots: (a)horizontal plane, (b)vertical plane.

In order to check the effect of the vane voltage on transverse acceptance, a set of simulations were performed only for the vertical plane. The vane voltage was varied within about 10 per cent around the nominal value and transverse acceptance was calculated. Figure 3.9a shows the change of vertical acceptance with the vane voltage. As it can be seen from the figure the vertical acceptance increases almost linearly with the increasing vane voltage. Figure 3.9b compares the vertical acceptance plots for three different vane voltage values.

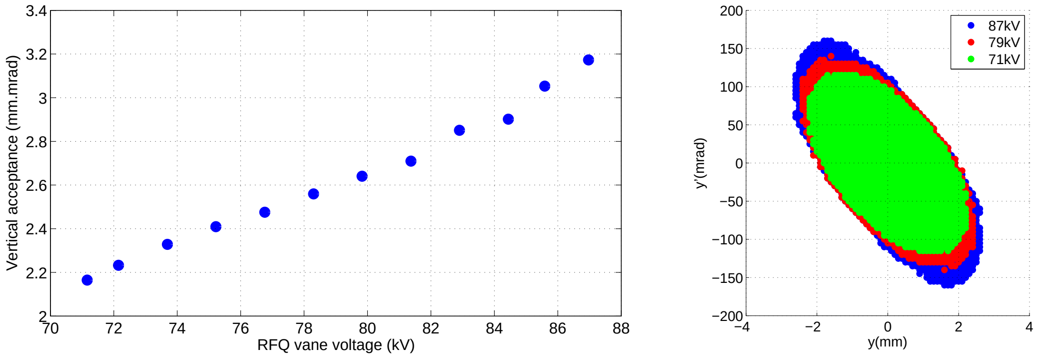

(a) (b)

Figure 3.9. (a) Vertical acceptance as a function of the vane voltage. (b) Comparison of vertical acceptance plots for three different vane voltage values.

3.2.2.2. Energy Acceptance of the RFQ. The RFQ receives continuous beam from the LEBT. While the longitudinal phase of the particles is irrelevant, the energy of the injected particles have an effect on the transmission. A set of simulations was performed to determine the energy range within which the RFQ can accept the particles. For the simulations, input particles were created on axis and with no transverse angle. Energies between 35 keV and 55 keV (10 keV relative to the RFQ design input energy) were scanned for one RF bucket. Because the particles do not feel any transverse force, none of the particles are lost. Most of the particles have output energies close to 3 MeV, while some particles have output energies close to zero. Figure 3.10 shows the input (Figure 3.10a) and output (Figure 3.10b) coordinates of the simulated particles in the longitudinal phase space. Particles coming out of the RFQ with an energy close to design output energy of the RFQ are plotted with red and the others with blue. As it can be seen from Figure 3.10, particles with initial energy higher than 39 keV and lower than 51 keV are captured and accelerated efficiently.

3.2.3. Medium Energy Beam Transport

The acceptance of the MEBT line is 3.6 mm.mrad in the horizontal plane and it is 2.1 mm.mrad in the vertical plane. Figure 3.11 shows the horizontal and the vertical acceptance plots for the MEBT. Since the MEBT line is not a periodic focusing

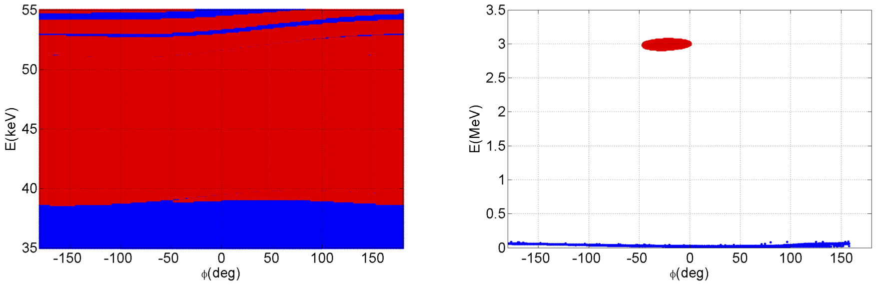

(a) (b)

Figure 3.10. The coordinates of the (a) input and (b) output particles in the longitudinal phase space.

structure, the beam current has a big effect on the dynamics of the beam. For this reason, the zero current acceptance plots and the nominal input beam phase space plots of the MEBT are not compared.

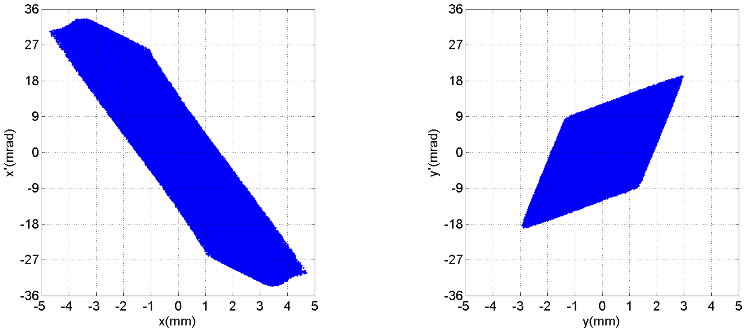

(a) (b)

Figure 3.11. MEBT acceptance plots: (a) horizontal plane, (b) vertical plane.

In case of errors, the cumulative probability for the change of acceptance is given in Figure 3.12 for the two transverse planes. In the cumulative probability plots, vertical axis shows the probability that the maximum change in acceptance will be less than or equal to the corresponding value on the horizontal axis. For example, for the MEBT line, with 70 per cent probability, decrease in the horizontal acceptance would be no more than 2.5 per cent. Negative values of the curve indicate the decrease of the acceptance and positive values of the curve indicate the increase of the acceptance. Expected values for the decrease in the transverse acceptance, due to misalignment, are 2.1 per cent for the horizontal plane and 2.0 per cent for the vertical plane.

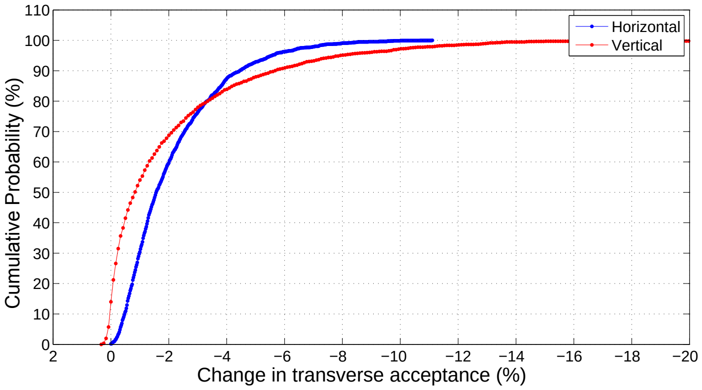

Figure 3.12. The horizontal and vertical cumulative probability plot for the change in MEBT transverse acceptance.

The longitudinal acceptance of the MEBT line is 9.0 deg.MeV. Figure 3.13 compares the nominal input particle distribution and the acceptance plot in the longitudinal phase space.

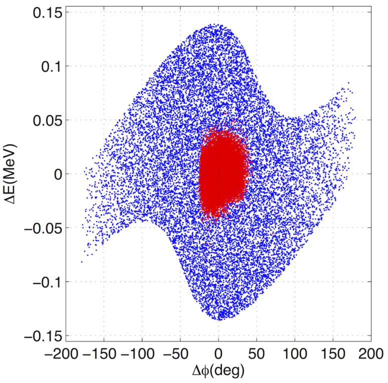

Figure 3.13. Comparison of the nominal input particle distribution for the MEBT and the acceptance plot in the longitudinal phase space.

3.2.4. Drift Tube Linac

The horizontal acceptance of the DTL is 14.8 mm.mrad and the vertical acceptance is 15.2 mm.mrad. Figure 3.14 compares the nominal input particle distribution for the DTL and the acceptance plot in the transverse phase space.

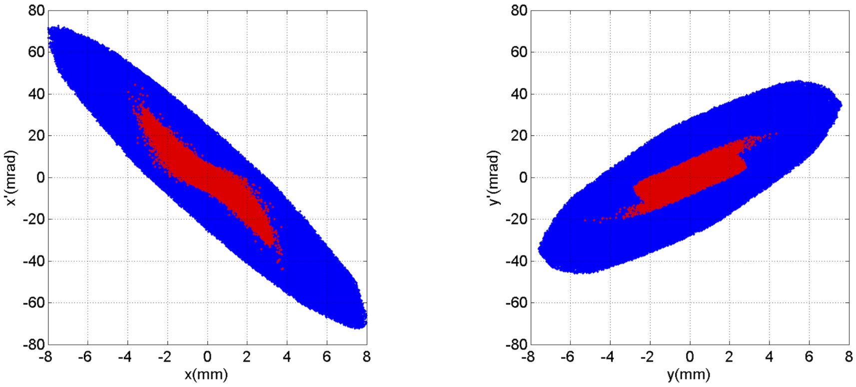

(a) (b)

Figure 3.14. Phase spaces of the nominal input beam and DTL acceptance plots: (a)horizontal plane, (b)vertical plane.

Figure 3.15 shows the plot of cumulative probability for change in the transverse acceptance of the DTL due to errors. The expected value for the decrease in the transverse acceptance of the DTL is 14.1 per cent for both transverse planes. The acceptance of the DTL decreases significantly with the alignment errors. The drift tubes of the DTL tanks must be mounted to the tanks with extra care to keep the errors as small as possible.

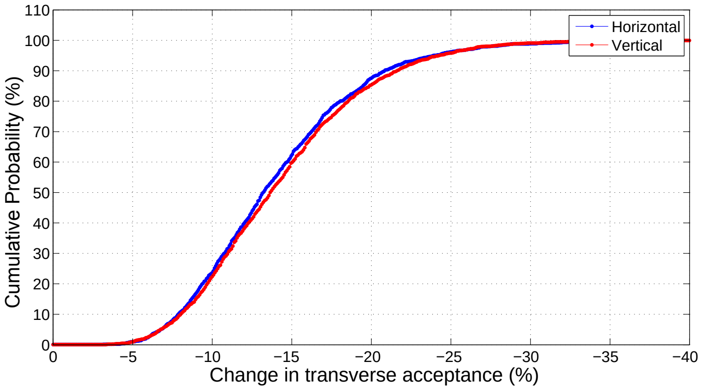

Figure 3.15. The horizontal and vertical cumulative probability plot for the change in DTL transverse acceptance.

Longitudinal acceptance of the DTL is 9.5 deg.MeV. Figure 3.16 compares the nominal input particle distribution and the acceptance plot in the longitudinal phase space.

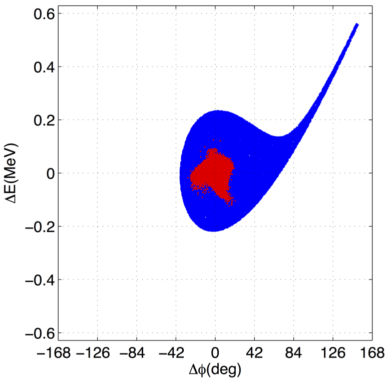

Figure 3.16. Comparison of the nominal input particle distribution for the DTL and the acceptance plot in the longitudinal phase space.

3.2.5. Cell-Coupled Drift Tube Linac

The horizontal acceptance of the CCDTL is 15.8 mm.mrad and the vertical acceptance is 16.0 mm.mrad. Figure 3.17 compares the nominal input particle distribution for the CCDTL and the acceptance plot in the transverse phase space.

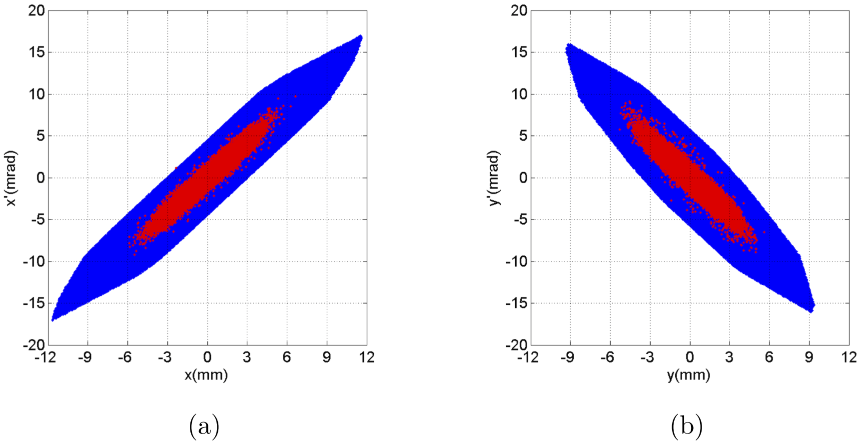

(a) (b)

Figure 3.17. Phase spaces of the nominal input beam and CCDTL acceptance plots: (a)horizontal plane, (b)vertical plane.

Figure 3.18 shows the plot of cumulative probability for change in the transverse acceptance of the CCDTL due to misalignment. Expected values for the decrease in the transverse acceptance of the CCDTL due to errors are 2.2 per cent for the horizontal plane and 2.3 per cent for the vertical plane.

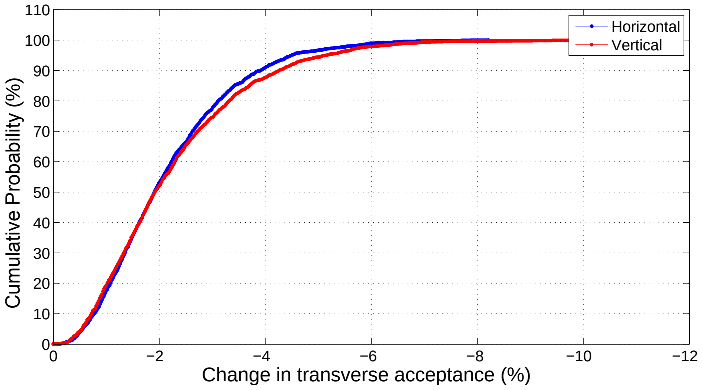

Figure 3.18. The horizontal and vertical cumulative probability plot for the change in CCDTL transverse acceptance.

Longitudinal acceptance of the CCDTL is 27.0 deg.MeV. Figure 3.19 compares the nominal input particle distribution and the acceptance plot in the longitudinal phase space.

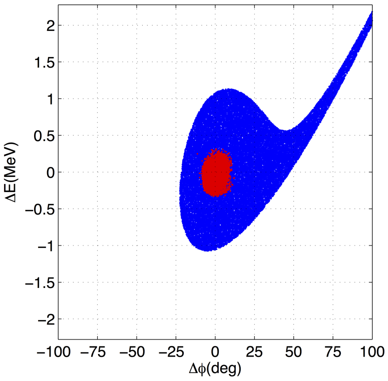

Figure 3.19. Comparison of the nominal input particle distribution for the CCDTL and the acceptance plot in the longitudinal phase space.

3.2.6. Pi-Mode Structure

The horizontal acceptance of the PIMS is 28.7 mm.mrad and the vertical acceptance is 28.4 mm.mrad. Figure 3.20 compares the nominal input particle distribution for the PIMS and the acceptance plot in the transverse phase space.

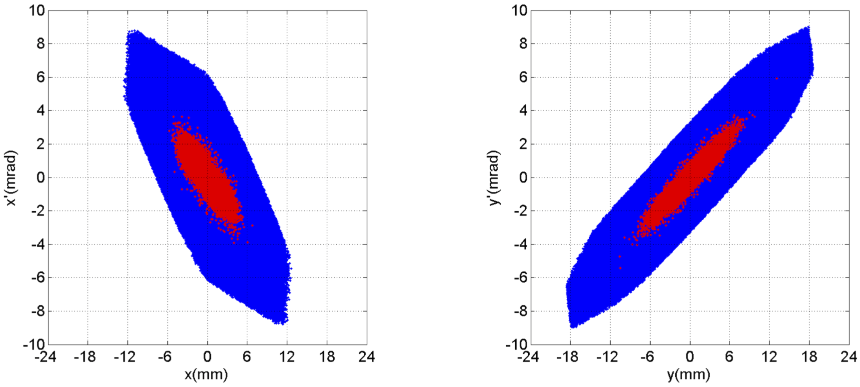

(a) (b)

Figure 3.20. Phase spaces of the nominal input beam and PIMS acceptance plots: (a)horizontal plane, (b)vertical plane.

Figure 3.21 shows the plot of cumulative probability for change in the transverse acceptance of the PIMS due to misalignment. Expected values for the decrease in the transverse acceptance of the PIMS due to errors are 1.0 per cent for the horizontal plane and 0.9 per cent for the vertical plane.

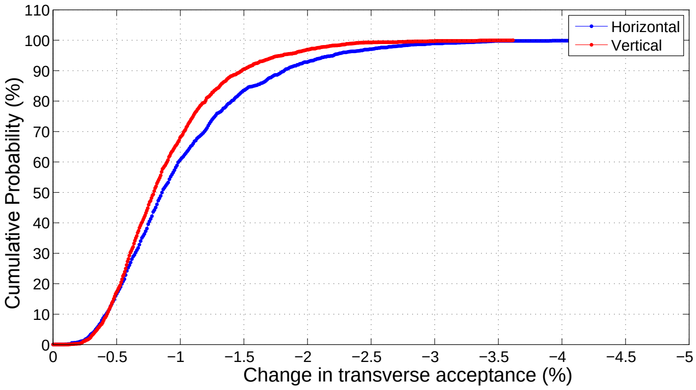

Figure 3.21. The horizontal and vertical cumulative probability plot for the change in PIMS transverse acceptance.

Longitudinal acceptance of the PIMS is 65.0 deg.MeV. Figure 3.22 compares the nominal input particle distribution of the PIMS and the acceptance plot in the longitudinal phase space.

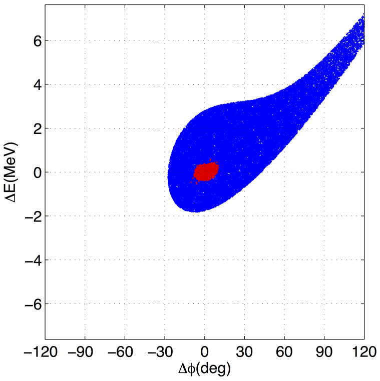

Figure 3.22. Comparison of the nominal input particle distribution for the PIMS and the acceptance plot in the longitudinal phase space.

3.2.7. The Acceptance Along Linac4

The zero current transverse and longitudinal acceptance of the individual structures of Linac4 have been studied. Figure 3.23a shows the transverse acceptance of the individual structures along Linac4. Likewise, Figure 3.23b shows the longitudinal acceptance of the individual structures. As it can be seen from the figures, the bottleneck for acceptance occurs at the low energy part of Linac4. Acceptance of the structures at the high energy end is significantly larger than the ones at low energy. Having a bigger acceptance at the higher energy part of the linac decreases the risk of loosing particles at high energies and therefore the risk of activation.

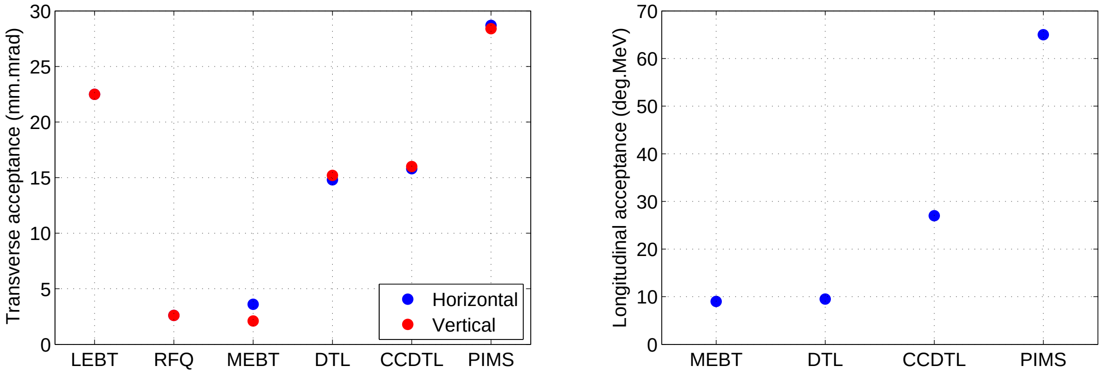

(a) (b)

Figure 3.23. Acceptance along Linac4 in (a) transverse planes and (b) longitudinal plane.

4. BACKTRACKING A MULTI-PARTICLE BEAM

Most of the time, the particle beam is tracked towards the high energy end of a linac. However, in some cases, it is also beneficial to track the beam towards the lower energy end. Starting with a description of a particle beam at a specific location along the linac and tracking the beam upstream, towards the low energy end is called backtracking.

Through a linear accelerator, motion of the charged particle beam is modeled using tracking codes (in this case, multi-particle tracking codes). If the physical laws used in a tracking code is invariant under time reversal, the same code, without any modification, can be used for backtracking. Utilizing the time reversal invariance of classical electromagnetic theory, a method was developed for backtracking a multi-particle beam, tested for low beam energies and used during the LEBT and the MEBT[2] commissioning [33, 34, 35].

Initially, the idea was considered for backtracking a multi-particle beam generated using the emittance measurement data obtained from a direct emittance measurement device (see Section 5.4.1). However, it will be discussed that, the method can also be used for testing the accuracy of the tracking code or technique and optimizing some parameters for simulations. Also, it will be discussed in Chapter 6 that backtracking can also be used for estimating the space charge compensation factor.

The following sections discuss the application of the time reversal invariance of classical electromagnetic theory on backtracking, the basics of the backtracking method and the accuracy of the method through different beam line elements.

---

[2] The relativistic beta, β_r, in the LEBT (45 keV) and in the MEBT (3 MeV) is around 0.01 and 0.08, respectively.

4.1. Time Reversal and Backtracking

Imagine that the motion of a particle was recorded as a movie. One can observe the evolution of its position and velocity in time by playing the movie forward. If, at any instant, the movie is paused and played backwards, the velocity of the particle would reverse and the particle would follow its trajectory backwards and end up at its initial position with a velocity opposite to its initial velocity. The speed of the particle at any position in space would be the same for the forward and the backward played movie. If this backward motion of the particle is allowed by the physical law which governs the motion of the particle, then, this certain physical law is said to be invariant under time reversal. In other words, if this physical law is invariant under time reversal, an observer, who does not have any prior information about the motion of the particle, can not tell if the movie is played backwards or forwards. Pausing the movie and playing it backwards can be imagined as time reversal operation.

4.1.1. Backtracking Procedure

In the case of a lossless system, where the interaction between the particles does not involve retarded potentials, classical electromagnetic theory is invariant under time reversal [36, 37]. Therefore, if a system is evolved in time, under the laws of classical electromagnetic theory, from an initial state, $\mathbf{S_i}$, to a final state, $\mathbf{S_f}$, one can start from $\mathbf{S_f}$ and use again the laws of classical electromagnetic theory to calculate $\mathbf{S_i}$. The forward evolution of a system in time and the process of backtracking is summarized in Figure 4.1, where **T** and **TS** represent the time reversal operator and the time-reversed state respectively.

Imagine that it took Δt time for the system to evolve from $\mathbf{S_i}$ to $\mathbf{S_f}$. Then, the procedure for backtracking is as follows:

- Apply the time reversal operator to the final state of the system to calculate time-reversed final state, $\mathbf{TS_f}$.
- Let the system evolve for a time interval Δt from the state $\mathbf{TS_f}$ to state $\mathbf{TS_i}$.

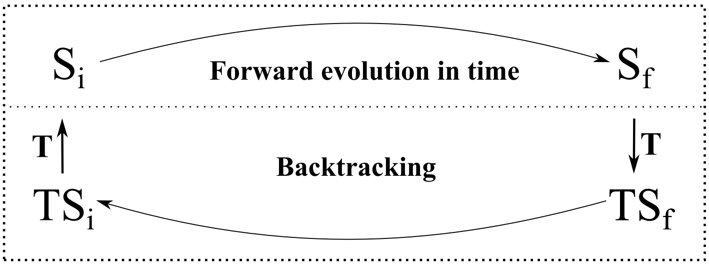

Figure 4.1. Evolution of the system in time and backtracking.

- Apply the time reversal operator to the state $\mathbf{TS_i}$ in order to find the initial state, $\mathbf{S_i}$, of the system[3] .

4.1.2. Transformation under Time Reversal Operation

Let us consider a charged particle bunch in an accelerator. At any time, the state (instantaneous state) of this particle bunch can be fully described by the position, velocity, charge and the mass of each particle. The mass, charge and the position ($\vec{r}$) of the particles are invariant under time reversal. The velocity ($\vec{v}$) of each particle flips sign as in Equation 4.2, where $\xrightarrow{\mathbf{T}}$ represents the transformation under time reversal operation.

$$\vec{r} \xrightarrow{\mathbf{T}} \vec{r} \tag{4.1}$$

$$\vec{v} \xrightarrow{\mathbf{T}} -\vec{v} \tag{4.2}$$

If the beam is backtracked only through a drift space, the transformations in Equation 4.1 and Equation 4.2 would be sufficient. However, if the particles are interacting with the external fields, which is not generated by the beam itself, the transformation of these fields should be considered for backtracking. Therefore, let us consider the whole accelerator as a system and see how the fields transform under time reversal. The transformations in Equation 4.1 and Equation 4.2 apply to each charged particle in the system.

---

[3] Notice that the time reversal operator is unitary: $\mathbf{TT} = \mathbf{I}$ where $\mathbf{I}$ is the identity operator.

One should first consider the transformation of charge density and current density to see how the fields transform under time reversal. The charge density, ρ, depends on the position of the particles, therefore it is invariant under time reversal (Equation 4.3). However, the current density, $\vec{J}$, depends on the velocity of the particles, therefore flips sign under time reversal (Equation 4.4).

$$\rho \xrightarrow{\mathbf{T}} \rho \tag{4.3}$$

$$\vec{J} \xrightarrow{\mathbf{T}} -\vec{J} \tag{4.4}$$

Considering the transformation of ρ and $\vec{J}$, it can be shown that the electric and the magnetic fields transform as in Equation 4.5 and Equation 4.6.

$$\vec{E} \xrightarrow{\mathbf{T}} \vec{E} \tag{4.5}$$

$$\vec{B} \xrightarrow{\mathbf{T}} -\vec{B} \tag{4.6}$$

Equation 4.5 and Equation 4.6 indicate that, at any location in space, if a particle feels certain electric and magnetic fields during forward evolution, that particle should feel the same electric field but opposite magnetic field during backtracking. Therefore, in addition to the properties of the particles, for backtracking, the properties of the beam line elements may also need to be modified to satisfy the transformation of the electric and the magnetic fields.

4.2. Modifying the Beam and the Beam Line for Backtracking

Backtracking of a multi-particle beam requires some changes to the particle coordinates and to some of the beam line elements. The following sections discuss the necessary modifications and the effects of the space charge forces on backtracking.

4.2.1. Coordinate System and Inverting the Beam Direction

The first step for backtracking is to apply the time reversal operation which requires modification of the coordinates of all the particles according to Equation 4.1 and Equation 4.2. This operation can be considered as inverting the beam direction. During the modification, the coordinate system of the multi-particle tracking code, which is used for the simulations, should be taken into account. Like most of the tracking codes, PATH uses a coordinate system where the direction of the axes depends on the beam direction. Figure 4.2 shows coordinate systems for forward tracking (the beam travels to the right) and backtracking (the beam travels to the left). In the figure, $\mathbf{\hat{x}}, \mathbf{\hat{y}}$ and $\mathbf{\hat{z}}$ are the unit vectors in the direction of +x, +y and +z, respectively.

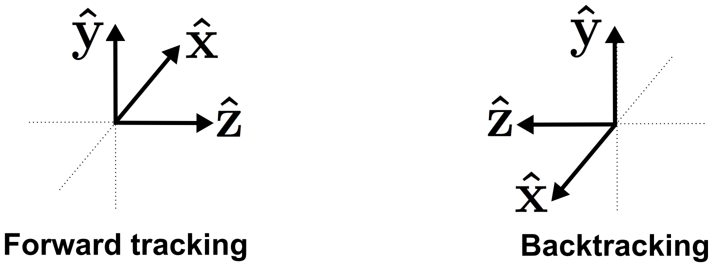

Figure 4.2. Coordinate systems for forward tracking and backtracking.

As it can be seen from Figure 4.2, $\mathbf{\hat{z}}$ always points in the beam direction. Therefore, the x and z axes change direction when the beam direction is inverted. According to Equation 4.1, Equation 4.2 and the coordinate systems shown in Figure 4.2, in order to invert the beam direction, coordinates of all the particles should be modified as follows:

- $x \rightarrow -x$
- $x' \rightarrow x'$
- $y \rightarrow y$
- $y' \rightarrow -y'$
- $\Delta\phi \rightarrow -\Delta\phi$
- $\Delta p \rightarrow \Delta p$

The modifications listed above can be applied to the beam by introducing an element to the beam line with length zero and transfer matrix, $\boldsymbol{R_{inv}}$, as shown in Equation 4.7.

As a last step of backtracking, the beam direction should be inverted again in order to obtain a beam traveling to the high energy end.

$$\boldsymbol{R_{inv}} = \begin{bmatrix} -1 & 0 & 0 & 0 & 0 & 0 \\ 0 & 1 & 0 & 0 & 0 & 0 \\ 0 & 0 & 1 & 0 & 0 & 0 \\ 0 & 0 & 0 & -1 & 0 & 0 \\ 0 & 0 & 0 & 0 & -1 & 0 \\ 0 & 0 & 0 & 0 & 0 & 1 \end{bmatrix} \tag{4.7}$$

4.2.2. Modification of the Beam Line Elements

Backtracking requires a description of the beam line elements in reversed order. For instance, the last element that the particles pass through during forward evolution should be the first element for backtracking. Considering the reversed order of motion, properties of the beam line elements may also need to be modified to adapt the fields for backtracking according to the new coordinate system. Some of the beam line elements and the required modifications are discussed below.

4.2.2.1. Drift Space. Through a drift space, particles do not feel any external fields. Therefore, no modification is needed.

4.2.2.2. Solenoid Magnet With a Field Map. PATH uses field maps which have the three dimensional description of the fields of solenoid magnets. For backtracking, the field map of a solenoid should be modified to reverse the magnetic field according to

Equation 4.6 and adapt the fields to the new coordinate system. Figure 4.3a shows the direction of the magnetic field lines of a solenoid magnet when particles pass through it. Figure 4.3b shows the magnetic field lines of the same solenoid magnet for backtracking.

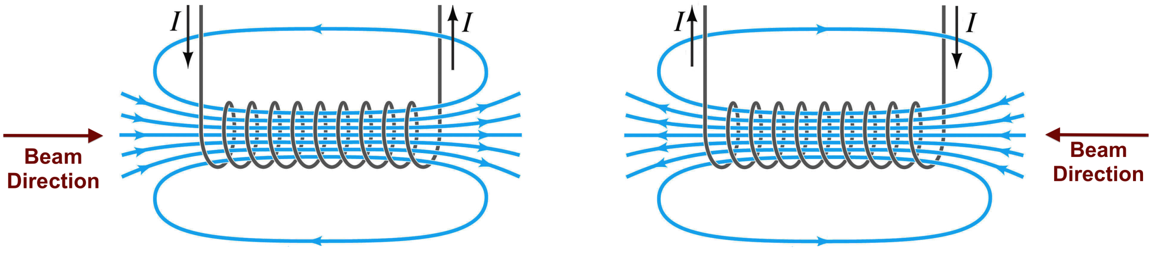

(a) (b)

Figure 4.3. (a) Direction of the solenoid magnetic field. (b) Reversed magnetic field direction for backtracking.

Backtracking through the solenoid field map means that, as in Figure 4.3b, the particles would enter the solenoid magnet from the right end and exit from the left end. Therefore, the field map for backtracking should assume that the z coordinate starts at the right end of the magnet and extends towards left end. Assuming that the description of the field map starts at $z = 0$ and finishes at $z = L$, for backtracking, the field map of a solenoid with radial symmetry should be modified as follows:

- $z \to L - z$
- $r \to r$
- $B_z \to B_z$
- $B_r \to -B_r$

Notice that the modifications on the field map are not only required to satisfy the transformation in Equation 4.6 but also to adapt the transformed magnetic field into the coordinate system used in the tracking code.

<u>4.2.2.3. Quadrupole Magnet.</u> PATH requires a minimum of three parameters for the quadrupole magnets: length, pole tip field with a sign[4] and pole tip radius. Figure

---

[4] The sign defines if the magnet is focusing or defocusing in the horizontal plane.

4.4a shows the direction of the field lines of a focusing quadrupole magnet in x-z plane (for a positively charged particle). For backtracking, the magnetic field lines should be reversed as in Figure 4.4b.

As it can be seen from Figure 4.4, the quadrupole magnet has a focusing effect in both directions. Likewise, a defocusing quadrupole magnet would be defocusing in both directions. Therefore, for backtracking, no modification is required on the description of a quadrupole magnet.

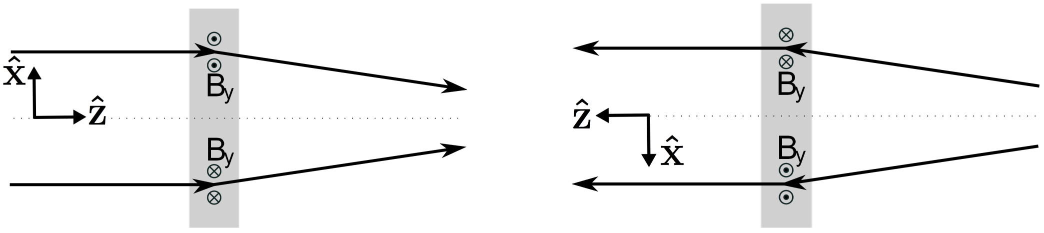

(a) (b)

Figure 4.4. Effect of a focusing quadrupole magnet on the particles: (a) evolution in time, (b) backtracking.

4.2.3. Beam Self-Generated Fields

As the beam travels in the accelerator, the charge and current of the beam create self-fields which effects the beam itself. The effect of self-generated fields should be considered during backtracking. Like external fields, the transformation of self-generated fields should satisfy Equation 4.5 and Equation 4.6.

If the trajectory and the velocity of the particles are calculated accurately during backtracking, the charge density and the current density follow the transformations shown in Equation 4.3 and in Equation 4.4. Therefore, during backtracking, self-generated fields calculated by the tracking code naturally follow the transformations given in Equation 4.5 and Equation 4.6. As a result, at any z location along the beam line, particles feel the same force during forward evolution and backtracking. However, an error in the calculation of position and velocity will result in error in the calculation of self-generated fields and force which will amplify the position and velocity error later on. This effect may be small for the low current beams however it may cause large errors for high current beams. Therefore, the longitudinal step size and the mesh size for space charge calculation should be chosen small enough to have accurate calculation.

4.3. Backtracking through Different Elements

The backtracking method was tested by tracking multi-particle beams first forwards and then backwards through an element or a set of elements. The procedure summarized in Figure 4.1 was followed step by step. An initial particle distribution (initial state) was tracked forward through an element and the beam distribution after the element (final state) was obtained. After that, the beam was first inverted (time reversed final state) and backtracked through the same element to obtain the distribution at the initial location (time reversed initial state). Then, as a final step, the beam was inverted again to obtain the initial particle distribution.

The coordinates of each particle before and after the simulations were compared to see the accuracy of the method. No aperture constraints were set to avoid the particle losses so that to have an accurate comparison. For a visual comparison, the phase spaces of the initial and the final beams were plotted together. For statistical error analysis, the shift in the coordinates of each particle was calculated and the data were binned to get the error distribution. Then, the mean and the standard deviation (rms) of the error distribution were calculated. If the method works well and the particles come back to their initial positions in the phase spaces, one expects to have an error distribution with both the mean and rms equal to zero.

The method was tested at two different beam energies, 45 keV (LEBT energy) and 3 MeV (MEBT energy). At 45 keV the method was tested by tracking a beam through a 60 cm long solenoid field map and also through a 100 cm long drift space. At 3 MeV, the beam was tracked through the whole MEBT line (about 3.9 m length) which contains 11 quadrupole magnets. The MEBT RF cavities were switched off for the simulations. The effect of space charge forces were studied with the simulations concerning the drift space at 45 keV and MEBT at 3 MeV. The PATH and TraceWin codes were used for the simulations. TraceWin was used only for the solenoid simulations and PATH was used for all the other cases.

4.3.1. Tracking at 45 keV Beam Energy

A multi-particle H^- beam with 5000 particles was generated with average energy of 45 keV and energy spread of ±0.6 keV. The beam coming from the ion source and passing through the LEBT is unbunched and has a radial symmetry. Therefore, for the generated input beam, the distribution of the particles in the horizontal and vertical phase spaces are similar and the longitudinal phase spread is ±180°. Figure 4.5 shows the phase spaces of the generated beam. The same initial beam was tracked through the solenoid and the drift space, independently.

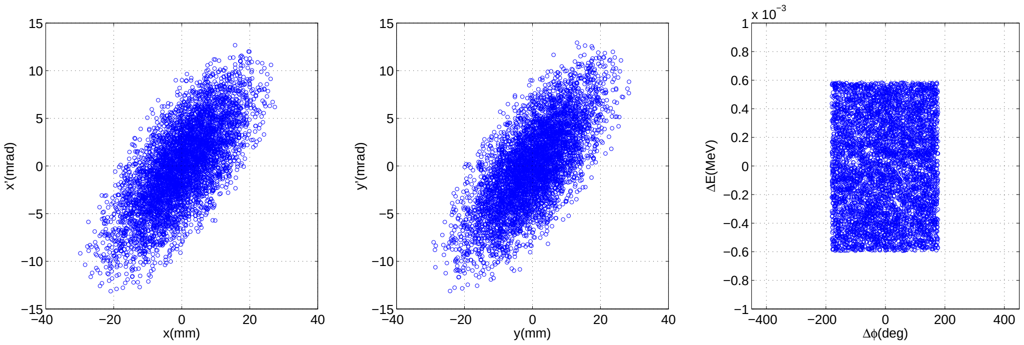

(a) (b) (c)

Figure 4.5. Phase spaces of the initial beam for 45 keV simulations: (a) horizontal phase space, (b) vertical phase space and (c) longitudinal phase space.

4.3.1.1. Backtracking through a Solenoid Field Map. The Linac4 LEBT solenoid magnetic field map was used for the simulations. The field map has a radial symmetry. The radial mesh size is 1 mm and the longitudinal mesh size is 2 mm. For the simulations, the field strength was chosen in such a way that the beam size would change significantly through the field map to amplify any possible errors. The beam current was set to zero to ignore the interaction between the particles. Figure 4.6 shows the evolution of rms beam size in transverse planes through the solenoid as well as the horizontal and longitudinal phase space of the beam after the solenoid. As it can be seen from Figure 4.6a, the change of horizontal and vertical beam size is the same. This is due to the radial symmetry of the particle distribution. Horizontal and vertical phase spaces are similar all along the field map, therefore, only the horizontal phase space will be shown in the figures.

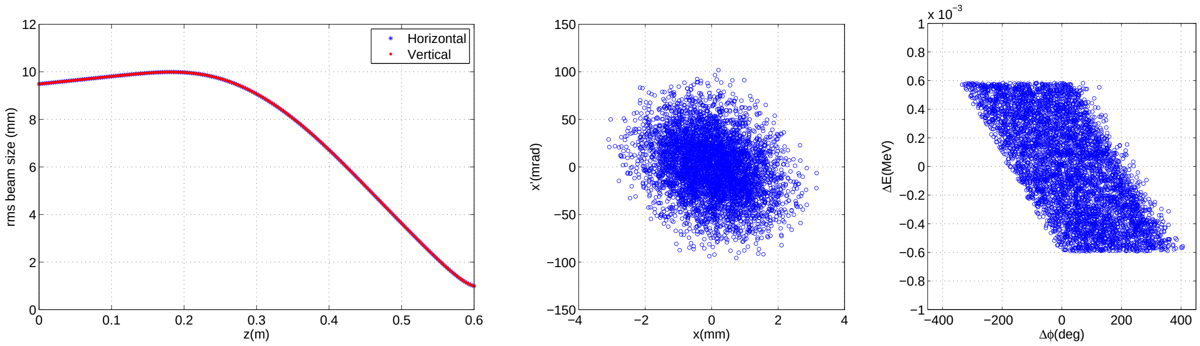

(a) (b) (c)

Figure 4.6. (a) Evolution of x_{rms} and y_{rms} during forward tracking through the solenoid. (b) Horizontal phase space and (c) longitudinal phase space of the beam after the solenoid field map.

The beam distribution after the solenoid was inverted as explained in section 4.2.1 and then tracked back to the solenoid entrance. Figures 4.7a and 4.7b show the horizontal and longitudinal space of the inverted beam before backtracking. Comparing Figure 4.6b and Figure 4.7a, one can see that the converging beam after the solenoid becomes diverging after inverting the beam direction. Likewise, it can be seen from Figures 4.6c and 4.7b, after beam inversion the tail of the bunch becomes the head, and vice versa. Figure 4.7c shows the evolution of the rms beam size in transverse planes during backtracking. As it can be seen, this plot is just the reverse of the one shown in Figure 4.6a.

After obtaining the beam at the solenoid entrance, as a last step of backtracking, the beam was inverted again and then compared to the initial beam. Figure 4.8 shows the comparison of the initial and final particle distributions in the horizontal and longitudinal phase spaces. As it can be seen from the figure, the particles come to their original coordinates in the phase spaces after tracking through the solenoid and

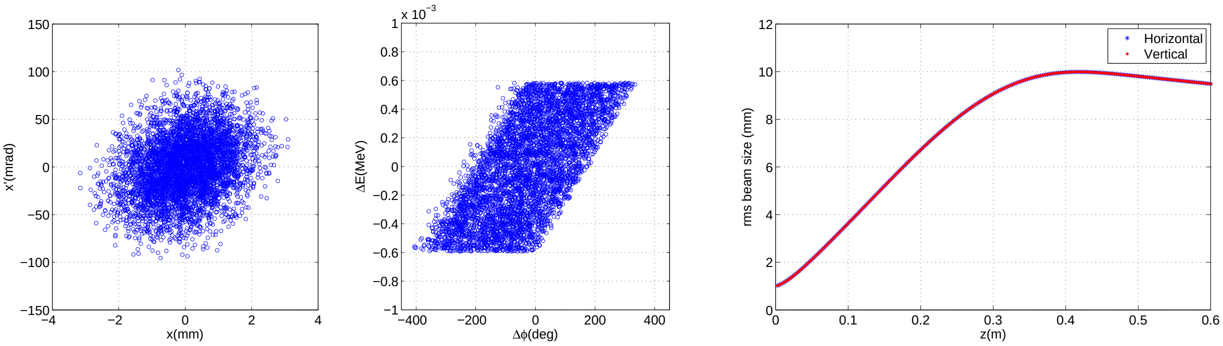

(a) (b) (c)

Figure 4.7. (a) The horizontal phase space and (b) longitudinal phase space of the inverted beam before tracking back to the solenoid entrance. (c) The evolution of x_{rms} and y_{rms} during backtracking.

then backtracking.

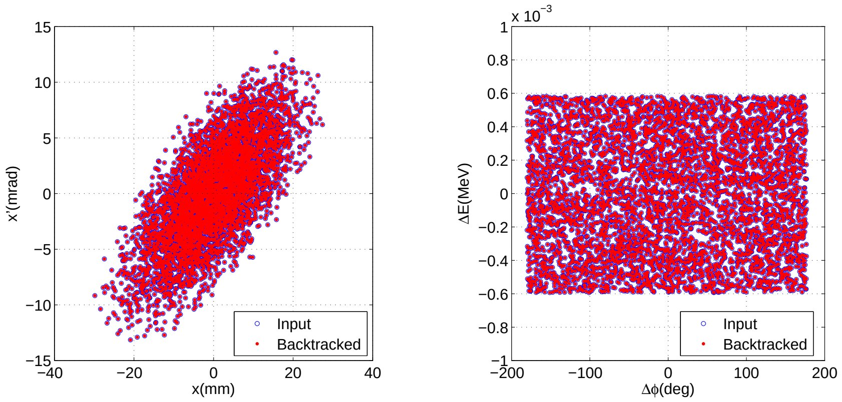

(a) (b)

Figure 4.8. Phase spaces of the initial and final beams after backtracking through the solenoid field map: (a) horizontal phase space, (b) longitudinal phase space.

Figure 4.9 gives a quantitative and more accurate comparison of the initial and the backtracked beam. Figures 4.9a and 4.9b show the error distribution for x and $\Delta\phi$, respectively. The mean and rms of each distribution are indicated on the corresponding plot. Error distribution of vertical position, y is similar to the error distribution of x with mean= $9.5 \cdot 10^{-9}$ mm and rms= $6.6 \cdot 10^{-7}$ mm. None of the particles have any error in x', y' or ΔE. In the beam file of TraceWin, the number of decimal places is six. Therefore, taking into account the rounding errors, the mentioned errors are consistent with zero.

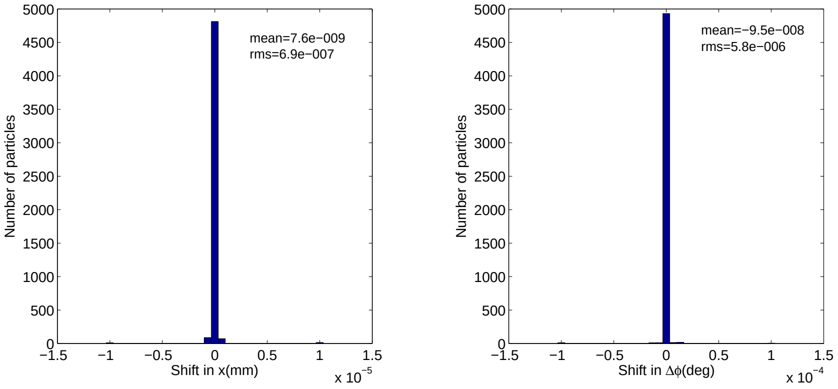

(a) (b)

Figure 4.9. Error distributions after backtracking through the solenoid field map for: (a) horizontal position and (b) longitudinal phase.

4.3.1.2. Backtracking through a Drift Space. For the simulations concerning the drift space with 45 keV beam energy, the initial particle distribution is the same with the distribution used for the solenoid simulations (see Figure 4.5). The step size of calculation in longitudinal direction was set to 5 mm. For the space charge calculations, number of mesh intervals were set to 100 both the longitudinal and radial directions.

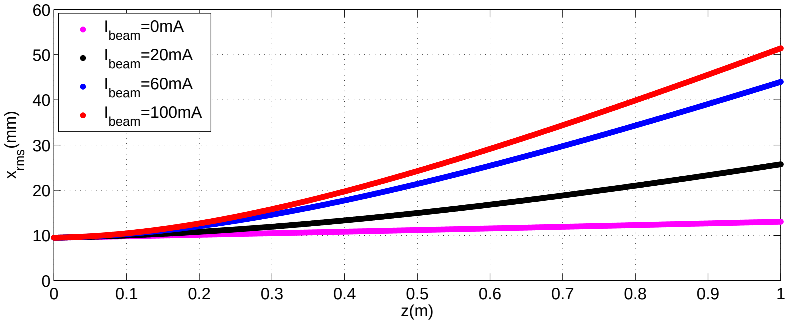

Figure 4.10. The evolution of the horizontal rms beam size along the drift space during forward tracking for various beam currents.

The beam current was varied up to 100 mA to test the backtracking method by including the space charge forces. Figure 4.10 shows the evolution of the horizontal rms beam size along the drift space (forward tracking) for various beam currents. As it can be seen from the figure, increasing the beam current results in bigger beam size at the end of the drift space due to higher space charge forces.

When the beam current was set to zero to ignore the space charge forces, the error distributions for x and $\Delta\phi$ were obtained as in Figure 4.11a and 4.11b. The error distribution of y has a mean of $2.1 \cdot 10^{-19}$ mm and rms of $6.6 \cdot 10^{-17}$ mm. Both the mean and rms of the error distributions for x', y' and ΔE are zero. Through a drift space, when there are no space charge effects, particles follow a straight path, therefore transverse angles are kept constant. Likewise, the energy of the particles stays constant. However, the transverse position and longitudinal phase of particles are computed at each step of calculation. The number of decimal places used in the beam file of PATH is 15. When this number is compared to the order of magnitude of the errors[5] shown in Figure 4.11, it can be concluded that the errors are small enough to be generated only from rounding of the numbers during the computation.

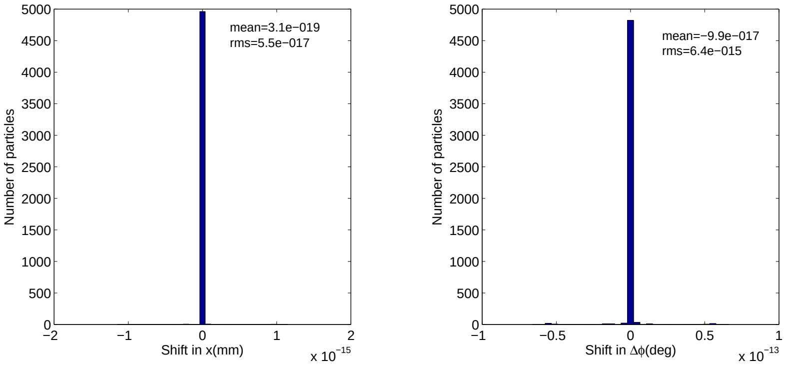

(a) (b)

Figure 4.11. Error distributions after backtracking through the drift space with $I_{\text{beam}} = 0$ mA: (a) for x and (b) for $\Delta\phi$.

Backtracking was tested with the same initial beam by varying the beam current. Figure 4.12 shows the rms of the error distributions for various beam currents up to 100 mA. For the transverse coordinates, the mean of the distributions is two orders of magnitude smaller than the rms value. For the phase, the mean is around one order of magnitude smaller (see Figure 4.14c). For an unbunched beam, the particles do not

---

[5] Notice that two orders of magnitude difference in position and phase errors comes from the conversion of units from radians to degrees.

feel any longitudinal force. Therefore, both the mean and rms of the error distribution for ΔE are equal to zero.

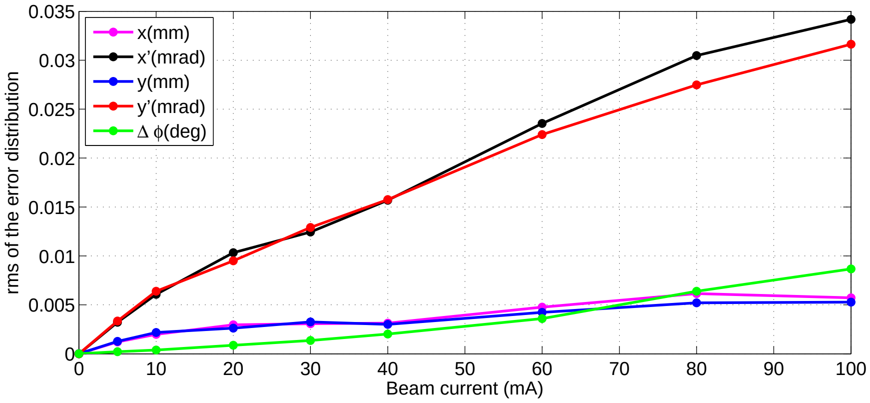

Figure 4.12. The rms values of the error distributions for backtracking through 45 keV drift space with various beam current.

The errors presented in Figure 4.12 show that the accuracy of the method decreases as the beam current increases. Nevertheless, even for a beam with 100 mA of current, the errors are not high and the backtracking method can still be applied. In addition, due to the procedure of the test, the results listed in Figure 4.12 are the cumulative effect of both forward tracking and backtracking. Therefore, the errors are overestimated. It is also important to keep in mind that the result given in Figure 4.12 strongly depends on the accuracy of the space charge calculations (see Section 4.4).

The comparison of particle distributions of initial and backtracked beams with 100 mA current is given in Figure 4.13. The shift in coordinates of the particles is not significant enough to observe the difference.

Figure 4.14 shows the error distributions for x, x' and $\Delta\phi$ from backtracking with 100 mA beam current.

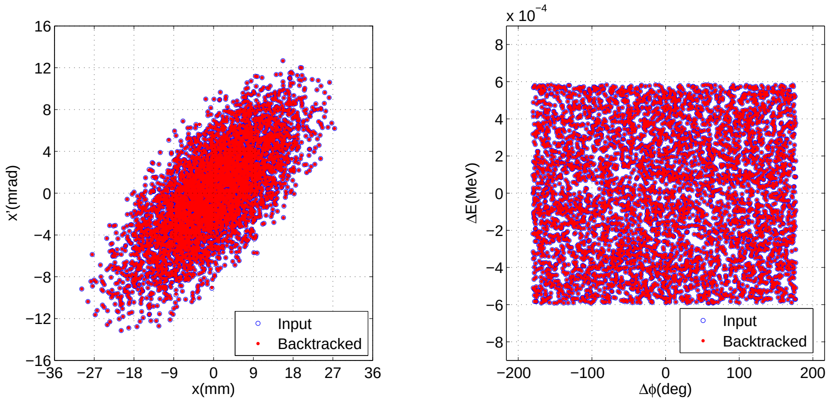

(a)

(b)

Figure 4.13. (a) The horizontal and (b) longitudinal phase spaces of the initial and final beams after backtracking ($\mathrm{I_{beam}} = 100$ mA) through the drift space.

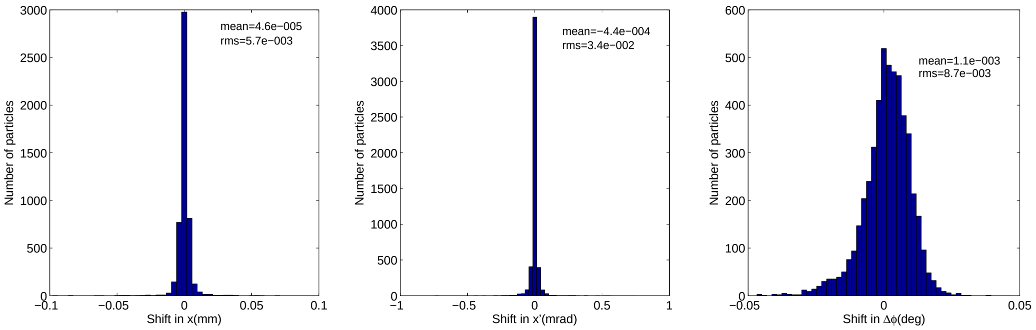

(a)

(b)

(c)

Figure 4.14. Error distributions after backtracking through the drift space with $\mathrm{I_{beam}} = 100$ mA: (a) for x, (b) for x' and (c) for $\Delta\phi$.

4.3.2. Tracking at 3 MeV Beam Energy

The beam obtained from the RFQ beam dynamics simulations was used as an input to the backtracking simulations. Phase spaces of the beam, which has around 36000 particles, are shown in Figure 4.15. As it can be seen from Figure 4.15c, the beam is bunched with phase and energy spread of around $\pm 20^\circ$ and ± 60 keV, respectively. The bunch frequency is 352.2 MHz. The calculation step size in longitudinal direction is 5 mm. For the space charge calculations, number of mesh intervals were set to 40 both in longitudinal and radial directions.

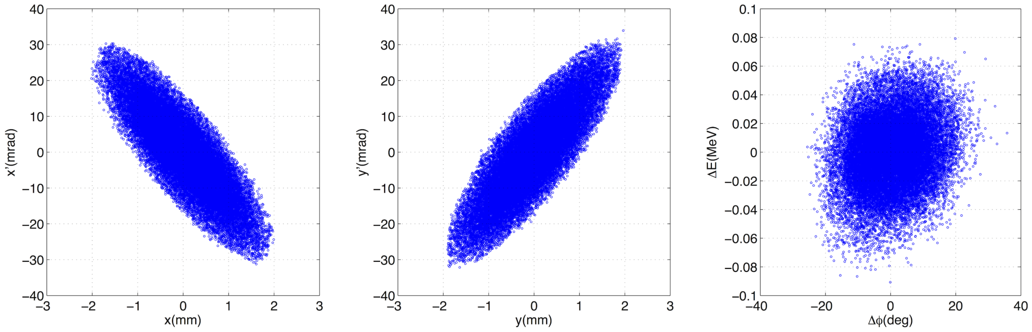

(a) (b) (c)

Figure 4.15. (a) The horizontal, (b) vertical and (c) longitudinal phase spaces of the initial beam for 3 MeV simulations.

As in the case of 45 keV simulations, the beam current was varied up to 100 mA and the error distributions for each case were calculated. The evolution of the transverse and longitudinal beam size along the beam line is different for each beam current. In the case of a bunched beam, because of the space charge forces, the energy spread of the bunch also gets bigger. The evolution of the energy spread along the beam line is strongly related to the beam current. Figure 4.16 shows the evolution of $\Delta\phi_{rms}$ and ΔE_{rms} along the MEBT for different beam currents during forward tracking.

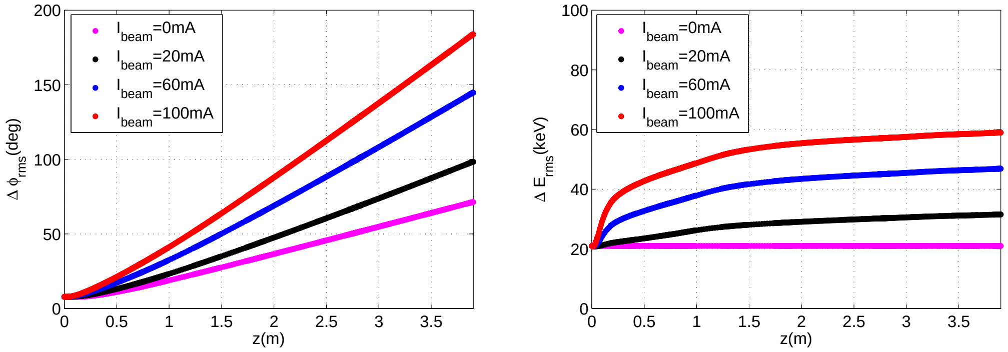

(a) (b)

Figure 4.16. The evolution of (a) phase rms and (b) energy rms along the MEBT for different beam currents.

The strength of the quadrupole magnets were kept the same for each beam current. Figure 4.17 shows, how x_{rms} and y_{rms} change along the MEBT during forward tracking for $I_{beam} = 0$ mA. Transverse beam size along the beam line also depends on the beam current.

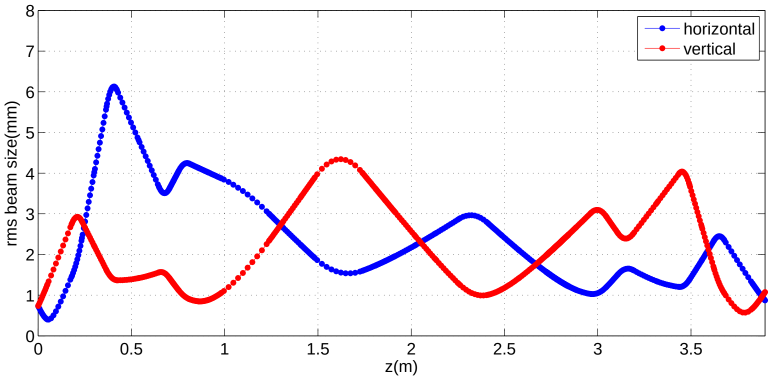

Figure 4.17. The evolution of transverse rms beam sizes along the MEBT during forward tracking for $I_{beam} = 0$ mA.

Figure 4.18 shows the rms of the error distributions calculated by comparing the initial and the backtracked beam for different beam currents. The mean values of the distributions are two or three orders of magnitude smaller than the corresponding rms values. As it can be seen from Figure 4.18b there is a shift also in the energy of the particles. Through the quadrupole magnets, the energy error amplifies the transverse position and the angle errors. Together with the energy error, the transverse errors contribute to the phase error.

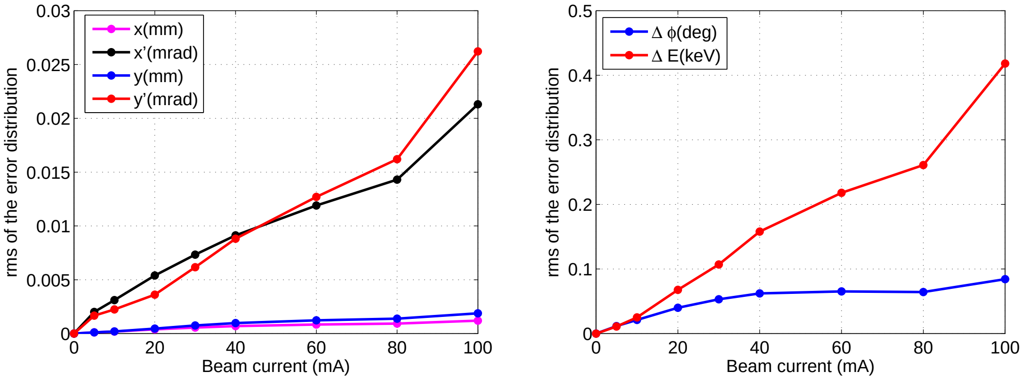

(a) (b)

Figure 4.18. The rms values of the error distributions for backtracking through MEBT at 3 MeV: (a) transverse coordinates (b) longitudinal coordinates.

When Figure 4.18 is compared to Figure 4.12, it can be seen that, at 3 MeV, in spite of the length and the complexity of the beam line, the errors in the transverse coordinates of the particles are not higher than the errors at 45 keV for the drift space case. The error in the longitudinal coordinates of the particles is small enough to have an accurate result from backtracking.

4.4. Other Applications

The backtracking method explained in this chapter can also be used for testing a tracking code, identifying the bugs in the code or checking the accuracy of the simulation method. For instance, when the beam current is set to zero, the only source of error should be rounding of the numbers during the computation. Therefore, backtracking can be used for testing the effect of the rounding errors. A similar method was used for checking the influence of rounding errors on the results of tracking calculations [38]. Likewise, if there is an unexpected error in the coordinates of the particles, this may indicate a bug in the code.

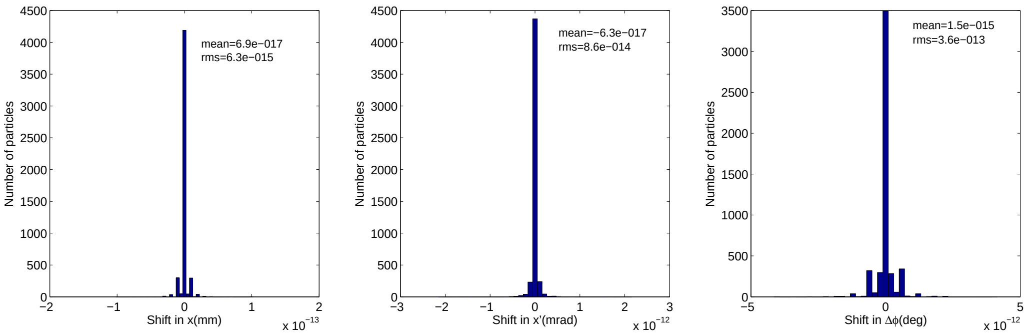

(a) (b) (c)

Figure 4.19. Error distributions after backtracking through the drift with $I_{\text{beam}} = 100$ mA at 45 keV beam energy using Coulomb's law for the space charge calculations: (a) for x, (b) for x' and (c) for $\Delta\phi$.

Backtracking can be used for testing the accuracy of the space charge calculations. As an example, the simulation through the drift space (Section 4.3.1.2) with 100 mA current at 45 keV beam energy was repeated by using the Coulomb's law routine [27] for the space charge calculations. Figure 4.19 shows the error distributions for x, x' and

$\Delta\phi$ obtained from backtracking using Coulomb's law. If the rms values in Figure 4.19 are compared to the rms values in Figure 4.14, it can be seen that the simulations using Coulomb's law for space charge calculations give much smaller errors. The rms of the error distributions for x, x' and $\Delta\phi$ are 12, 12 and 10 orders of magnitude smaller, respectively, when the Coulomb's law is used for the space charge calculations.

The accuracy of the space charge calculations depend on the number of radial and longitudinal mesh intervals (N_r^{sc} and N_l^{sc}, respectively). Using backtracking, one can check if the values defined for the number of mesh intervals give accurate results or find optimum values to be used for the simulations in order to have an accurate calculation with reasonable computation time. The forward tracking and backtracking process for the beam line described in Section 4.3.2 was repeated by varying the number of radial and longitudinal space charge mesh intervals for $\mathrm{I}_{\mathrm{beam}} = 40$ mA. First, a set of simulations were run by fixing N_r^{sc} to 50 and varying the N_l^{sc} from 10 to 100. Figure 4.20 shows the rms of the error distributions for backtracked beams obtained from the simulations with different N_l^{sc}. As it can be seen from the figures, there is a rapid decrease in the rms of the error distributions with increasing N_l^{sc}. However, when N_l^{sc} exceeds 40, the rms of the error distributions is more or less constant. Therefore, setting N_l^{sc} to a number larger than 40 will increase the computation time but not the accuracy.

For the second set of simulations, N_l^{sc} was kept constant at 40 and N_r^{sc} was varied from 10 to 100. Figure 4.21 shows the rms of the error distributions. As it can be seen from Figure 4.21a, for small values of N_r^{sc}, the accuracy of the simulation increases (in transverse planes) with increasing N_r^{sc}. However, for N_r^{sc} values greater than 30, the errors are almost constant. The errors for the longitudinal coordinates are more or less constant for each value of N_r^{sc} (see Figure 4.21b). Therefore, setting N_r^{sc} to a value larger than 30 will not improve the simulation accuracy but increase the computation time for this particular structure.

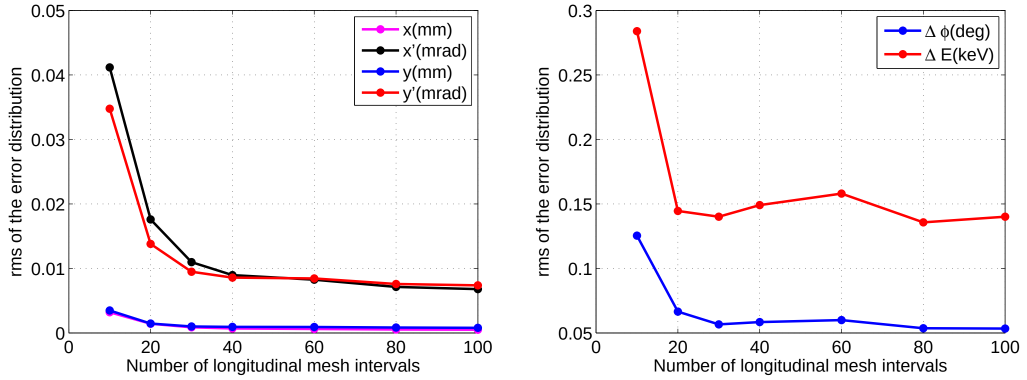

(a) (b)

Figure 4.20. The rms values of the error distributions for backtracking through MEBT ($I_{\text{beam}} = 40$ mA) with different longitudinal space charge mesh intervals: (a) transverse coordinates (b) longitudinal coordinates.

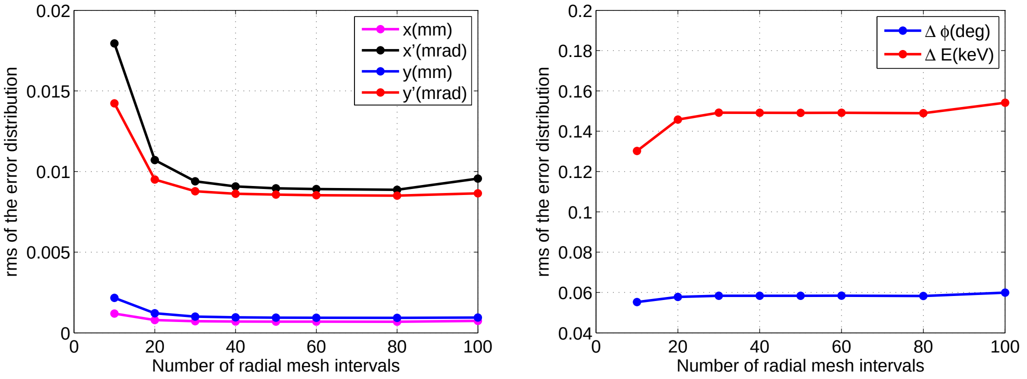

(a) (b)

Figure 4.21. The rms values of the error distributions for backtracking through MEBT ($I_{\text{beam}} = 40$ mA) with different space charge radial mesh intervals: (a) transverse coordinates (b) longitudinal coordinates.

4.5. Conclusion and Discussion

In this chapter, the backtracking method which uses the time reversal invariance of classical electromagnetic theory was discussed. The accuracy of the method through different beam lines and for several beam currents was tested using multi-particle tracking codes. Up to 100 mA beam current, it was shown that backtracking can be used both at 45 keV and 3 MeV beam energies with good accuracy. The method was not tested with higher beam currents simply because it is not applicable to Linac4. However, as it can be seen from Figure 4.19, even for 100 mA beam current at 45 keV energy, where the space charge forces are strong, the rms values of the error distributions are very small when Coulomb's law was used for the space charge computation. Therefore, it is expected that, for beam currents higher than 100 mA, the method should still work when an accurate space charge solver is used for the computation of the self forces.

Originally, the method was considered for backtracking the multi-particle beams generated based on the emittance measurement data. However, in this chapter, it was shown that, the method can also be used for testing the accuracy of the calculations and optimizing the parameters for simulations. It will be discussed in Chapter 6 that backtracking can also be used for estimating the space charge compensation factor.

5. LINAC4 BEAM DIAGNOSTICS AND MEASUREMENT METHODS

Beam diagnostics is essential for any accelerator both during the operation and the commissioning period. The diagnostic instruments for the operation can be used for a quick measurement of basic beam parameters to check the machine operation and stability. However, the diagnostic instruments for the commissioning of a linac should give reliable information about the complex beam behavior and help understanding the properties of the accelerator components in detail. Having reliable diagnostics instruments is crucial for a successful commissioning period for the development of a linac with higher performance.

There are various permanent diagnostic instruments along the Linac4 to be used during the operation. Along with the specific instruments for the commissioning, the permanent instruments were also used during the commissioning period.

Following sections explain the basic principle behind the operation of the diagnostic instruments and the measurement methods used at the Linac4 commissioning.

5.1. Measurement of the Beam Current

The electrical current of the beam is one of the most important parameters of a particle accelerator. During the beam commissioning of the Linac4, a first check always concerned the beam current. Measuring and comparing the beam current at the injection point of a structure and at the extraction point of the structure gives an indication of the transmission efficiency. At Linac4, there are two instruments used for the measurement of beam current, namely, the Faraday Cup and the beam current transformer (BCT).

5.1.1. Faraday Cup

Faraday Cups measure the beam current by measuring the total charge of the beam. All the particles are collected by an electrically isolated metallic electrode inside the Faraday Cup. Thus, measurement of beam current with a Faraday Cup is a destructive process. The charges, which are collected on the electrode, are integrated with a sensitive amplifier. Since all beam charges are collected for such a measurement, it is the most sensitive measurement possible for the beam current [39]. Sensitivity of the Faraday Cup makes it the ideal instrument at low beam intensities. Faraday Cups can also be used for high intensity beams, provided that there is cooling to carry away the heat generated by the beam collected in the Faraday Cup. Faraday Cups are mostly used at the low energy end of the linac. At high energies, Faraday Cups are not suitable because the particles have penetration depth of several centimetres and for the high intensity beams the total energy carried by the beam can be high enough to destroy the intercepting material [40].

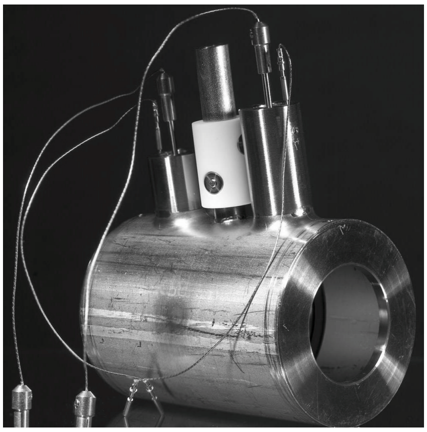

Figure 5.1. Picture of a Faraday Cup [41].

When a particle beam hits on the electrode of the Faraday Cup, secondary electrons are emitted from the surface. If the electrons escape the Faraday Cup, the measurement of the current will not be reliable. While measuring a positively charged beam the current will be overestimated and while measuring a negatively charged beam the current will be underestimated. In order to prevent these electrons from escaping the cup, a negatively polarized electrode (guard ring) is placed at the entrance of the cup. Figure 5.2a shows the potential around the guard ring. Its function is to push the electrons back onto the electrode (see Figure 5.2b). These secondary electrons typically have energies of few tens of electronvolts, such that relatively low polarization voltages are usually sufficient to repel them [39].

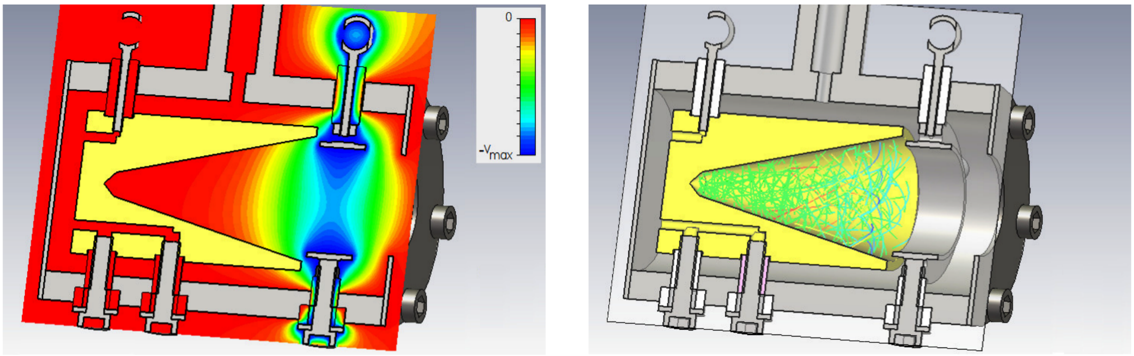

(a) (b)

Figure 5.2. Potential around the guard ring and suppression of the secondary electrons [42].

5.1.2. Beam Current Transformer

A moving charged particle beam creates magnetic and electric fields around it. One can measure the beam current indirectly by measuring these fields. A beam current transformer (BCT) is a device which measures the beam current using the induced magnetic field.

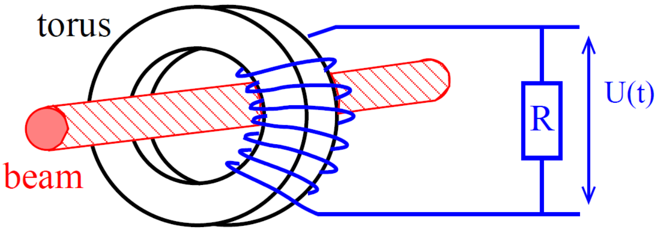

Figure 5.3. Simple representation of a BCT [40].

Figure 5.3 shows a simple model of a BCT. The beam acts as the primary winding of the transformer. When a beam pulse passes through the torus, it creates a time varying magnetic field. The field lines are guided by the magnetic material with very high permeability. There is an insulated wire which is wound around the torus as a secondary winding of the transformer. As the magnetic flux changes through the torus, a signal is induced on the wire and a time varying potential difference is generated across the resistor. This potential difference is measured to calculate the beam current. After the secondary winding of the transformer, a suitable capacitance and resistance network should be added, often coupled with an active amplification circuit [39]. The strength of the field created by the beam is extremely small. In order to have a reliable measurement, it is important to shield the system from the external magnetic fields.

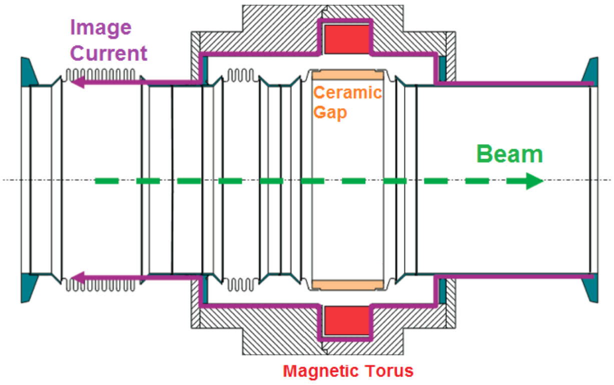

Figure 5.4. The ceramic gap and the path of the image current around the torus [39].

When a charged particle beam travels inside a conducting vacuum chamber, it induces an image current which has the same amplitude but travels in the opposite direction. Image current on the metallic wall cancels the magnetic field of the beam outside of the vacuum chamber. In order to measure the beam current with a BCT, the BCT either should be placed inside the vacuum chamber or the conducting chamber should be broken to avoid the image current pass through the torus. As the former requires an installation in the vacuum, it is more appropriate to break the vacuum chamber and install a ceramic insulator between the two metallic ends. This allows the image current to be guided around the magnetic torus using a metallic cover as shown in Figure 5.4.

Figure 5.5 shows a drawing and a picture of the Linac4 beam current transformer.

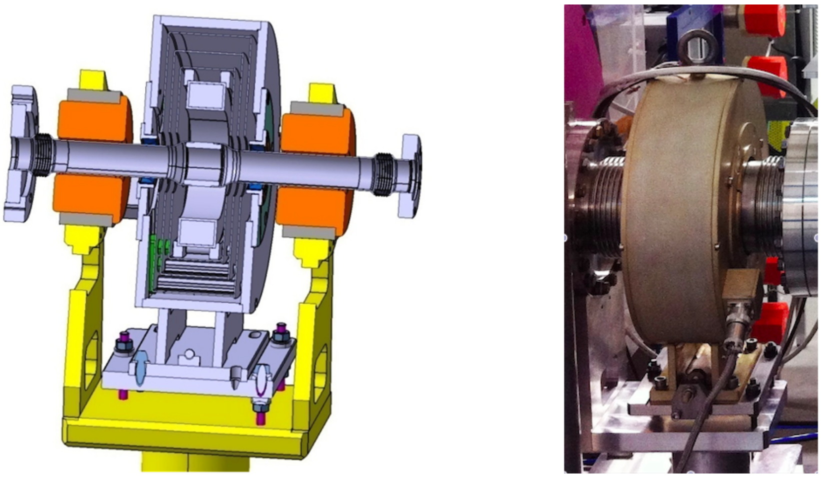

(a) (b)

Figure 5.5. A drawing and a picture of the Linac4 BCT.

Figure 5.6 shows the graphical user interface (GUI) for the beam current measurements at Linac4. The horizontal axis shows the time in nanoseconds and the vertical axis shows the beam current in milliamperes. As it can be seen from the figure, evolution of the beam current along the beam pulse can be observed. Users can choose a window (white window on Figure 5.6) to display the average beam current within the window.

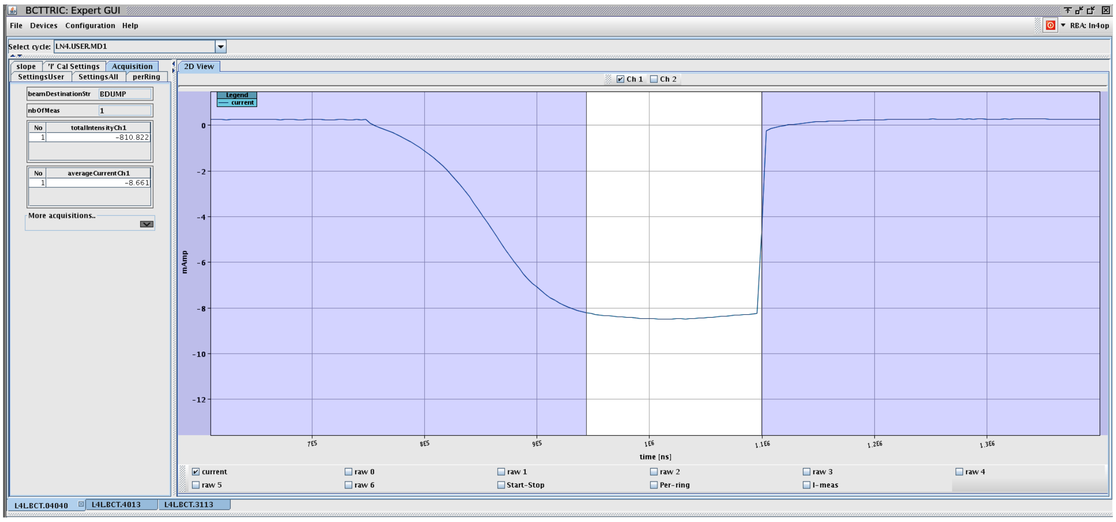

Select cycle: LN4.USER.MD1

beamDestinationStr: BDUMP

nbOfMeas: 1

No	totalIntensityCh1
1	-810.822

No	averageCurrentCh1
1	-8.661

Figure 5.6. Graphical user interface for the Linac4 beam current transformers.

5.2. Measurement of Beam Position

The absolute beam position as well as beam intensity can be measured with a beam position monitor (BPM). As it can be seen in Figure 5.7, four pick-up plates are installed symmetrically around the axis of the vacuum chamber. When a bunch of charged particles passes through the BPM, charges are induced on the plates and create a signal.

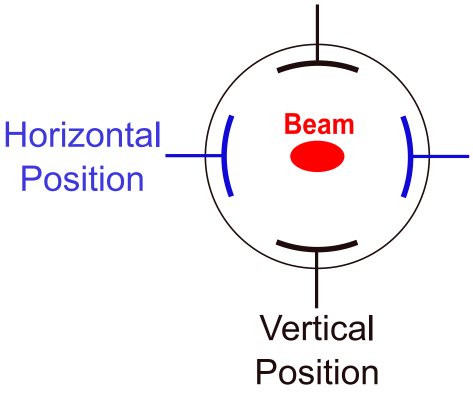

Figure 5.7. A sketch of cross section of a BPM.

The beam position in a transverse plane is then calculated by computing the difference of the magnitude of the signals from two opposite electrodes and normalizing with their sum. The beam intensity is proportional to the sum of magnitude of the signals from all electrodes [43]. A pair of BPMs can also be used for the measurement of the average kinetic energy (See Section 5.7.1).

5.3. Measurement of Transverse Beam Profile

The transverse profile of the beam varies along the accelerator. This variation is controlled using focusing elements (solenoids or quadrupole magnets at Linac4). The transverse beam profile gives information about the machine setting and beam properties. The typical applications of such a measurement are:

- Comparison of the measured and expected beam profile gives an indication of how well the beam is controlled along the accelerator.

- Profile measurements can be used for checking the setting of the magnetic elements and calibrating them.
- A bending magnet and a profile measurement instrument can be used for the measurement of the energy spread (see Section 5.8).
- A slit and a profile measurement instrument can be used for the direct measurement of the transverse emittance (see Section 5.4.1).
- Measured beam profiles can be used for indirect measurement of the transverse beam emittance with quadrupole variation or three monitor method (see Section 5.4.2 and Section 5.4.3).

At Linac4, the transverse beam profiles are measured using two types of instruments, namely, wire scanner (WS) and secondary electron emission (SEM) grid.

5.3.1. Secondary Electron Emission Grid

When a primary beam of particles with sufficient kinetic energy hits a surface, electrons are emitted from the surface. This phenomenon is called secondary electron emission. A SEM grid is composed of parallel wires mounted on a frame (see Figure 5.8). When the particles enter and leave the wires, secondary electrons are emitted. The emission of the electrons creates current on the wires. The current on an individual wire is proportional to the number of particles hitting it. In order to measure the beam profile, the current on each wire should be measured individually which requires one electronic channel for each wire. The beam profile can be obtained by plotting the wire position and the current on the wires. Passage of only one beam pulse is enough for such a measurement.

Figure 5.8 shows a SEM grid with both horizontal and vertical wires. The vertical wires are used for the measurement of the horizontal beam profile. Likewise, the horizontal wires are used for the measurement of the vertical beam profile. The resolution of the measurement depends strongly on the wire spacing.

The Linac4 LEBT has permanent SEM grids (one for each transverse plane) to

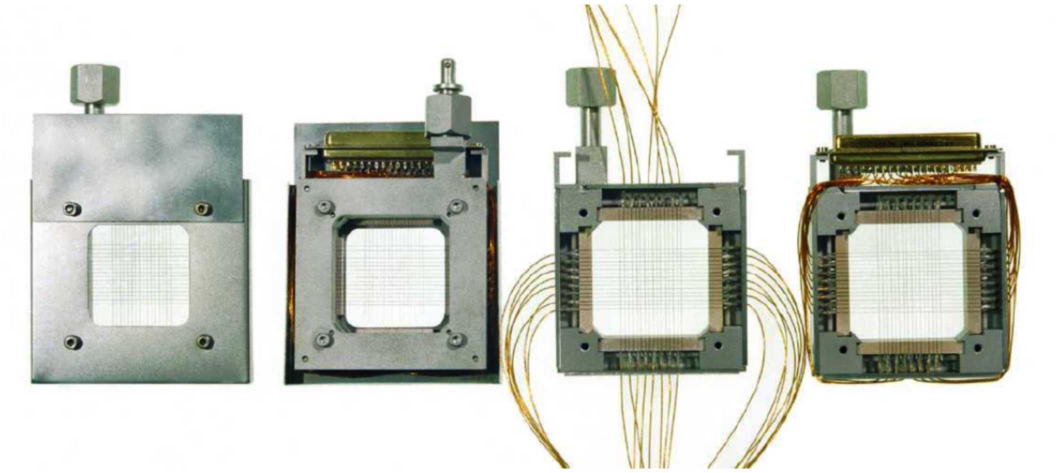

Figure 5.8. SEM grid [40].

monitor the beam profiles during the operation. Each grid is composed of 24 gold-plated tungsten wires with 40 μm diameter. The pitch of the wires is 1 mm in the middle of the grids and increases to 3 mm and then 5 mm towards the edge. During the 45 keV, 3 MeV and 12 MeV commissioning stages, SEM grids were also used for the emittance, energy and energy spread measurements. This will be discussed in the following sections.

5.3.2. Wire Scanner

Instead of using multiple wires for the profile measurements, a single wire can be moved through the beam, and the signal from the wire can be recorded for different positions of the wire. Such a profile measurement device is called a wire scanner. The beam profile can be visualized by plotting the wire position and the signal from the wire. Unlike SEM grids, wire scanners require passage of multiple beam pulses to measure the profile. However, wire scanners do not require expensive electronics and the resolution of the measurement does not depend on the wire spacing as in the case of the SEM grid.

Usually, wire scanners have two wires assembled on a fork, making a 45° angle with the fork and 90° angle with each other (see Figure 5.9). The wires can be cross shaped as in Figure 5.9a or L-shaped as in Figure 5.9b.

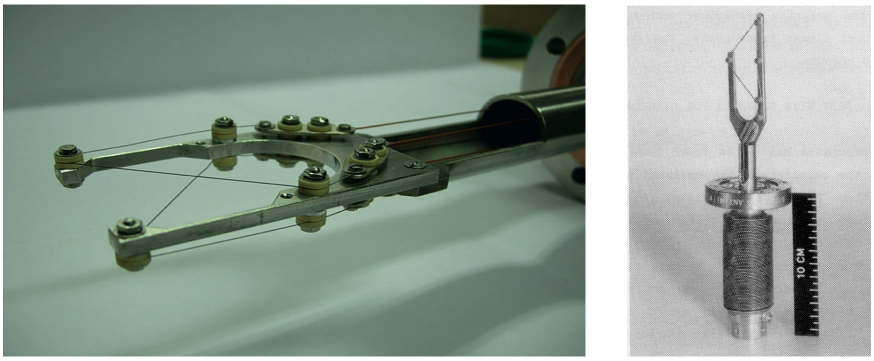

(a) (b)

Figure 5.9. Wire scanners [39, 40].

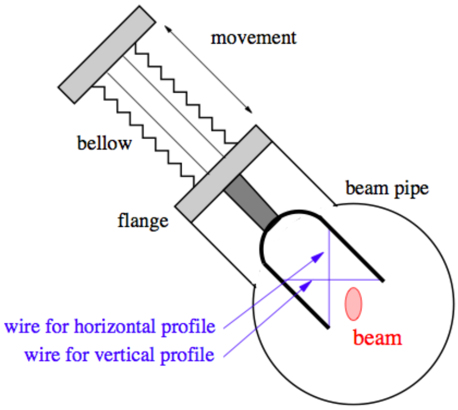

Figure 5.10. Movement of the wire scanner [40].

The arm of the wire scanner moves into or out of the beam pipe making a 45° angle with the vertical plane. As it can be seen in Figure 5.10, the vertical wire measures the horizontal beam profile and the horizontal wire measures the vertical beam profile.

There are two wire scanners in the Linac4 MEBT line (see Figure 7.8). The wire scanners used at the 3MeV test stand [44] had 33 μm thick carbon wires [45] mounted on the same fork with a cross shape as shown in Figure 5.9a. Before the installation of the MEBT at the Linac4 tunnel, the cross shaped wire scanners were replaced with L-shaped ones (as in Figure 5.9b) which have 33 μm thick graphite wires [46]. For the measurements, the wires are moved across the vacuum chamber and the signal from each wire is sampled at a frequency of 250 kHz [45] which makes it possible to measure the evolution of beam profile along the pulse with a resolution of 4 μs.

5.4. Measurement of Transverse Emittance

The transverse emittance of the beam can be measured directly or indirectly. The direct measurement of the emittance is based on sampling the transverse phase spaces of the beam with an emittance measurement device, for instance, slit-grid emittance meter. Such a device can measure the distribution of the particles in the transverse phase spaces and is very useful for generating a multi-particle beam for beam dynamics simulations.

Indirect methods (quadrupole variation and three profile) are based on calculating the emittance from several beam profile measurements. These methods are applicable when the space charge forces can be ignored. If the space charge forces are significant, the forward method can be used to estimate the emittance. The forward method is based on changing the initial beam parameters and tracking a multiparticle beam forward to the location of the profile measurement until a good agreement is found between the simulation and measurements. This will be the only method to determine transverse emittance at 50, 100 and 160MeV commissioning stages of Linac4.

5.4.1. Slit-Grid Emittance Meter

The slit-grid emittance meter is composed of a slit to sample the beam in position and a SEM grid to measure the density of particles for different angles in a phase space. Measurement of the emittance with a slit-grid system is based on moving the slit across the vacuum chamber and recording the signal from the wires of the SEM grid for each position of the slit. The position of the slit opening gives the position of the particles in a phase space. The angle is calculated using the position of the slit opening and the position of the wires. The signals induced on the wire give the density of the particles. In this system, the SEM grid can also be movable to decrease the cost of electronics and increase the resolution of the measurement. A slit-grid pair can measure only one transverse phase space of the beam. Therefore, the slit-grid emittance meter has two slit-grid pairs. The vertical slit and the vertical grid are used for horizontal plane measurements. Likewise, the horizontal slit and the horizontal grid are used for vertical plane measurements.

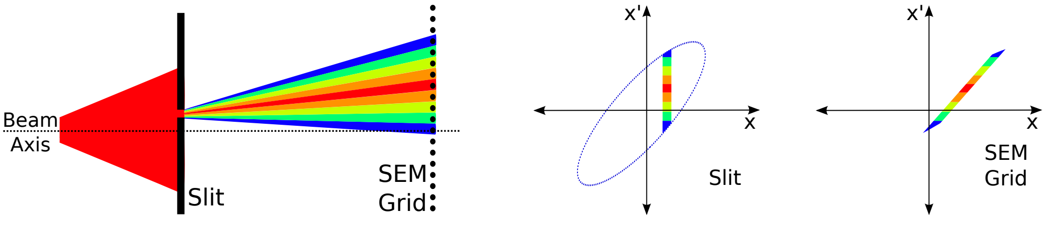

(a) (b)

Figure 5.11. The motion of the selected particles from the slit to the grid, (a) in real space, (b) in a phase space.

In the measurement process, the slit is used for selecting the particles within a narrow slice in position (Figure 5.11). Figure 5.11a shows the motion of the selected particles in the real space. Figure 5.11b shows the phase space of the selected particles just after the slit and at the grid. When the beamlet travels from the slit to the grid, the angular distribution of the particles is transformed into a position distribution and sampled using a SEM grid. The whole phase space of the beam can be sampled by moving the slit across the vacuum chamber.

During a measurement, position of the slit opening, position of the grid and the signal induced on each wire are recorded. As the distance between the wires is well known, the position of each wire can be calculated from the grid position. For the i^{th} step of the slit motion, let's denote the position of the slit opening with x_i^s, the position of the j^{th} wire with x_{ij}^w (Figure 5.12a) and the signal on the wire with S_{ij}.

$$x'_{ij} = \frac{x_{ij}^w - x_i^s}{L} \tag{5.1}$$

When there are no magnetic elements between the slit and the grid, the angle of the particles which hit the j^{th} wire can be calculated using Equation 5.1, where L is the distance between the slit and the grid. In a transverse phase space, S_{ij} gives the density of the particles around the point (x_i^s, x'_{ij}). Figure 5.12a shows the measurement process for the i^{th} position of the slit and Figure 5.12b shows a slice of the phase space that is reconstructed from the measurement data. It is important to note that, the reconstructed phase space from the slit-grid emittance meter gives the description of the beam at the slit location.

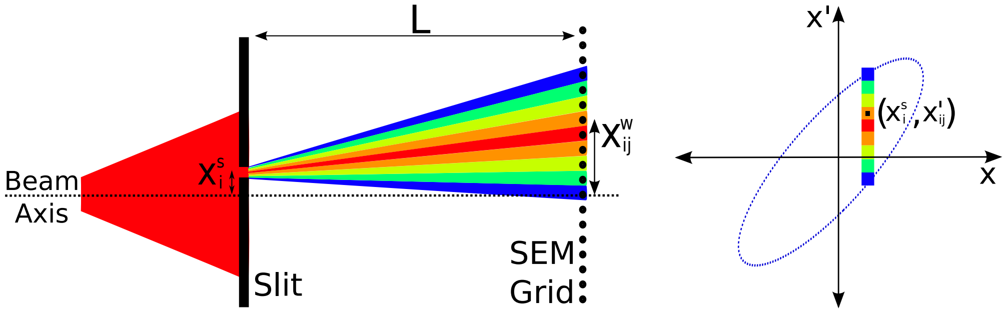

(a) (b)

Figure 5.12. Reconstructing the phase space from the measurement data.

The angular acceptance of such a system is limited by the size of the vacuum chamber and the distance between the slit and the grid. The maximum divergence of a beam which can be measured using such a system is $x'_{max} = r/L$ where r is the radius of the vacuum chamber and L is the distance between the slit and the grid. In order to increase the acceptance of the emittance meter, quadrupole magnets can be installed between the slit and the grid.

The slit-grid emittance meter used at Linac4 for the 3MeV and 12MeV beam commissioning has two quadrupole magnets installed between the slit and the grid (see Figure 7.1). In this case the angle of the particles hitting a specific wire can be calculated using the transfer matrix between the slit and the grid.

The position and the angle of the particles at two different locations on a beam line can be related to each other by the transfer matrix between these two locations. In a transverse phase space, the relationship between a particle's position and angle at the grid and at the slit locations is given by Equation 5.2. In the equation, x is the position of a particle, x' is its angle and subindices s and g indicate the slit and the grid locations, respectively.

$$\begin{bmatrix} x \\ x' \end{bmatrix}_g = \begin{bmatrix} R_{11} & R_{12} \\ R_{21} & R_{22} \end{bmatrix} \begin{bmatrix} x \\ x' \end{bmatrix}_s \tag{5.2}$$

Two equations are obtained from the matrix multiplication. The first equation, Equation 5.3, relates the angle of the particles at the slit location (x'_s), to position of the particle at the slit (x_s) and at the grid (x_g) location.

$$x'_s = \frac{x_g - R_{11}x_s}{R_{12}} \tag{5.3}$$

Likewise, for the i^{th} position of the slit, the angle of the particles which hit the j^{th} wire can be calculated using Equation 5.4.

$$x'_{ij} = \frac{x^w_{ij} - R_{11}x^s_i}{R_{12}} \tag{5.4}$$

Notice that Equation 5.1 can be obtained from Equation 5.4 by inserting the corresponding elements of the transfer matrix of a drift, $R_{11} = 1$ and $R_{12} = L$.

5.4.1.1. Linac4 Slit-Grid Emittance Meter. During the Linac4 commissioning slit-grid emittance meters were used for the direct sampling of the transverse phase spaces at 45 keV, 3 MeV and 12 MeV beam energies. Because of the different beam divergence and heat deposition on the slit, the design of the emittance meter used for the measurements at 45 keV is different than the one used at 3MeV and 12MeV.

The emittance meter used at 45keV has a 1mm thick steel slit blade which is inclined at 45° relative to vertical plane. The blade has two 100 μm wide gaps machined, one parallel to the horizontal axis, the other parallel to the vertical axis. Therefore, similar to the L-shaped wire scanner in Figure 5.9b, depending on the depth of the blade in the vacuum chamber, it acts either as a vertical or a horizontal slit. The two SEM grids are positioned 20cm downstream the slit. Each SEM grid consists of 40 tungsten wires, with 40 μm diameter, separated by 0.75 mm [47]. Each wire is connected to a separate acquisition channel and sampled at 160kHz frequency which makes it possible to measure the emittance evolution along the pulse with a resolution of 6.25μs. A Faraday Cup is placed 8 cm downstream the SEM grids for the beam current measurements and to act as a beam dump.

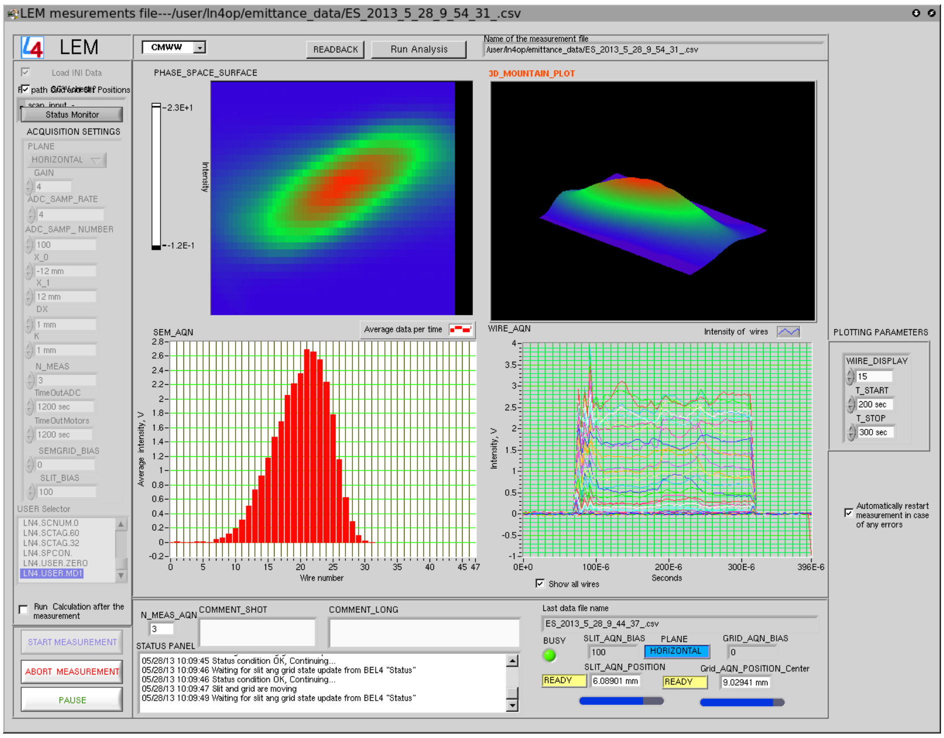

LEM mesurements file---/user/ln4op/emittance_data/ES_2013_5_28_9_54_31_.csv

Name of the measurement file: /user/ln4op/emittance_data/ES_2013_5_28_9_54_31_.csv

ACQUISITION SETTINGS
PLANE: HORIZONTAL
GAIN: 4
ADC_SAMP_RATE: 4
ADC_SAMP_ NUMBER: 100
X_0: -12 mm
X_1: 12 mm
DX: 1 mm
K: 1 mm
N_MEAS: 3
TimeOutADC: 1200 sec
TimeOutMotors: 1200 sec
SEMGRID_BIAS: 0
SLIT_BIAS: 100

USER Selector
LN4.SCNUM.0
LN4.SCTAG.60
LN4.SCTAG.32
LN4.SPCON.
LN4.USER.ZERO
LN4.USER.MD1

☐ Run Calculation after the measurement

PLOTTING PARAMETERS
WIRE_DISPLAY: 15
T_START: 200 sec
T_STOP: 300 sec

☑ Automatically restart measurement in case of any errors

N_MEAS_AQN: 3
COMMENT_SHOT:
COMMENT_LONG:

STATUS PANEL

```
05/28/13 10:09:45 Status condition OK, Continuing...
05/28/13 10:09:46 Waiting for slit ang grid state update from BEL4 "Status"
05/28/13 10:09:46 Status condition OK, Continuing...
05/28/13 10:09:47 Slit and grid are moving
05/28/13 10:09:49 Waiting for slit ang grid state update from BEL4 "Status"
```

Last data file name: ES_2013_5_28_9_44_37_.csv
BUSY: ●
SLIT_AQN_BIAS: 100
PLANE: HORIZONTAL
GRID_AQN_BIAS: 0
SLIT_AQN_POSITION: READY 6.08901 mm
Grid_AQN_POSITION_Center: READY 9.02941 mm

Figure 5.13. Graphical user interface of the slit-grid emittance meter application [44].

The emittance meter used at 3 MeV and 12 MeV has two identical slits for each transverse plane. The slit is made of two graphite blades mounted with a 15° angle with respect to the horizontal axis in order to distribute the energy deposition on a larger surface. The SEM grids are located 3m downstream the slit. Each grid consists of 48 graphite wires with a diameter of 33 μm. Distance between the wires is 0.75 mm [46]. Signal from each wire is sampled at 200 kHz frequency which makes it possible to measure the emittance evolution along the pulse with a resolution of 4 μs [44].

Figure 5.13 shows the graphical user interface of the Linac4 emittance meter application. The same interface and application have been used for all stages of commissioning up to 12 MeV with few minor modifications. The emittance meter application is based on LabView. The user defines the transverse plane to be measured, initial and final positions of the slit and the relative movement between the slit and the grid. When the measurement is started, the application moves the slit and the grid automatically and acquires the signals from the wires. It stores the data and plots several graphs for their visualization.

In Figure 5.13, the upper left graph shows the measured phase space in a two dimensional colored map, the colors indicate the signal strength acquired during the measurement. The upper right graph shows the same phase space in a three dimensional mountain plot. It can be rotated using the mouse. The lower left graph shows the wire number in horizontal axis and the signal acquired from each wire in the vertical axis for the current position of the slit. The lower right graph shows the signal acquired from each wire along the pulse. Each color represents a different wire of the SEM grid. During an emittance scan, all the graphs are updated as the slit moves to the next position.

5.4.1.2. Generating a Multi-particle Beam Using Measurement Data.

Emittance measurement devices which directly sample the transverse phase spaces are essential for the commissioning of the low energy part of the linac. Using the data obtained from the horizontal and vertical emittance scans taken at the same location, one can generate a multi-particle beam and use it as an input for the beam dynamics simulations. Using a particle distribution obtained from the measurements allows the optimization of the linac parameters more accurately with the tracking codes.

Figure 5.14 shows the graphical user interface (GUI) of the program that is used for generating a multi-particle beam from the slit-grid emittance measurement data during the Linac4 commissioning. The user chooses the horizontal and vertical measurement files, consecutively, as input. The program displays the data visually on three graphs for each transverse plane. The left side of the GUI displays the graphs of the horizontal plane and the right side displays the graphs of the vertical plane.

Before handling the measurement data, the user should enter the parameters to be

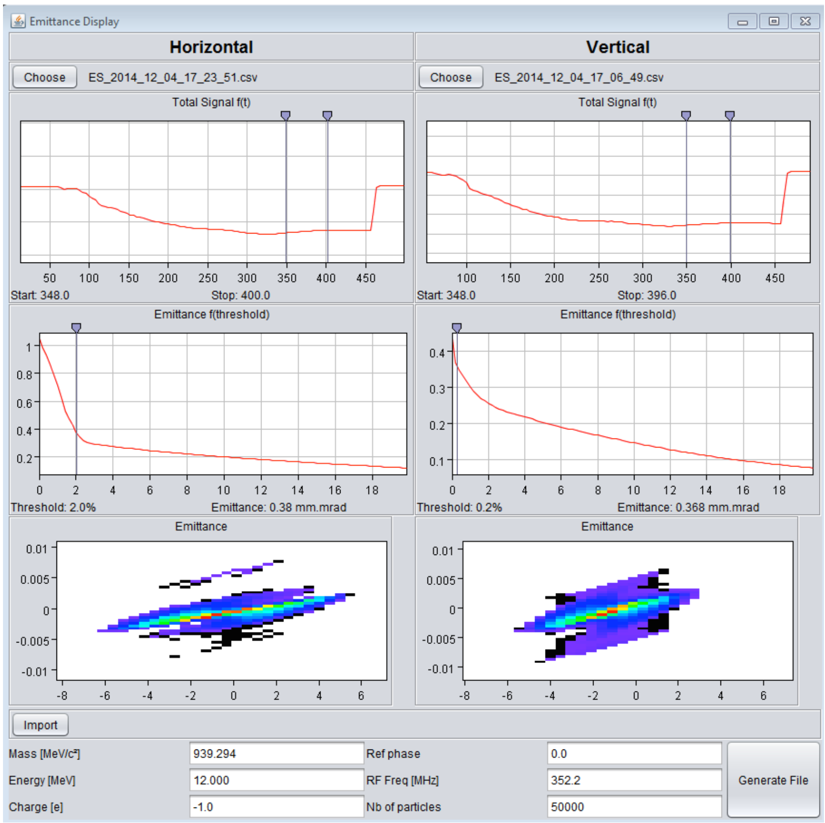

Horizontal: ES_2014_12_04_17_23_51.csv

Start: 348.0 Stop: 400.0

Threshold: 2.0% Emittance: 0.38 mm.mrad

Vertical: ES_2014_12_04_17_06_49.csv

Start: 348.0 Stop: 396.0

Threshold: 0.2% Emittance: 0.368 mm.mrad

Mass [MeV/c²] 939.294

Energy [MeV] 12.000

Charge [e] -1.0

Ref phase 0.0

RF Freq [MHz] 352.2

Nb of particles 50000

Figure 5.14. Graphical user interface of Emittance Display program.

used for the beam generation. The parameter window is located below the graphs (See Figure 5.14). The mass and the average kinetic energy of the particles are necessary for the calculation of the emittance.

The top graph shows the total signal on all the wires for all positions of the slit along the beam pulse. Horizontal axis shows the time in μs and vertical axis shows the total signal in arbitrary units. Referring to Section 5.4.1, the total signal can be calculated by $S_T(t) = \sum_{i,j} S_{ij}(t)$. The beam intensity is proportional to $S_T(t)$, therefore, for a stable beam the horizontal and the vertical emittance scans should have similar graphs as in Figure 5.14. Looking at the graph of total signal along the pulse, the user can identify the stable part of the beam pulse. Using the cursors just above the graph window, the user can select the initial time and the final time between which the signals will be considered for the particle generation. This feature allows the user to study the evolution of the measured phase spaces along the beam pulse.

After selecting the initial and the final time, the program calculates the time average of the signals, S_{ij}, within the selected time interval and updates the next two plots automatically.

The second graph (in the middle) allows the user to select an appropriate threshold value to handle the noise in the measurements. The program calculates and plots the normalized rms emittance, ϵ_{rms}, of the beam in the corresponding phase space for different threshold values. The threshold is defined relative to the maximum of S_{ij} after averaging in time. The program subtracts the threshold from S_{ij} or sets the signal to zero if it is smaller than the threshold. The curve of ϵ_{rms} vs. threshold can be different for the horizontal and the vertical measurements. If there is significant noise in the measurement, the curve has a sharp drop at the low end side of the plot as seen for the horizontal plane in Figure 5.14. However, if the noise level is low, ϵ_{rms} decreases slightly with increasing threshold as seen for the vertical plane in the figure. The user can define the threshold value independently for each plane by moving the cursor above the graph window. After selecting the threshold value, the third graph is updated automatically.

The last graph shows the two dimensional colored map of the measured and processed signals. It represents the distribution of the particle density in the corresponding phase space. The graph is obtained by plotting (x_i^s, x'_{ij}, S_{ij}). This graph is for the visualization of the result, therefore, it is not interactive.

After setting the time interval and the threshold for each transverse plane, the user can generate particles in the four dimensional phase space. The number of particles to be generated is defined in the parameter window. At this step, the program generates the coordinates of the particles in horizontal and vertical phase spaces independently[6] . In order to generate a multi-particle beam in six dimensional phase space, the particle distribution in the longitudinal phase space should be defined. Using the import button, the user can import a file which contains the longitudinal particle distribution. In that case, the number of particles to be generated is limited to the number of particles

---

[6] Slit-grid emittance meters do not give any correlation between the two transverse phase spaces.

defined in the imported file.

If the file with the longitudinal particle distribution is imported, after generating the beam, the program writes an output beam file which is ready to be imported by PATH and used as an input for beam dynamics simulations.

5.4.2. Quadrupole Variation Method

The quadrupole variation method is based on calculating the Twiss parameters of the beam, in a transverse phase space, using three or more profile measurements. The method is based on changing the gradient of a focusing quadrupole magnet located upstream of a profile monitor and measuring the beam size for different quadrupole gradients. The beam Twiss parameters can be calculated at a location upstream of the quadrupole magnet where the beam properties do not depend on the quadrupole magnet setting, for example at the beginning of the quadrupole magnet, point A, in Figure 5.15. This method assumes that the space charge effects are negligible.

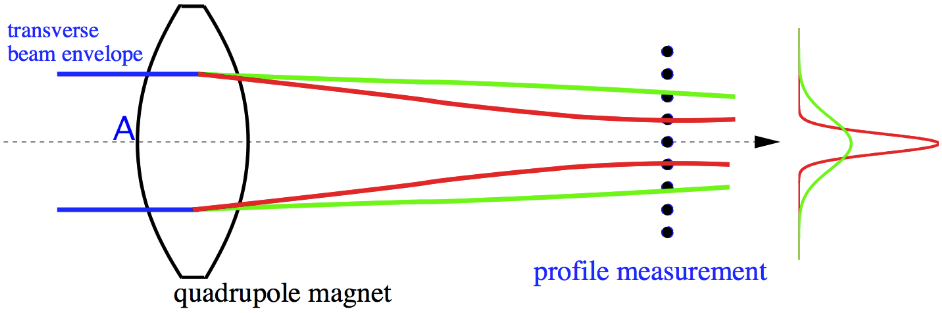

Figure 5.15. Measurement of emittance with quadrupole variation method [40].

Because of the noise in the measurements and the tails of the distribution, the full beam size is not straightforward to determine. Instead, the rms beam size is less sensitive to measurement errors, therefore, more reliable for the emittance calculations. Using rms beam size for the calculations, one can find the rms emittance of the beam.

The evolution of the beam matrix between two locations, along the beam line, can be calculated with Equation 5.5, where $\boldsymbol{\sigma}(i)$ and $\boldsymbol{\sigma}(f)$ are the beam matrices at the initial and final locations, respectively, and $\boldsymbol{R}$ is the transfer matrix between the two locations.

$$\boldsymbol{\sigma}(f) = \mathbf{R}\boldsymbol{\sigma}(i)\mathbf{R}^T \tag{5.5}$$

The first element of the beam matrix σ_{11} is simply the square of the rms beam size, x_{rms}^2, which is measured. Carrying out the matrix multiplication in Equation 5.5 gives the relation in Equation 5.6.

$$x_{rms}^2 = \sigma_{11}(f) = R_{11}^2\sigma_{11}(i) + 2R_{11}R_{12}\sigma_{12}(i) + R_{12}^2\sigma_{22}(i) \tag{5.6}$$

The beam matrix is symmetric. Therefore, the elements of the beam matrix on the right-hand side of Equation 5.6, completely describes the beam matrix at an initial location. In order to construct $\boldsymbol{\sigma}(i)$, all three terms, $\sigma_{11}(i), \sigma_{12}(i), \sigma_{22}(i)$, must be calculated which requires solving three independent equations in the form of Equation 5.6. Changing the quadrupole gradient which changes the transfer matrix and measuring the beam size downstream, one can obtain three independent equations.

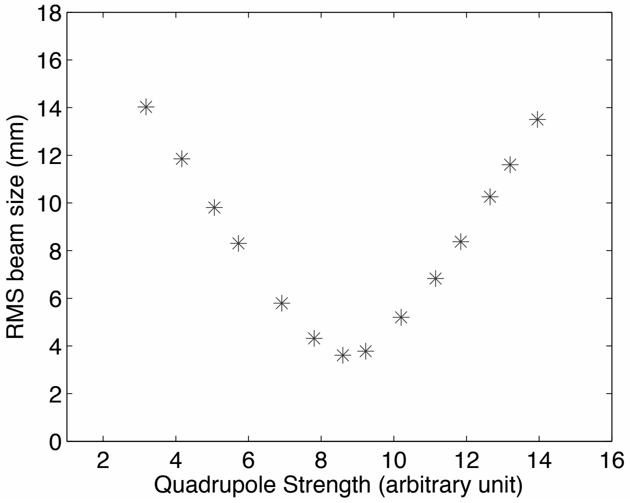

Figure 5.16. Example of measured rms beam size as a function of quadrupole magnet strength.

The accuracy of the result depends on the choice of the quadrupole magnet setting which defines the measured beam size. This method works better when one obtains a beam waist during the measurements as shown in Figure 5.16. One of the measurement points around the beam waist and two other points from each side of the parabola can be used for the calculation of $\boldsymbol{\sigma}(i)$.

During the profile measurements, because the quadrupole gradient is varied in a wide range, there may be particle losses which may damage the vacuum chamber, especially at higher beam energies. At high energy, three profile method can be used for emittance measurements.

5.4.3. Three Profile Method

The three profile method is very similar to the quadrupole variation method. It is also based on solving a system of at least three independent equations to calculate the Twiss parameters of the beam. Instead of varying the quadrupole gradient and measuring the beam profile with one profile monitor, the quadrupole gradient is fixed and the profile is measured at three monitors downstream of the quadrupole as shown in Figure 5.17.

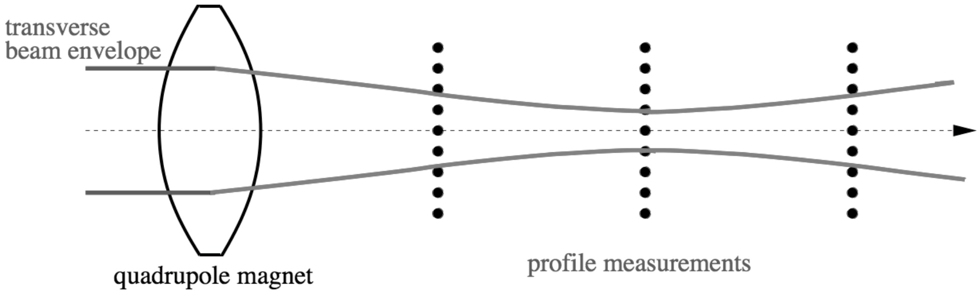

Figure 5.17. Measurement of emittance with three profile method [40].

In principle, any location upstream of the first profile monitor can be chosen to calculate the Twiss parameters and reconstruct a transverse phase space of the beam. Three equations are obtained using the transfer matrices from the reconstruction point to each profile monitor and the measured beam size. For an accurate calculation of Twiss parameters, it is favorable to obtain the beam waist at the second profile monitor as shown in Figure 5.17.

5.4.4. Forward Method

Both quadrupole variation and three profile method are based on calculations which ignore the space charge effects. These methods do not give accurate results for low energy, high current hadron beams, where the space charge forces can be dramatic. When space charge forces are not negligible, the forward method can be used for the emittance reconstruction.

The forward method is also based on profile measurements. The measurements can be performed by varying a quadrupole, similar to the case of quadrupole variation method, or by fixing a quadrupole and measuring at three locations, similar to the case of three profile method. However, unlike the other methods, the forward method is based on tracking a particle beam from an initial location to the measurement location. The principle is to start with an initial beam and vary its parameters at a location where the transverse phase spaces are being reconstructed and track the multi-particle beam forward to the profile monitor and compare the beam size from the simulations and the measurements.

At least six measurements (three measurements for each transverse plane) should be simulated with an identical input beam and the results should be analyzed simultaneously. For the analysis of the data, a penalty function can be defined as in Equation 5.7 where N is the number of measurements to be used at the reconstruction process, r^m and r^s are the rms beam size (x_{rms} or y_{rms}) from measurement and simulation respectively.

$$f_p = \sqrt{\sum_{i=1}^{N} \left(\frac{r_i^m - r_i^s}{r_i^m} \right)^2} \tag{5.7}$$

In order to find an input beam which describes the measurement data, a series of runs are launched (for each measurement) by varying the Twiss parameters of the input beam in both transverse planes [48]. At the end of each run, the value of the penalty function is calculated. The parameters of the input beam is varied with a matching algorithm until the penalty function is lower than a user defined value.

The forward method takes space charge forces into account. Therefore, the result for the transverse phase spaces depends on the longitudinal parameters of the beam. This effect is stronger for high current beams at low energies. For accurate determination of the transverse properties, it is important to specify the longitudinal parameters of the initial beam as realistically as possible.

Choosing an initial beam whose properties are close to the one which is measured would fasten the process. As a first approximation, the Twiss parameters of the initial beam can be calculated from the quadrupole variation or three profile method. After calculating the Twiss parameters, a multi-particle beam can be generated to be used as an input beam for the simulations. At this stage, the distribution of the particles in the transverse phase spaces should be predicted.

If the emittance of the beam is measured at an upstream location using a direct method, like the slit-grid emittance meter, the Twiss parameters and the particle distribution at the reconstruction point can be approximated using multi-particle tracking codes. During the 3 MeV commissioning stage of Linac4, the forward method was used for the reconstruction of transverse phase spaces at the RFQ exit (See Section 7.2.2). For the reconstruction, the longitudinal particle distribution of the beam tracked through the RFQ was used.

5.5. Measurement of Longitudinal Bunch Profile

The longitudinal bunch structure can be measured using a bunch shape monitor(BSM). The operational principle of BSM is shown in Figure 5.18a. The principle is based on the coherent transformation of the longitudinal bunch structure into a spatial distribution of low energy secondary electrons through transverse RF modulation [49].

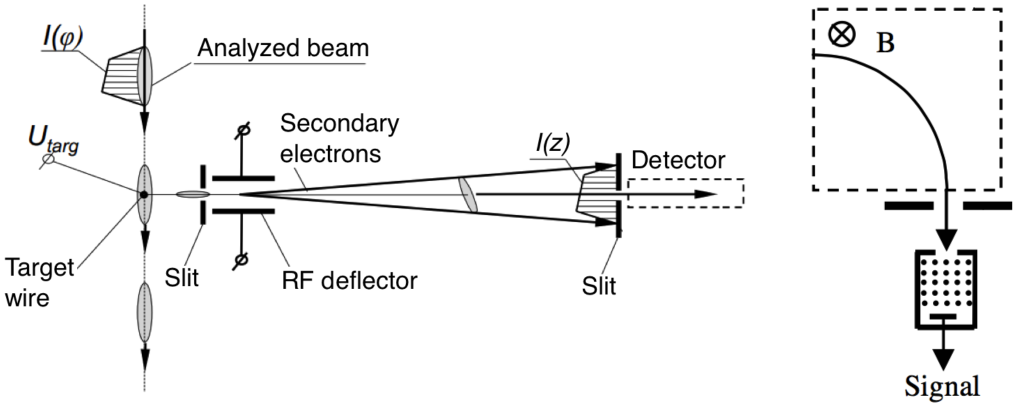

(a) (b)

Figure 5.18. (a) The operational principle of BSM, (b) detector part of the BSM [49].

As seen in Figure 5.18a, a wire is inserted into the vacuum chamber as a target. When the particles in the main beam hit the wire, secondary electrons are generated. A slice of the secondary electron beam is selected using a slit between the target and the RF deflector. At a specific time, the density of the generated electrons is proportional to the number of particles hitting the wire. Therefore, the longitudinal distribution of the secondary electrons passing through the slit is similar to the longitudinal distribution of the particles in the measured beam. The RF deflector, which operates at the bunch frequency, deflects the particles and transforms the longitudinal distribution, $I(\phi)$, into a spatial distribution, $I(z)$, as shown in Figure 5.18a. The spatial distribution is measured using a slit and a detector after it. The RF phase of the deflector is varied in steps to select different part of the distribution with the second slit. Typically, the resolution of the BSM is about 1° at frequencies of hundreds of MHz [49].

When measuring the bunch structure of an H^- beam, electrons from H^- ions are stripped and distort the measurement. In order to separate the stripped electrons from the secondary electrons, the target wire is negatively polarized and a bending magnet is installed in the detector part. The field of the bending magnet is adjusted to select the secondary electrons as shown in Figure 5.18b.

5.6. Measurement of Longitudinal Emittance

The quadrupole variation method can be adapted to the longitudinal phase space to calculate the emittance of the beam. The phase of the RF cavity can be set to -90° to have only bunching without any acceleration. Then, the RF amplitude of the cavity can be varied to measure the longitudinal rms phase spread as a function of the cavity setting. In Linac4, a BSM was used for the measurement of the longitudinal phase spread.

The Twiss parameters can be calculated using a system of linear equations constructed from the transfer matrices in the longitudinal plane and the measured rms beam size, as explained in Section 5.4.2. If the space charge forces are not negligible, then the forward method (Section 5.4.4) can be applied to the longitudinal phase space. During the 3 MeV commissioning period, the longitudinal emittance was reconstructed at the RFQ exit using forward method (see Section 7.3.3).

5.7. Measurement of Average Energy

The average energy of the beam after an accelerating structure depends on the setting of the field amplitude and the RF phase. Therefore, during the commissioning period, energy measurements are very useful for characterization of the linac structure. Up to 12 MeV commissioning stage, two different methods have been used for the measurement of energy, namely, the Time-of-Flight (ToF) and the magnetic spectrometer method.

5.7.1. Measurement of Average Energy with Time-of-Flight

The set-up for the ToF measurements consists of two BPMs separated by a drift of several meters. The principle is to measure the time it takes for a bunch to travel from the first BPM to the second one, then, calculate the speed and the average kinetic energy of the beam.

The principle of the ToF measurement is shown in Figure 5.19. If one measures a single bunch, the time difference between the signals from two BPMs, ΔT, can be measured without confusion. However, when measuring a bunched beam, there are many bunches inducing signals which are not distinguishable. Therefore, the time difference of the signals from the two BPMs, Δt, is smaller than the RF period, T_{RF}. If the number of bunches between the two BPMs is known, then the time of flight can be calculated.

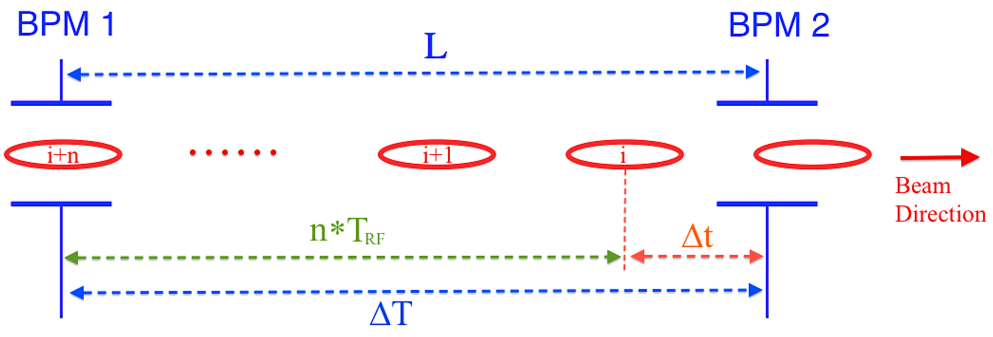

Figure 5.19. Principle of ToF measurement using two BPMs.

In Figure 5.19, the number of full bunches between the two BPMs is n. Δt is the time difference between the signal from the two BPMs. However, the signals are induced by different bunches. The signal from BPM2 is induced by the i^{th} bunch and the signal from BPM1 is induced by the $(i+n)^{th}$ bunch. The time required for the i^{th} bunch to travel from BPM1 to BPM2 can by calculated using Equation 5.8 by considering the number of bunches between the BPMs and the RF period. After the measurement of time-of-flight, knowing the distance between the two BPMs, the calculation of speed and energy is straightforward.

$$\Delta T = nT_{RF} + \Delta t \tag{5.8}$$

During the Linac4 12MeV commissioning stage, ToF measurements were used for the precise calibration of the RF phase and field amplitude of the first DTL tank.

5.7.2. Measurement of Average Energy with Magnetic Spectrometer

When a charged particle enters a uniform magnetic field that is perpendicular to its velocity, it follows a circular trajectory with a certain radius. For a particle with charge q and momentum p, the infinitesimal angle of deflection is given by Equation 5.9 where B is the magnetic field and dz is the infinitesimal displacement along the trajectory of the particle.

$$d\alpha = \frac{q}{p} B dz \tag{5.9}$$

Figure 5.20 shows a particle passing through a dipole magnet. The total angle of deflection, α_{bend}, can be found by integrating Equation 5.9, taking into account the inhomogeneous field, $B_y(z)$, of the magnet along the path.

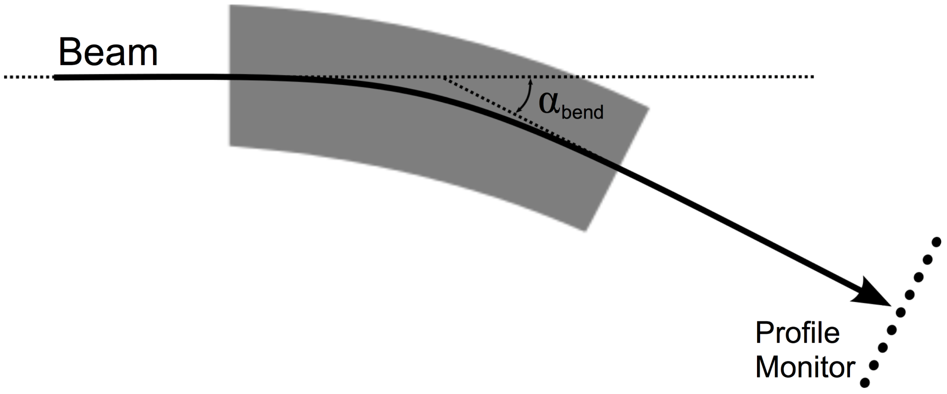

Figure 5.20. Measurement of average energy with a spectrometer.

Integrating Equation 5.9 along the path of the particle and solving for momentum gives the relation in Equation 5.10.

$$p = \frac{q}{\alpha_{bend}} \int\limits_{path} B_y(z) dz \tag{5.10}$$

Equation 5.10 indicates that the momentum of a particle can be determined by measuring the angle of deflection in a known magnetic field. Afterwards, the kinetic energy can be calculated using relativistic relations. As shown in Figure 5.20, a spectrometer system with a dipole magnet and a profile monitor can be used for the measurements. The measurement principle can be applied to a beam of charged particles. The momentum and the average energy can be calculated by analyzing the horizontal beam profile obtained from the monitor.

5.8. Measurement of Energy Spread

Energy spread of a charged particle beam can be measured using a spectrometer shown in Figure 5.20. The angle of deflection of a particle depends on the momentum of the particle. Therefore, when particles pass through the bending magnet the momentum spread of a particle beam effects the particle distribution in the horizontal plane. The momentum spread and the energy spread can be calculated by analyzing the horizontal beam profile obtained from the profile monitor.

For a Gaussian particle distribution, after the bending magnet, the horizontal rms beam size is given by Equation 5.11 [23].

$$x_{rms} = \sqrt{\beta_b \epsilon_{rms} + \left(D \frac{p_{rms}}{p_0} \right)^2} \tag{5.11}$$

The first term under the square root comes from the monochromatic part of the beam. The second term is the contribution of the momentum spread where D is the dispersion, p_{rms} is the rms momentum spread and p_0 is the momentum of the synchronous particle. The contribution of the first term can be decreased significantly so that it can be ignored and the measured particle distribution is directly proportional to the momentum spread. A slit can be introduced before the bending magnet to decrease the emittance of the beam and the beta function can be minimized by obtaining a beam waist around the location of the profile monitor. In this case Equation 5.11 takes the form of Equation 5.12.

$$x_{rms} = D \frac{p_{rms}}{p_0} \tag{5.12}$$

Using the value of the dispersion function at the position of the profile monitor and the measured horizontal spread of the profile, the momentum spread (p_{rms}) can be calculated using Equation 5.11. The momentum spread and the energy spread (W_{rms}) can be related using Equation 2.17[7] by replacing Δp by p_{rms} and ΔW by W_{rms}.

---

[7] Notice that Equation 2.17 is an approximation and the accuracy depends on $\Delta p/p_0$.

6. 45 keV COMMISSIONING STAGE

The parameters of the beam coming from the ion source are adjusted in the LEBT before the beam is injected into the RFQ. Hence, it is crucial to understand the beam parameters for an optimized matching of the beam from the ion source to the RFQ. Measurements performed during the LEBT commissioning aimed to validate the simulation tools and techniques, characterize the beam parameters and generate a multi-particle beam to be used for the beam matching to the RFQ.

The Linac4 measurement campaign started at the Linac4 3 MeV test stand. During 2010 and onwards, extensive measurements were taken after the source, and after the first and the second solenoids (RFQ injection plane) with the aim of preparing for the RFQ commissioning and validating the simulation tools [50, 51, 52, 53]. This thesis focuses on the commissioning period starting at the end of 2012.

During the commissioning of the LEBT, the ion source was operated both in proton and H^- production modes. In December 2012 the measurements at the Linac4 LEBT started with a proton beam and the source was switched to H^- mode in February 2013 [44]. This chapter discusses the LEBT diagnostics and measurement set-up, the measurements performed during the LEBT commissioning and their analysis.

6.1. LEBT Diagnostics and Measurement Set-up

There are several permanent beam diagnostic instruments installed in the LEBT. Figure 6.1 shows the layout of the LEBT with the diagnostic instruments. Between the two solenoid magnets, there is a BCT and a diagnostic tank which houses a SEM grid and a Faraday Cup. During daily operations, the SEM grid can be inserted into the beam pipe and used for checking the stability of the beam coming from the ion source. Together with a BCT downstream of the RFQ, the LEBT BCT and the Faraday Cup are used for the RFQ transmission measurements. The Faraday Cup can also be used as a beam dump to stop the beam going into the RFQ and to monitor the beam current at the same time.

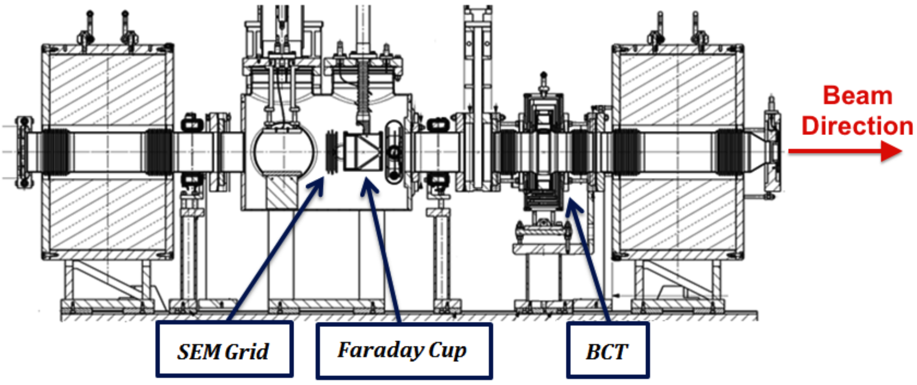

Figure 6.1. Diagnostic instruments on the LEBT line.

During the commissioning of the LEBT, a slit-grid emittance meter was used for the characterization of the beam and the solenoids. Figure 6.2 shows a picture of the measurement set-up during the LEBT commissioning. As it can be seen from the picture, the slit-grid emittance meter was installed after the diagnostic tank.

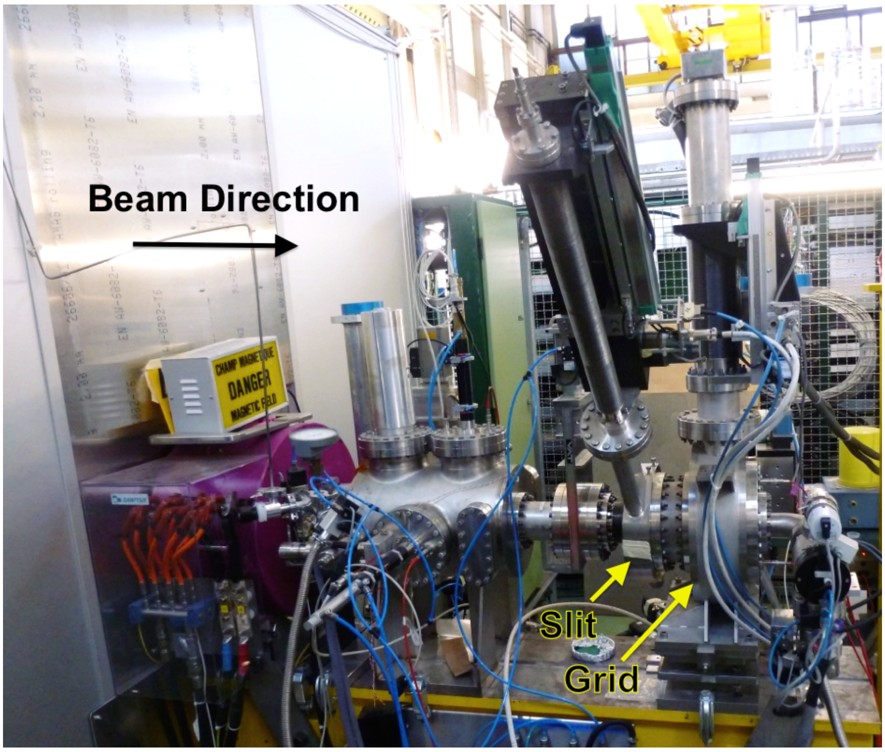

Figure 6.2. Picture of the solenoid, the diagnostic tank and the emittance meter.

6.2. Emittance Measurements and Backtracking

Several emittance measurements were taken after the first solenoid of the LEBT with the measurement set up shown in Figures 6.2 and 6.5. The phase space of the beam in the transverse planes at the slit location was changed by varying the electrical current passing through the solenoid magnet windings (I_{sol}, solenoid current). For each solenoid current, both the horizontal and the vertical phase space plots of the beam were extracted. Then, a multi-particle beam was generated (see Section 5.4.1.2) using the data both from the horizontal and vertical emittance scans. Each generated beam had 45 keV average energy and a very small energy spread (0.1 per mill). The process was repeated both for the proton beam and the H^- beam.

6.2.1. Measurements with the Proton Beam

The LEBT solenoid magnets are identical and can produce an integrated axial field of $9.6 \cdot 10^{-2}$ Tm for $I_{sol} = 145$ A. Figure 6.3 shows the phase space plots of the generated proton beams for three different solenoid currents. As it can be seen from the figure, for each solenoid current, shape and the orientation of the phase space plot of the beam at the slit location is different. The beam is convergent for $I_{sol} = 85$ A (Figures 6.3a and 6.3d), it is focused for $I_{sol} = 95$ A (Figures 6.3b and 6.3e) and it is divergent (focused before the slit) for $I_{sol} = 105$ A (Figures 6.3c and 6.3f).

Figure 6.4 compares the phase space plots of the beams shown in Figure 6.3. While the phase space plots of the proton beam rotate and change shape with increasing solenoid current, the arms at two sides don't change orientation. These arms represent the H^0 particles which also leave signal on the emittance meter SEM grid[8] . For particle tracking, these arms were removed from the beam.

Figure 6.5 shows a sketch of the set-up used for the LEBT emittance measurements. The phase space plots shown in Figure 6.3 describe the beam at the slit location (see Section 5.4.1). Therefore, they can not be used directly for the optimization of the

---

[8] H^0 and the other particle species, H_2^+ and H_3^+, will be discussed later in this section.

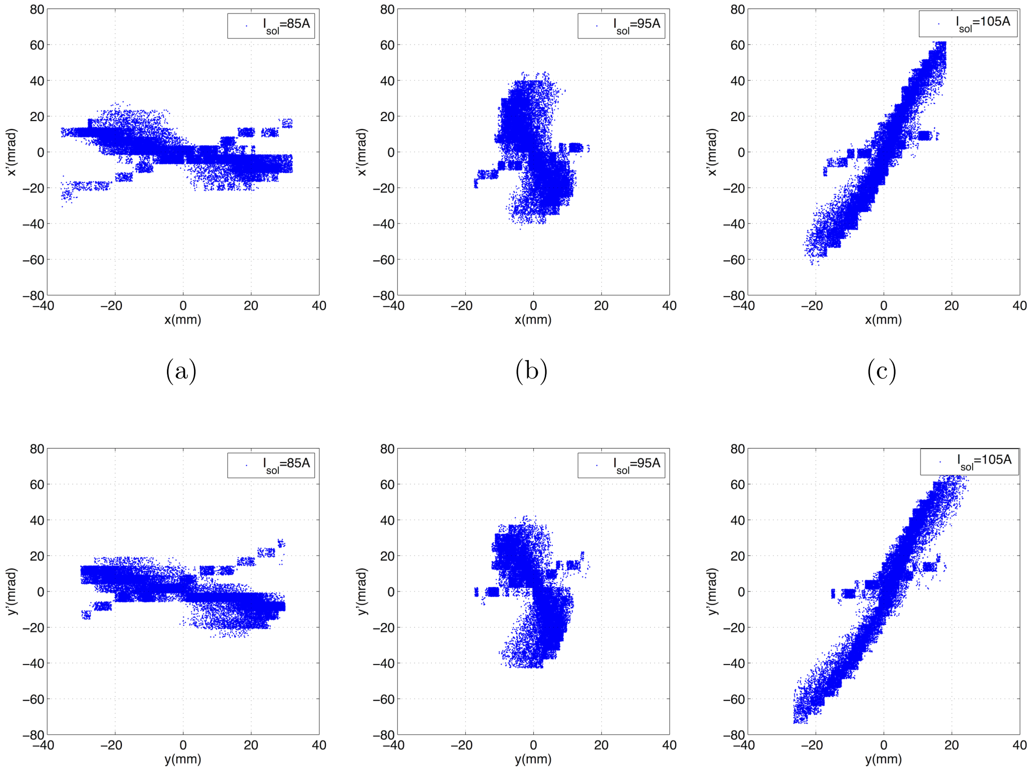

(a) (b) (c)

(d) (e) (f)

Figure 6.3. The phase space plots of the proton beams generated from the emittance measurement data. The first row shows the horizontal and the second row shows the vertical phase space plots. From left to right, $I_{sol} = 85$ A, $I_{sol} = 95$ A and $I_{sol} = 105$ A, respectively.

solenoid magnets to match the beam from the ion source to the RFQ. The matching process requires the definition of the particle beam at the entrance of the first solenoid magnet (see Section 6.3 for the matching process). Therefore, the generated beams had to be backtracked to the beginning of the first solenoid where the magnetic field starts[9] (see Figure 6.5). The backtracking includes tracking the particles first through an 80 cm long drift and then 60 cm long magnetic field map.

The measured beam current at the Faraday cup was around 15 mA. However due to space charge compensation, the effective current of the beam is decreased. This decrease had to be taken into account for the computation of the space charge forces.

---

[9] The physical length of the solenoid itself is 30 cm, however the magnetic field region is 60 cm.

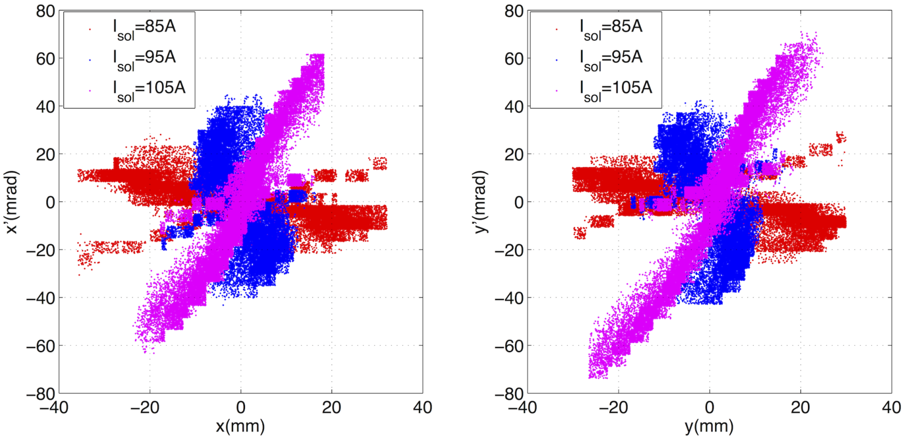

(a) (b)

Figure 6.4. Comparison of the phase space plots of the proton beam measured with different solenoid currents (red: $I_{sol} = 85$ A, blue: $I_{sol} = 95$ A, magenta: $I_{sol} = 105$ A).

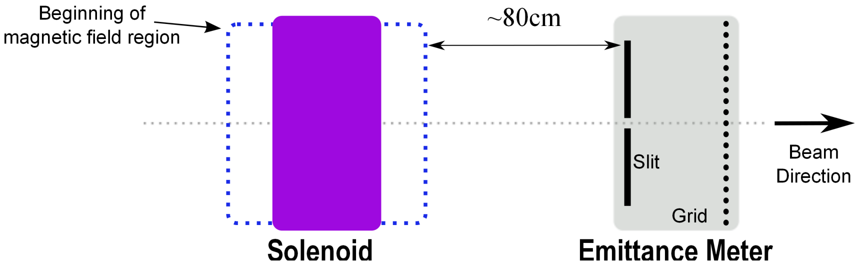

Figure 6.5. Sketch of the measurement set-up at 45 keV.

Space charge compensation (also addressed as space charge neutralization) occurs due to the ionization of the residual gas [54] caused by the collision of the particles in the main beam with the residual gas molecules. Space charge compensation occurs both for the proton and H$^-$ beams [55, 56]. However, the mechanism is different for each case. In the case of a proton beam, after the ionization of the residual gas molecules, the positive ions are pushed towards the vacuum chamber and the electrons are trapped in the positive potential of the proton beam. However, in the case of an H$^-$ beam, the electrons are pushed away and the positive ions are trapped. In both cases, the potential generated by the beam itself is reduced by the potential of the trapped particles. The amount of space charge compensation can not be calculated with PATH, however, the dynamics of the main beam can still be modeled by setting the beam current to a lower value (effective beam current, I_{eff}) which depends on the compensation factor. The space charge compensation can be controlled (up to some extent) by injecting different types of gas and by changing the gas pressure in the LEBT [57]. The Linac4 LEBT has a gas injection system to control the density of the residual gas.

In order to determine the effective beam current and to obtain the particle distribution for further simulations, the generated beams shown in Figure 6.3 were backtracked using PATH code to the beginning of the first solenoid (where magnetic field starts in Figure 6.5). In principle, if I_{eff} is set to the correct value, after backtracking, the phase space plots of all three beams should be identical. Therefore, in order to estimate the correct value of I_{eff}, all three beams were backtracked by varying I_{eff} between zero and 15 mA, and for each I_{eff} value, the phase space plots of the backtracked beams were compared to each other. For the comparison of phase space plots of two different beams, the mismatch factor given in Equation 6.1 [58] was used. In the equation, M_{ij} is the mismatch factor calculated from the i^{th} and j^{th} beams and Δ_{ij} is calculated from the Twiss parameters of the beams as shown in Equation 6.2. The mismatch factor, M, is dimensionless and it gives an indication of how different the rms ellipses of the two beams are in the phase space. If the ellipses are identical then M is equal to zero.

$$M_{ij} = \frac{1}{2}\left(\Delta_{ij} + \sqrt{\Delta_{ij}^2 + 4\Delta_{ij}}\right) \tag{6.1}$$

$$\Delta_{ij} = (\alpha_i - \alpha_j)^2 - (\beta_i - \beta_j)(\gamma_i - \gamma_j) \tag{6.2}$$

In order to estimate for which I_{eff}, all three backtracked beams are closer to each other, a total mismatch factor is defined as $M_T = \sqrt{M_{12}^2 + M_{23}^2 + M_{13}^2}$. The total mismatch factor was calculated for each transverse plane and for each set of three beams obtained from backtracking with different I_{eff}.

Figure 6.6 shows M_T calculated after backtracking with various effective beam

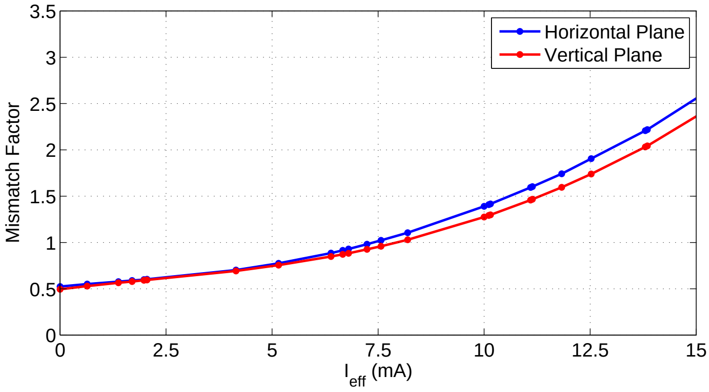

Figure 6.6. Total mismatch factor for proton beams backtracked with different effective beam currents.

currents. The result presented in the figure indicates that both in horizontal and vertical planes, the phase space plots of all three beams are closest to each other when backtracked with effective beam current of zero. The horizontal phase spaces of the

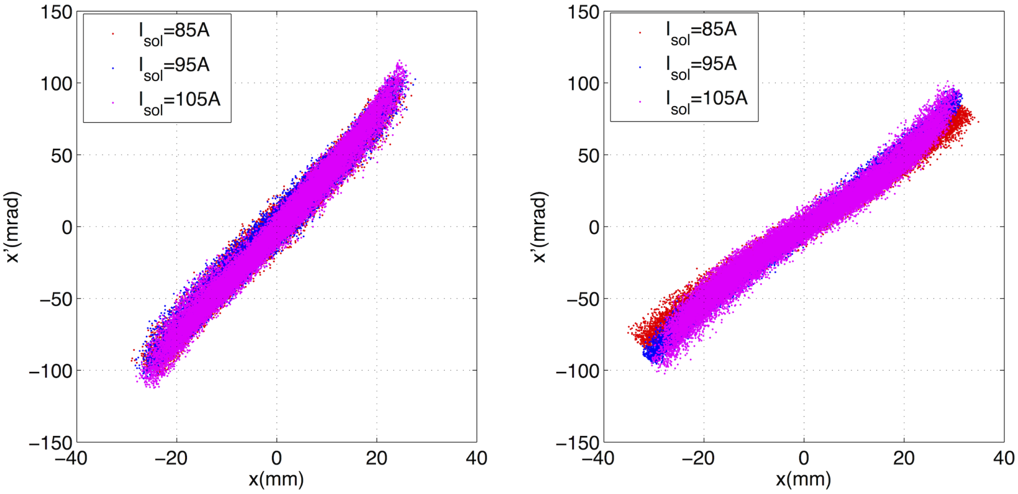

(a) (b)

Figure 6.7. The comparison of the phase space plots of the three proton beams backtracked (a) with $I_{eff} = 0$ mA and (b) with $I_{eff} = 15$ mA (red: $I_{sol} = 85$ A, blue: $I_{sol} = 95$ A, magenta: $I_{sol} = 105$ A).

backtracked beams were plotted together both for $I_{eff} = 0$ mA and $I_{eff} = 15$ mA. Figure 6.7a and 6.7b show the phase space plots of the three beams backtracked with

$I_{eff} = 0$ mA and $I_{eff} = 15$ mA, respectively. As it can be seen in Figure 6.7b, when the measured beams were backtracked with $I_{eff} = 15$ mA the phase space plots of the three beams were different from each other. However, for the case of backtracking with $I_{eff} = 0$ mA, the phase space plots of all three beams seem to overlap well (Figure 6.7a).

The space charge compensation factor can be calculated using Equation 6.3 [59] where η is space charge compensation factor, I^*_{eff} is the effective beam current which minimizes M_T, and I_{beam} is the beam current measured with the Faraday Cup. Considering $I_{eff} = 0$ mA gives the minimum value of M_T, space charge compensation for the proton beam in Linac4 LEBT was 100 per cent.

$$\eta = 1 - \frac{I^*_{eff}}{I_{beam}} \tag{6.3}$$

Figure 6.8 shows the phase space plots of the proton beams after backtracking to the solenoid entrance with $I_{eff} = 0$ mA. Phase spaces of all three beams are almost identical when backtracked with a correct effective beam current. Notice that there may be small differences arising from the errors in the emittance scans.

6.2.1.1. Investigating the Other Particle Species After the First Solenoid. Figures 6.3 and 6.4 clearly show the trace of the H^0 particles but not that of H_2^+ and H_3^+. However, during the former measurement periods, emittance measurements clearly showed also the traces of H_2^+ and H_3^+ [50, 51, 53]. Even if these particle species are not of primary interest, tracking these particles to the emittance meter location and comparing the simulation and measurement results help to understand the system better, verify the accuracy of the tracking code and the simulation methods.

The beam whose phase space plots are shown in Figures 6.8b and 6.8e was taken as a starting point. The phase spaces were populated with H^0, H_2^+ and H_3^+ particles assuming that each type of particle beam has similar Twiss parameters. After the addition of the other species, the new beam with different types of particles had 70 per

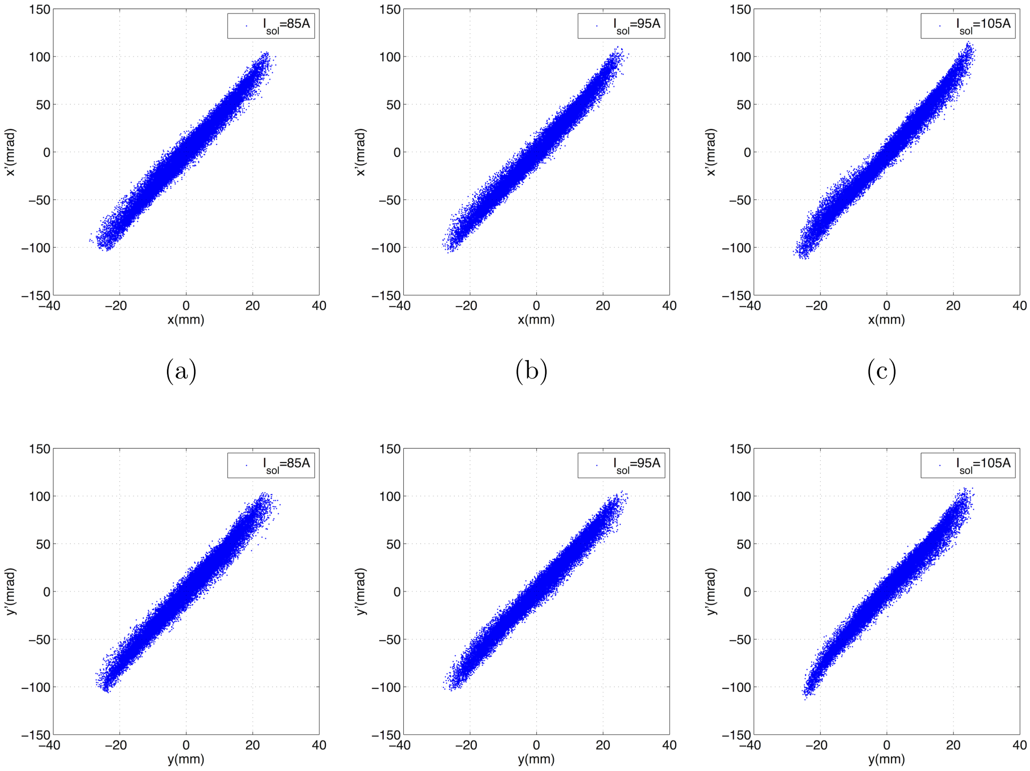

(a) (b) (c)

(d) (e) (f)

Figure 6.8. Phase space plots of the proton beams backtracked to the solenoid entrance with $I_{eff} = 0$ mA. The first row shows the horizontal and the second row shows the vertical phase space plots. From left to right, $I_{sol} = 85$ A, $I_{sol} = 95$ A, $I_{sol} = 105$ A, respectively.

cent protons, 15 per cent H_2^+, 10 per cent H_3^+ and five per cent H^0.

The beam, which consists of different particle types, was tracked through the solenoid to the emittance meter (slit location) with $I_{sol} = 85$ A and $I_{sol} = 95$ A in order to compare with the emittance measurements. Figure 6.9 shows the comparison of the phase plots from simulations and measurements. As it can be seen from the plots, the traces of H^0 particles from the measurements agree very well with the simulations. However, other particle types are not visible in the measurement. This may be due to the low resolution of the measurement and small separation of the phase space plots of different species.

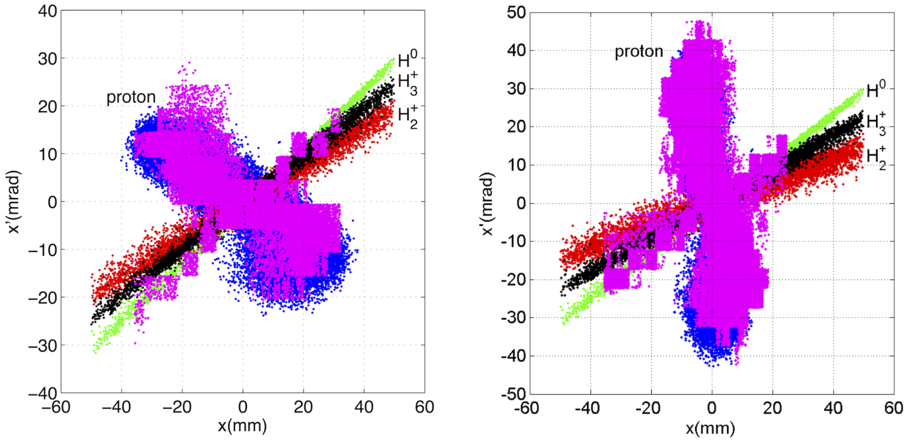

(a) (b)

Figure 6.9. The comparison of the phase space plots from simulations and measurements for $I_{sol} = 85$ A and $I_{sol} = 95$ A (the particle species are indicated on the plot).

The simulations showed that for $I_{sol} = 140$ A the phase space plots of different particle types would nicely separate at the slit location. Therefore, the solenoid current was set to 140 A and the horizontal and vertical phase spaces were measured. Figure 6.10 shows the comparison of the simulation and measurement results. As it can be

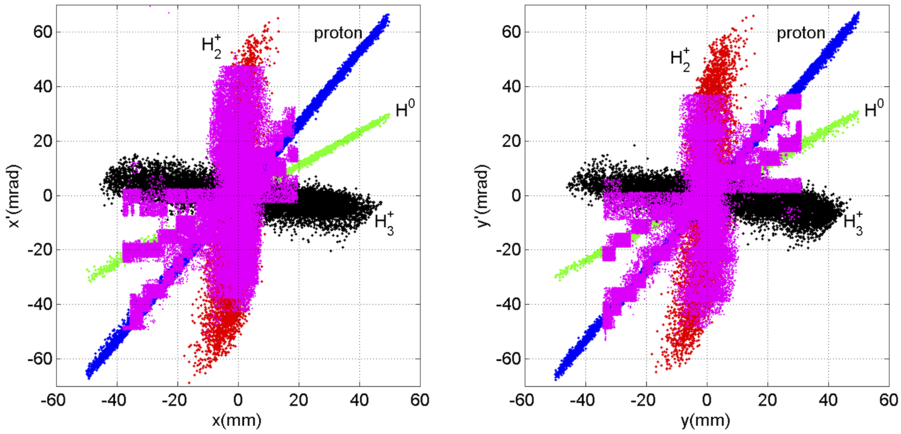

(a) (b)

Figure 6.10. The comparison of (a) horizontal and (b) vertical phase space plots from simulation and measurements for $I_{sol} = 140$ A (the particle species are indicated on the plot).

seen in the phase space plots, the simulation and measurement results agree well except for H_3^+. In the measurement the signal from H_3^+ is still very weak. The measurement data is cut in x and y direction but still it can be seen that the orientation of the phase space plot of different types of particles agrees well with the measured phase space plot.

6.2.2. Measurements with the H^- Beam

In February 2013, the measurements in the LEBT started with a temporary H^- source which can deliver a beam current of 14 mA [60]. The measurement set-up for the H^- beam and the proton beam was the same (see Figure 6.2). Horizontal and vertical emittance measurements were taken with different solenoid currents. Figure 6.11 shows the horizontal phase space plots obtained from the emittance measurement for $I_{sol} = 90$ A, $I_{sol} = 95$ A and $I_{sol} = 100$ A[10] .

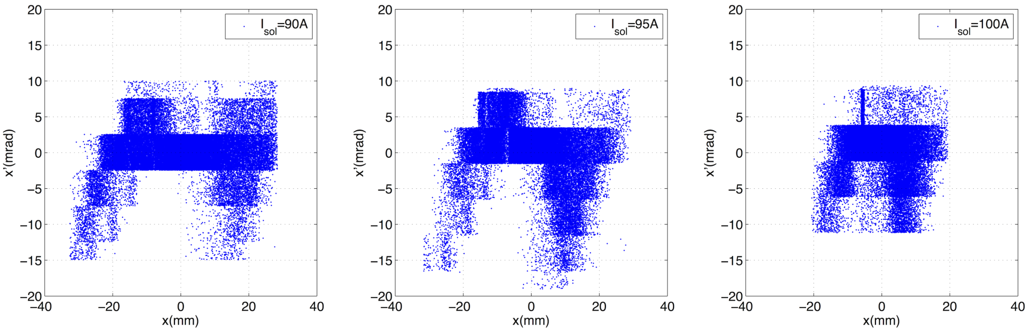

(a) (b) (c)

Figure 6.11. The horizontal phase space plots of H^- beams generated from the emittance measurement data with (a) $I_{sol} = 90$ A, (b) $I_{sol} = 95$ A, (c) $I_{sol} = 100$ A.

Three multi-particle H^- beams were generated from the emittance measurement data and backtracked to the solenoid entrance. The procedure of varying the effective beam current for backtracking, as explained in Section 6.2.1, was also applied to the H^- beams. The total mismatch factor (see Section 6.2.1) was calculated after backtracking with each effective beam current. Figure 6.12 shows the total mismatch factor

---

[10] Since the beam is symmetric in the LEBT, for simplicity, only the horizontal phase space plots will be given in this section.

calculated for different effective beam currents between zero and 14 mA. As it can be seen in the figure, the calculation predicts the value of the I_{eff} as 3 mA. Considering the beam current of 14 mA measured at the Faraday Cup, 3 mA effective beam current corresponds to 78 per cent space charge compensation. The space charge compensation factor in Linac4 LEBT with H^- ions was predicted to be 80 per cent by utilizing another method which uses the ion source extraction simulations [56].

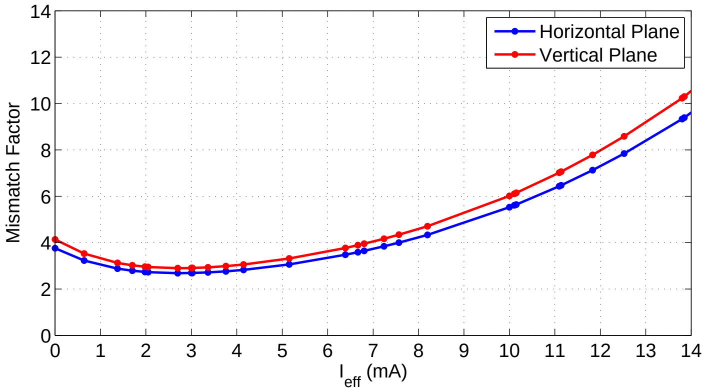

Figure 6.12. Total mismatch factor for H^- beams backtracked with different effective beam currents.

Figure 6.13 shows the comparison of the phase space plots of the three beams backtracked with $I_{eff} = 0$ mA, $I_{eff} = 3$ mA and $I_{eff} = 14$ mA. As it can be seen in the figure, the phase space plots of the beams are closer to each other for $I_{eff} = 3$ mA. In Figures 6.13a and 6.13c, there is a clear difference in the orientation of the phase space plots. However, in the case of Figure 6.13b, for $I_{eff} = 3$ mA, the orientation of the phase space plots are the same. The small emittance of the beam measured with $I_{sol} = 100$ A is due to the error in the measurement which resulted in cutting away some part of the beam in x' direction (see Figure 6.11c).

6.3. Matching the Beam to the RFQ

Starting from the emittance measurement data, it was possible to obtain a representation of the particle distribution at the source exit using backtracking. The distribution measured with $I_{sol} = 95$ A and backtracked to the source exit was taken as a reference H^- beam to find the setting of the solenoids for the RFQ matching.

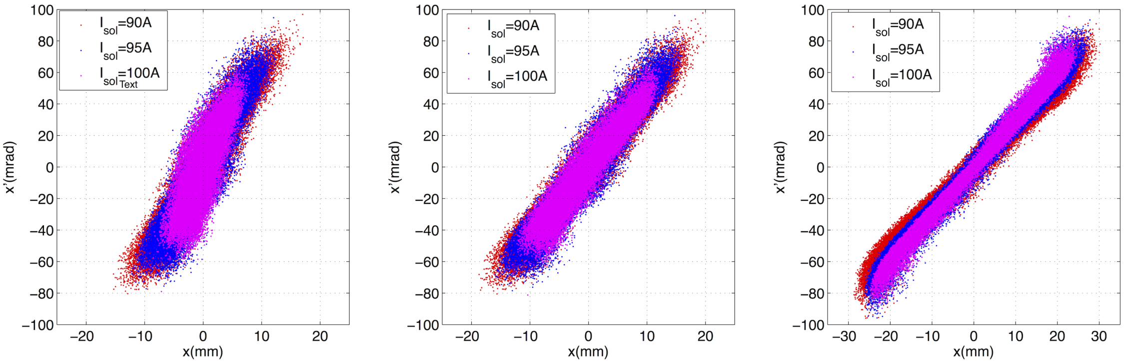

(a) (b) (c)

Figure 6.13. The comparison of the phase space plots of the three H$^-$ beams backtracked with (a) $I_{eff} = 0$ mA, (b) $I_{eff} = 3$ mA and (c) $I_{eff} = 14$ mA, respectively (red: $I_{sol} = 90$ A, blue: $I_{sol} = 95$ A, magenta: $I_{sol} = 100$ A).

Using PATH code, the currents of the first and second solenoid for RFQ matching were found as 87 A and 118 A, respectively. Before removing the emittance meter for the installation of the second solenoid, the first solenoid current was set to 87 A and the emittance was measured at the matching condition. The measured normalized rms emittance for the transverse plane was 0.6 mm.mrad after averaging over the horizontal and vertical planes [60]. Compared to the target transverse normalized rms emittance of 0.31 mm.mrad after the RFQ, it can be seen that the measured value with the temporary H$^-$ source was much higher than what was considered to be accelerated in the RFQ. Therefore, along with the beam commissioning, the work on the source for the current and emittance improvement continued.

7. 3 MeV COMMISSIONING STAGE

The 3 MeV commissioning stage started in March 2013 with the measurements after the RFQ. The RFQ and MEBT were commissioned first in the Linac4 3 MeV test stand. Then, in the second half of 2013 they were transported into the Linac4 tunnel to their final location. The commissioning period in the tunnel started in November 2013 [17] with recommissioning of the RFQ and MEBT[11] .

During the 3 MeV commissioning stage, besides characterization of the beam parameters, several other issues were addressed. The major ones were confirming the RFQ performance, validating the chopping system operation and finding the RF phase and amplitude setting of the cavities on the MEBT. This chapter discusses the measurement set-up, techniques and the results related to 3 MeV beam commissioning.

7.1. Movable Diagnostic Bench

The beam commissioning at 3 MeV (and also at 12 MeV) was performed using a movable diagnostic bench. The bench was consecutively used for the beam measurements after the RFQ, the MEBT line and the first tank of the DTL. Figure 7.1 shows the layout of the bench. The bench has a straight section and a spectrometer. The straight part is equipped with a slit-grid emittance meter, a BSM, two BPMs and a BCT. The spectrometer has a BCT and a SEM grid as a profile monitor.

The beam current through the BCTs was the first parameter to check when the machine started. The BCT on the straight section of the bench is installed as close as possible to the beginning of the measurement bench to help measuring the transmission through the structure upstream of the bench. The second BCT was installed on the spectrometer line to help adjusting the bending magnet current to deliver the beam safely to the SEM grid and to the beam dump.

---

[11] The location of the measurements related to the RFQ or MEBT will not be stated unless it is necessary.

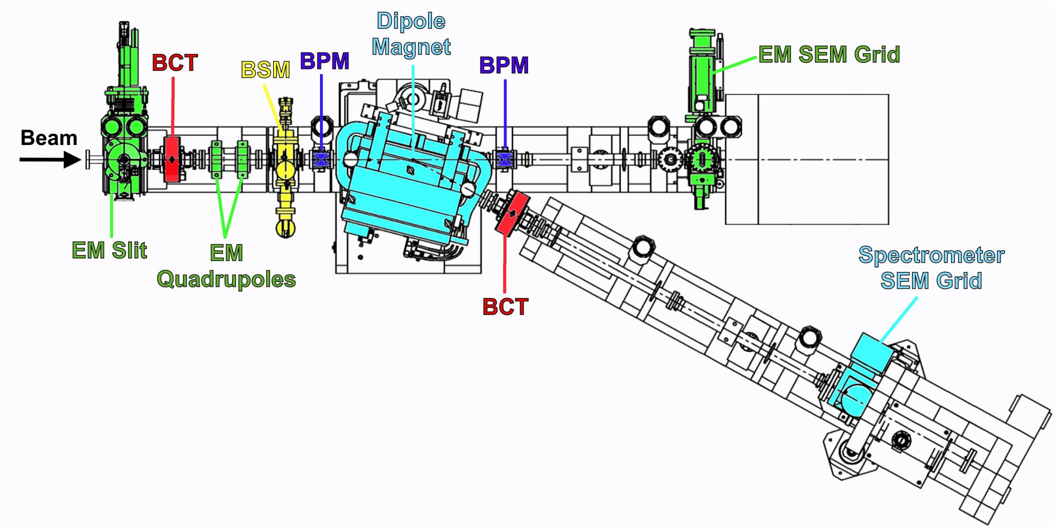

Figure 7.1. Movable diagnostic bench for 3MeV and 12MeV beam measurements.

The two electromagnet quadrupoles were used during the emittance measurements to increase the angular acceptance of the system. They were also used during the energy spread measurements to minimize the β function at the spectrometer SEM grid location (see Section 5.8).

7.2. Commissioning of the Radio Frequency Quadrupole

The beam was first accelerated through the RFQ in March 2013 [44]. The LEBT solenoids were at 87 A and 118 A, respectively. The values were predicted using the measured beam at the LEBT as an input to the tracking code PATH for RFQ matching (see Section 6.3). Figure 7.2 shows the first sign of the beam after the RFQ measured with the BCT, right after the RFQ. The beam current was recorded as 16 mA in the LEBT and 10 mA after the RFQ, which corresponds to 62 per cent transmission. After adjusting the steering magnets and fine tuning the solenoid currents in the LEBT, the transmission could be increased up to 75 per cent (12 mA after the RFQ). The final solenoid settings were within three per cent of the ones predicted with PATH, which proved the accuracy of the LEBT modelling and particle tracking. It is important to note that the target transmission through the Linac4 RFQ is 95 per cent [12]. The measured 75 per cent transmission efficiency was expected from the simulations due to

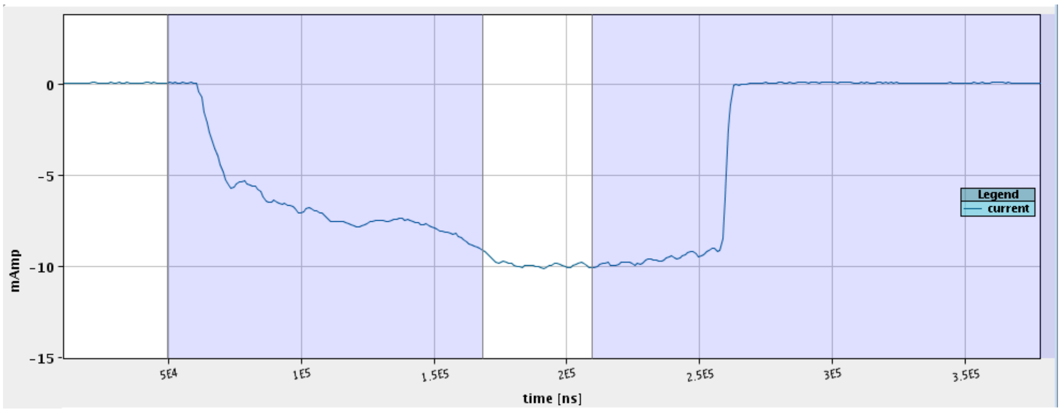

Figure 7.2. The first measurement of the 3 MeV H^- beam with the BCT after the RFQ.

the large emittance of the injected beam.

The next step was to check the energy of the beam coming out of the RFQ. Therefore, the beam was sent to the spectrometer arm of the diagnostic bench. The BCT in the spectrometer measured a similar value for the beam current which proved that the beam measured after the RFQ was at 3 MeV.

7.2.1. Transmission through the RFQ as a Function of RF Power

The performance of the RFQ and the calibration of the RF amplitude were confirmed by varying the power in the RFQ and measuring the transmission. The transmission through the RFQ was measured as a function of the RF power in the RFQ for different values of the gas pressure in the LEBT. The measured values were compared to the expected transmission from the simulations. The transmission through the RFQ was studied with Parmteqm [25], considering the measured particle distribution in the LEBT. Figure 7.3 compares the measured characteristic curve of transmission vs. RF power in the RFQ for different LEBT gas pressures and the expected transmission from the simulations. The measured transmission agrees well with the expected values especially around the operational power level of 390 kW. During the measurements, the solenoid magnets were optimized for the case corresponding to $P = 1 \cdot 10^{-6}$ mbar.

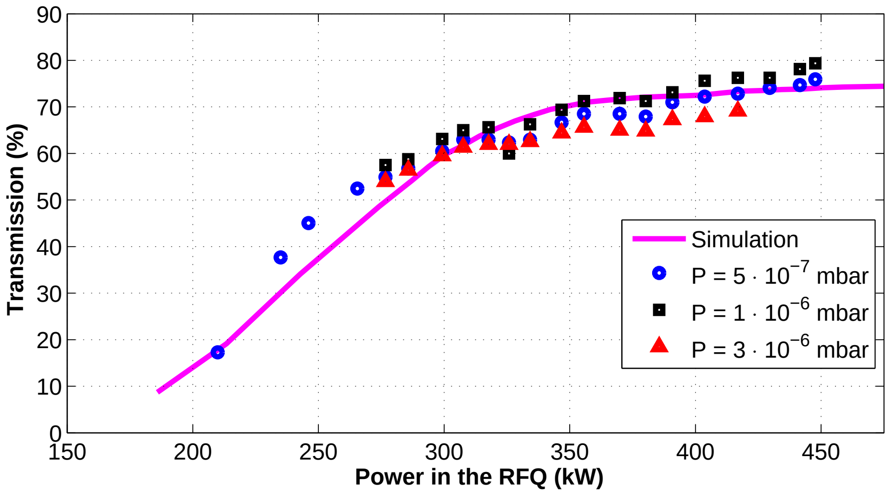

Figure 7.3. Transmission through the RFQ as a function of the RFQ power for three different values of the LEBT pressure.

7.2.2. Transverse Emittance Reconstruction After the RFQ

When the measurements started after the RFQ, at the 3 MeV test stand, the slit-grid emittance meter was not fully operational[12] . Therefore, other solutions were found to determine the emittance of the beam after the RFQ. During the measurements after the RFQ, two electromagnet quadrupoles were installed between the RFQ and the movable diagnostic bench in Figure 7.1. The transverse beam profile was measured using the slit of the emittance meter and the BCT downstream [45] for various quadrupole magnet settings. Measured beam profiles were used for reconstructing the transverse phase space plots at the RFQ exit with the forward method (see Section 5.4.4).

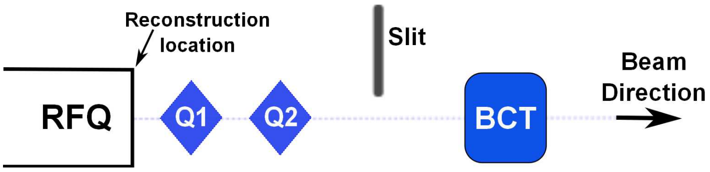

Figure 7.4. The measurement set-up for the emittance reconstruction.

Figure 7.4 shows a drawing of the set-up with the two quadrupole magnets (Q_1

---

[12] 3 MeV test stand was aimed to be the test bed for most of the commissioning strategy and calibration of diagnostics [61].

and Q_2), slit of the emittance meter and the BCT right after the slit. During the measurements, the slit was not used for selecting a slice of the beam but rather as a scraper to change the beam intensity. In order to measure the beam profile, the slit blade was inserted into the vacuum chamber step by step and the beam intensity was measured with the BCT as a function of the blade position. By subtracting the measured intensity from the maximum intensity measured, the losses were calculated as a function of the slit position. The slope of the curve of losses for each slit position gives the beam intensity at that specific position. Therefore, the beam profile was obtained by taking the derivative of the curve along the slit position.

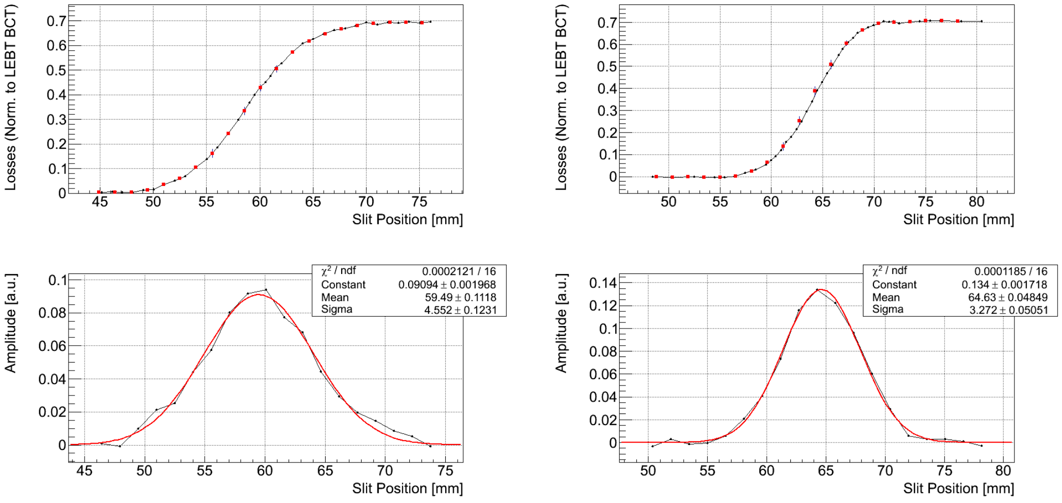

(a) (b)

Figure 7.5. The curve of losses (top) and the calculated beam profiles (bottom) for the (a) horizontal and (b) vertical planes.

Figures 7.5a and 7.5b show the measured curves of losses and the calculated beam profiles for the horizontal and vertical planes, respectively. The beam intensity measured after the RFQ was normalized to the intensity measured at the LEBT to take into account any possible oscillations in the beam current. Therefore, the maximum value of the curve of losses is around 0.7 which is actually the normalized transmission efficiency of the RFQ.

Using different quadrupole magnet settings, five beam profiles were measured for each transverse plane. Using the measured profiles, the beam phase space plots were reconstructed at the RFQ exit (see Figure 7.4). After the reconstruction, the beam measured at the LEBT and tracked through the RFQ with Parmteqm was compared to the reconstructed beam after the RFQ. Figure 7.6 shows the comparison of the phase space plots of the beam tracked with Parmteqm and the beam reconstructed at the RFQ exit. The reconstructed beam has a smaller emittance in both transverse phase spaces. The tracked beam has a normalized rms emittance of 0.36 mm.mrad and 0.37 mm.mrad in horizontal and vertical planes, respectively. The normalized rms emittance values for the reconstructed beam are 0.32 mm.mrad and 0.34 mm.mrad in horizontal and vertical planes, respectively.

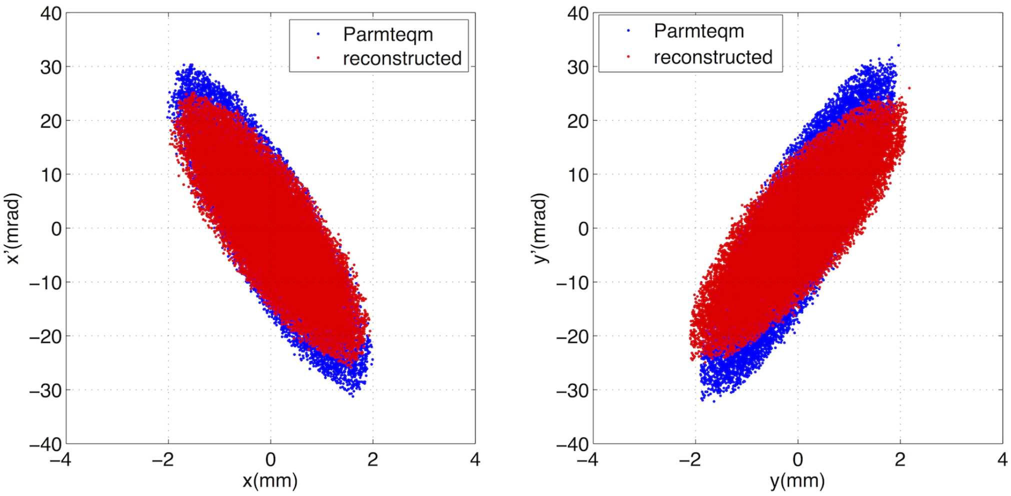

(a) (b)

Figure 7.6. The comparison of the (a) horizontal and (b) vertical phase space plots of the beam measured in LEBT then tracked through the RFQ with Parmteqm and the beam reconstructed at the RFQ exit.

The beams from Parmteqm simulation and reconstruction were tracked from the RFQ exit to the slit location where the beam profiles were measured. Each measurement with the slit and BCT was simulated. The measured data were compared to the simulation result in order to see which beam describes the measurements better. Figure 7.7 shows the comparison of curves of losses from measurement and simulations for the two cases shown in Figure 7.5. As it can be seen in Figures 7.7a and 7.7b, the reconstructed beam describes better what was measured after the RFQ.

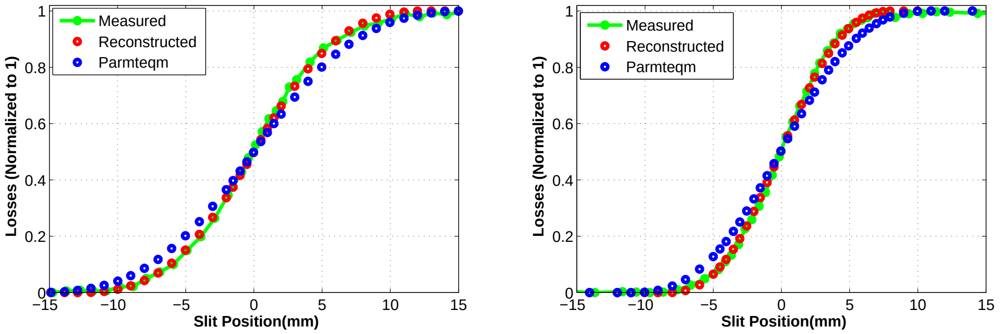

(a) (b)

Figure 7.7. The comparison of curves of losses from measurement and simulations for the (a) horizontal and (b) vertical profile measurements.

The same method was used for the transverse emittance reconstruction where the beam profile was measured with a MEBT wire scanner [62].

7.3. MEBT Commissioning

After the commissioning of the RFQ, the MEBT line was installed and the diagnostic bench shown in Figure 7.1 was moved to the end of the MEBT line. Figure 7.8 shows a drawing of the MEBT line with the RF cavities, quadrupole magnets and wire scanners colored. Besides the instruments on the diagnostic bench, two wire scanners (red in the figure) of the MEBT line were also used during the commissioning.

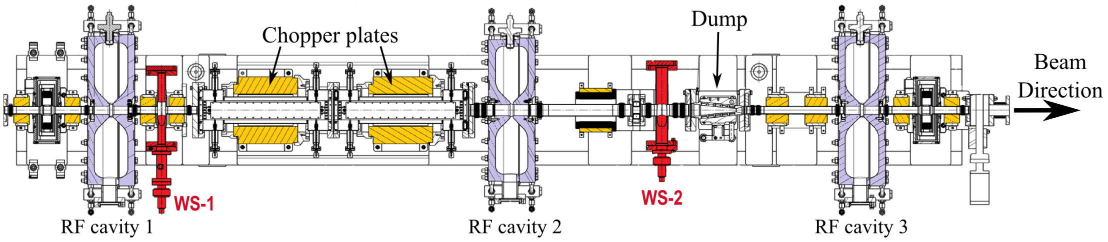

Figure 7.8. Drawing of the MEBT line with quadrupole magnets (yellow), RF cavities and wire scanners (red) [35].

7.3.1. Testing the Operation of the Chopping System

The first performance test of the chopper system was to chop some part of the pulse and observe the beam current along the pulse with the BCT (between the last two quadrupoles in Figure 7.8) downstream of the MEBT dump. Figure 7.9 shows the beam current along the pulse measured after the MEBT dump. As it can be seen in the figure, the bunches at the middle part of the pulse were chopped.

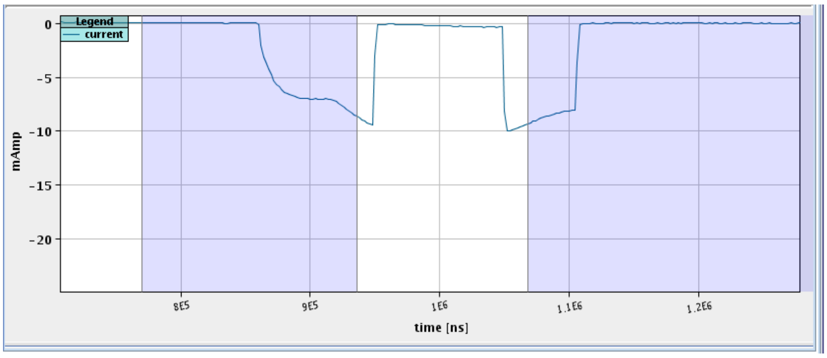

Figure 7.9. Beam current along the pulse from the BCT downstream of the MEBT dump when the chopper is on.

In order to see the separation between the main and the chopped beam, the profile of the beam was measured with the second wire scanner which is located upstream the MEBT dump (see Figure 7.8). A measured vertical profile along the pulse is given in Figure 7.10. The solid black lines show the beam profile along the pulse with a time

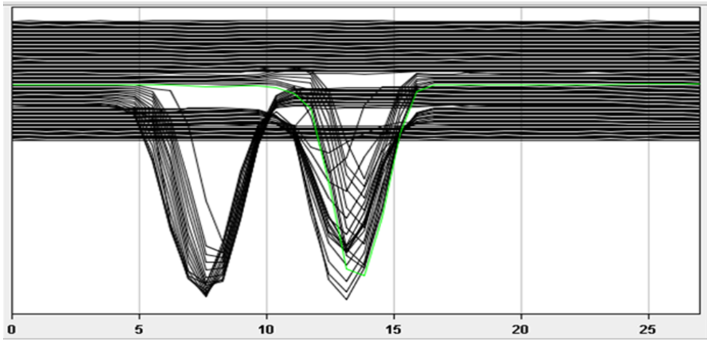

Figure 7.10. Beam vertical profile (along the pulse) on the wire scanner before the MEBT dump when the chopper was on. Horizontal axis is the wire position in millimeters.

resolution of 6 μs. The profile on the right belongs to the main beam and the one on the left belongs to the chopped beam. As it can be seen, the chopped bunches were separated nicely even before the dump at the wire scanner location.

The quadrupole magnet (L4L.RQF.371) between the chopping system and the MEBT dump plays an important role on the chopping efficiency. L4L.RQF.371 is defocusing in the vertical plane, therefore, helps deflecting the chopped bunches. However, if the gradient of the magnet is too high, then the size of the main beam would be too big to pass through the MEBT dump.

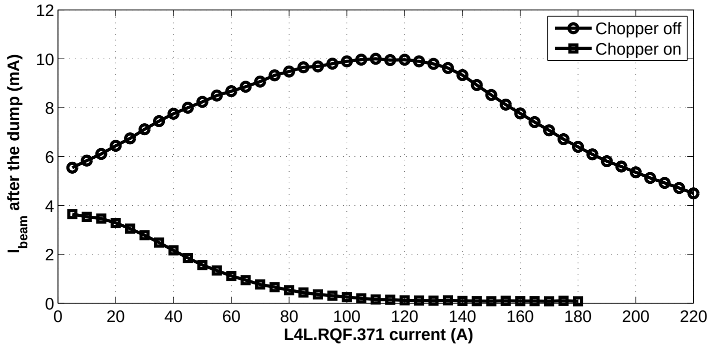

Figure 7.11. The beam current downstream of the MEBT dump as a function of L4L.RQF.371 setting.

The beam current downstream the MEBT dump was measured as a function of L4L.RQF.371 setting. Figure 7.11 shows the variation of the beam current with the quadrupole magnet setting both for the chopper on and off cases. As it can be seen in the figure, by setting the quadrupole magnet current to a value around 120 A, the deflected bunches can be stopped at the dump and the transmission of the main beam can be maximized simultaneously.

7.3.2. Setting the RF Phase and Calibrating the Amplitude of the MEBT Cavities

Determining the operational settings of the MEBT RF cavities was crucial for an optimized matching of the beam from the RFQ to the DTL. Also, calibrating the amplitude of the cavities was important to control and tune the MEBT during the operation. The calibration of the RF amplitude and determination of the RF phase settings of each cavity were done by measuring the kinetic energy gain of the beam through the cavity as a function of RF phase for various RF amplitudes. The cavities were turned on one by one and studied independently.

Figure 7.12 shows the normalized energy gain of the beam through a cavity as a function of the RF phase (see Section 2.1). In principle, one can vary the RF phase of the cavity and measure the energy gain to sample the curve of energy gain (blue curve in Figure 7.12). After obtaining the energy gain vs. RF phase curve, the effective axial RF voltage, V_0T, can be calculated and the four main RF phase points (red dots in Figure 7.12) can be determined.

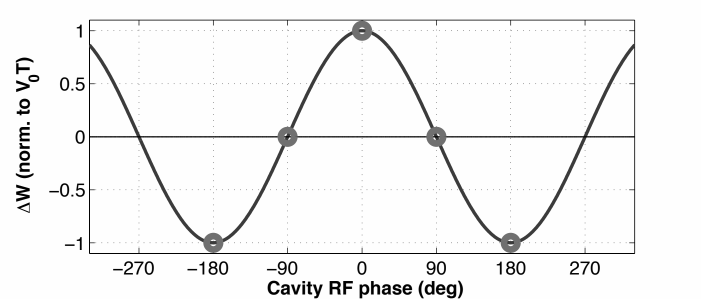

Figure 7.12. Normalized energy gain as a function of the cavity RF phase and four main RF points (the crest, through and two zero crossings).

The energy gain through each cavity was measured with the spectrometer arm of the measurement bench. For each MEBT cavity, the RF phase was varied over a range of 360° and the beam was centered on the spectrometer SEM grid by adjusting the current of the bending magnet. By centering the horizontal profile on the SEM grid the beam was forced to follow the same path (with the same bending angle) through the bending magnet regardless of its energy.

During the measurements, for each RF phase, the bending magnet current, which centers the beam profile on the SEM grid, was recorded. After the scan of the RF phase, a cosine function with a constant offset was fitted to the data. Figure 7.13

shows the measurement data related to the first MEBT cavity and the fitted curves for two different levels of the forward RF power sent to the cavity.

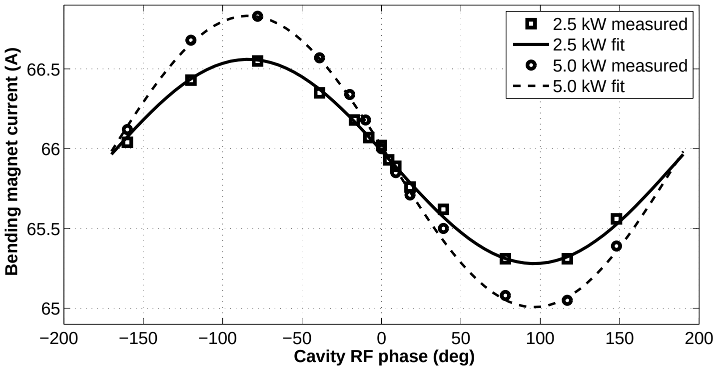

Figure 7.13. Bending magnet current (representing the energy gain) as a function of the RF phase of the first MEBT cavity for the two forward power levels.

Equation 7.1 shows the form of the fit function where ϕ_{RF} is the RF phase of the cavity. After fitting, the three unknowns (I_0, ΔI_{max} and $\Delta\phi$) could be determined. In the equation, I_0 gives the bending current which centers the beam on the SEM grid when there is no energy gain. ΔI_{max} shows how much the current was changed to center the beam when the energy gain was maximum. $\Delta\phi$ shows the shift of the curve in the positive ϕ_{RF} direction.

$$f(\phi_{RF}) = I_0 + \Delta I_{max} cos(\phi_{RF} - \Delta\phi) \tag{7.1}$$

Since the bending angle and the path of the beam through the bending magnet is the same for each case, considering the magnetic field is directly proportional to the magnet current, it can be shown from Equation 5.10 that $\Delta p/p_0$ is equal to $\Delta I_{max}/I_0$. Inserting this relation and Equation 2.6 into Equation 2.17, one can find the relation for effective axial RF voltage as in Equation 7.2.

$$V_0 T = \frac{W_0}{q}\left(\frac{\gamma_r + 1}{\gamma_r}\right)\frac{\Delta I_{max}}{I_0} \tag{7.2}$$

The measured and calculated V_0T for the first MEBT cavity with 2.5 kW and 5.0 kW forward power (see Figure 7.13) were 58.5 kV and 83.0 kV respectively[13] .

The measurement and analysis process explained above was repeated for all three MEBT RF cavities for several forward power levels to calibrate the RF amplitude of each cavity. The calibrations for the cavity amplitudes were taken into account for the Linac4 control system.

The beam dynamics design requires the MEBT RF cavities to operate at the bunching phase, which is $-90°$. From the fitting, the two zero crossings of the energy gain vs. RF phase curve can be calculated by $(90° - \Delta\phi)$ and $(90° + \Delta\phi)$. However, the information obtained from the phase scan of the cavities is not enough to determine which zero crossing corresponds to the bunching phase. In order to do that, the longitudinal phase spread of the beam was measured with the BSM [63].

7.3.3. Longitudinal Emittance Reconstruction at the RFQ Exit

After setting the phase and calibrating the RF amplitude of the MEBT cavities the forward method was applied to the longitudinal plane to reconstruct the emittance at the RFQ output [62]. For the measurements, the voltage of the second MEBT cavity was varied while keeping the RF phase at $-90°$ (at the bunching phase). The voltage and phase of the first cavity were kept constant at the operational values and the third cavity was turned off and detuned. The longitudinal phase spread of the beam was measured as a function of cavity voltage with the BSM in the diagnostic bench (see Figure 7.1).

Figure 7.14 shows the longitudinal phase space plots, at the RFQ exit, expected from the RFQ simulations and the one reconstructed from the measurement data. The longitudinal rms emittance values are 0.19 deg.MeV and 0.16 deg.MeV from Parmteqm and reconstruction, respectively.

---

[13] The estimated values for V_0T from the RF measurements were 60 kV and 84 kV for 2.5 kW and 5.0 kW forward power, respectively.

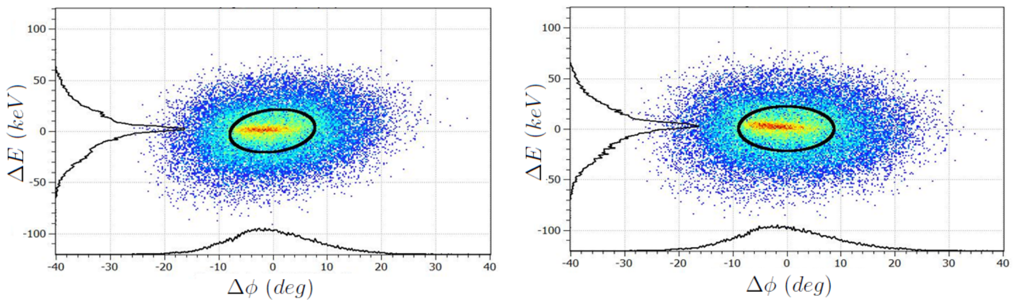

(a) (b)

Figure 7.14. Longitudinal phase space plot at the RFQ output (a) expected from Parmteqm simulations and (b) from reconstruction [62].

After the emittance reconstruction, the measured longitudinal rms phase spread was compared with the simulations. Figure 7.15 shows the comparison of the measured and simulated rms phase spread. The simulations were run both with the beam from Parmteqm and the reconstruction.

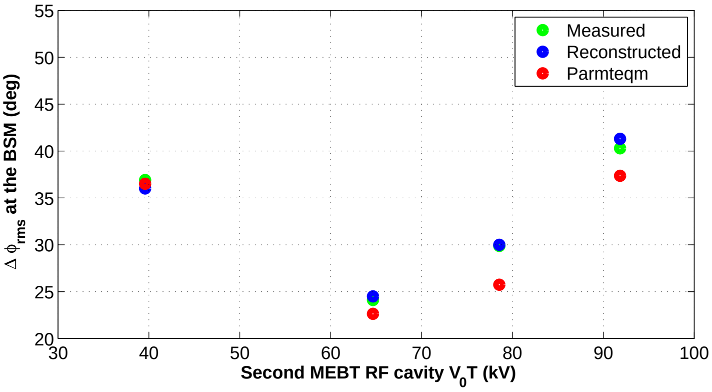

Figure 7.15. Comparison of the longitudinal rms phase spread at the BSM location from the measurement and simulations.

7.3.4. Commissioning the Emittance Meter with Quadrupole Magnets

Before the measurement bench was installed into the tunnel, in order to increase the angular acceptance of the emittance meter, two electromagnet quadrupoles were installed between the slit and the grid of the emittance meter (see Figure 7.1). Also, the Linac4 emittance meter application (see Section 5.4.1.1) had to be updated considering the effect of the quadrupole magnets as explained in Section 5.4.1. The correct operation of the emittance meter with two quadrupole magnets[14] was tested before proceeding with the analysis of the beam transverse phase spaces.

The slit-grid emittance meter measures the transverse phase spaces at the slit location. As it can be seen in Figure 7.1, EM quadrupoles are located downstream of the slit, therefore, the setting of the EM quadrupoles should not have any effect on the measured phase space plots (unless the transmission from the slit to grid changes). With the same setting of the MEBT line, transverse phase spaces of the beam were measured with three different EM quadrupole settings and then compared to each other. Table 7.1 shows the current values used for the quadrupole magnets for each set of measurements and the Twiss parameters of the beam in each transverse phase space .

Table 7.1. Twiss parameters from the emittance measurements with three different EM quadrupole magnet settings (β is in mm/mrad and ϵ is in mm.mrad).

EM Q_1(A)	EM Q_2(A)	α_x	β_x	ϵ_x	α_y	β_y	ϵ_y
70	50	0.1368	1.3203	0.2535	-0.2864	0.6829	0.2167
100	75	0.1363	1.3024	0.2608	-0.3195	0.6717	0.2347
170	130	0.1351	1.4702	0.2748	-0.3442	0.5564	0.2432

The values from the measurements have a fair agreement among them. The change in the values, as the quadrupoles get stronger, can be due to the reduction of the particle losses between the slit and the grid. Figure 7.16 shows the measured phase space plots for each setting of the EM quadrupoles.

---

[14] The two quadrupole magnets between the slit and the grid will be addressed as emittance meter quadrupoles (EM quadrupoles).

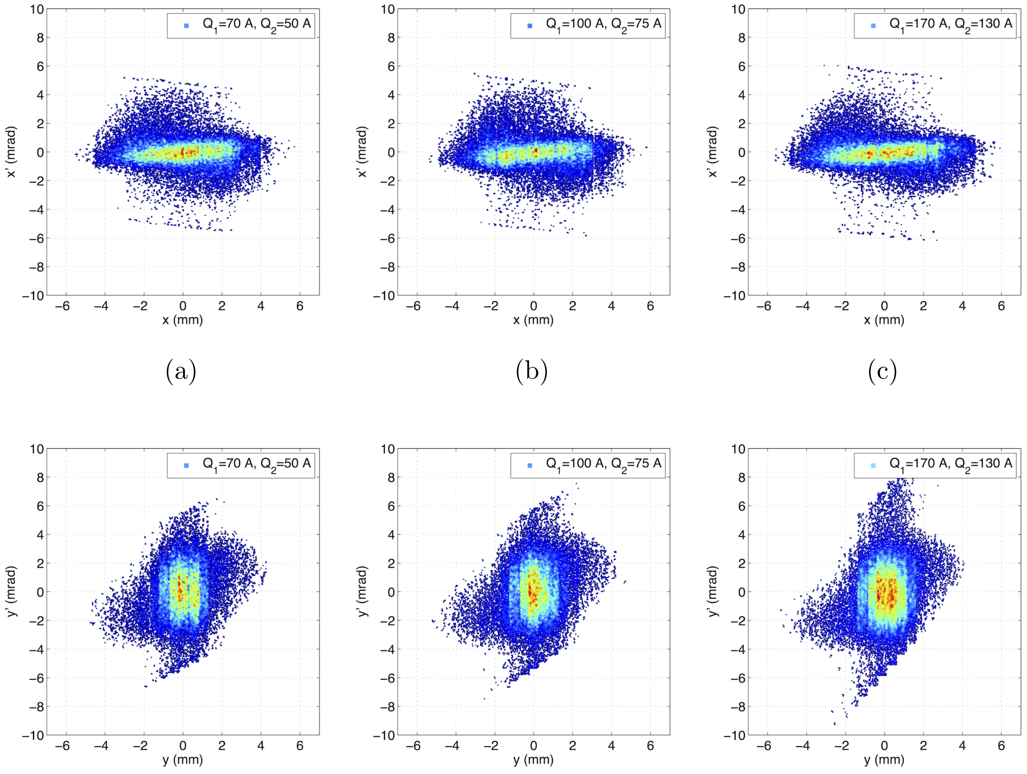

(a) (b) (c)

(d) (e) (f)

Figure 7.16. Measured phase space plots (first row: horizontal, second row: vertical) of the beam with different EM quadrupole settings. The electrical current through the magnets are indicated in the legend box of the plots.

7.3.5. Transverse Emittance Measurements after the MEBT

After the commissioning of the slit-grid emittance meter, several transverse emittance measurements were taken. At the time of the measurements, the beam current was around 10mA [35].

In order to check the calibration of the MEBT quadrupole magnets, five sets of measurements were taken by varying the last four MEBT quadrupole magnets (see Figure 7.8). Only three of the measurements will be presented in this thesis for the sake of brevity. Figure 7.17 shows the phase space plots of the multi-particle beams generated, at the slit location, based on the measurement data.

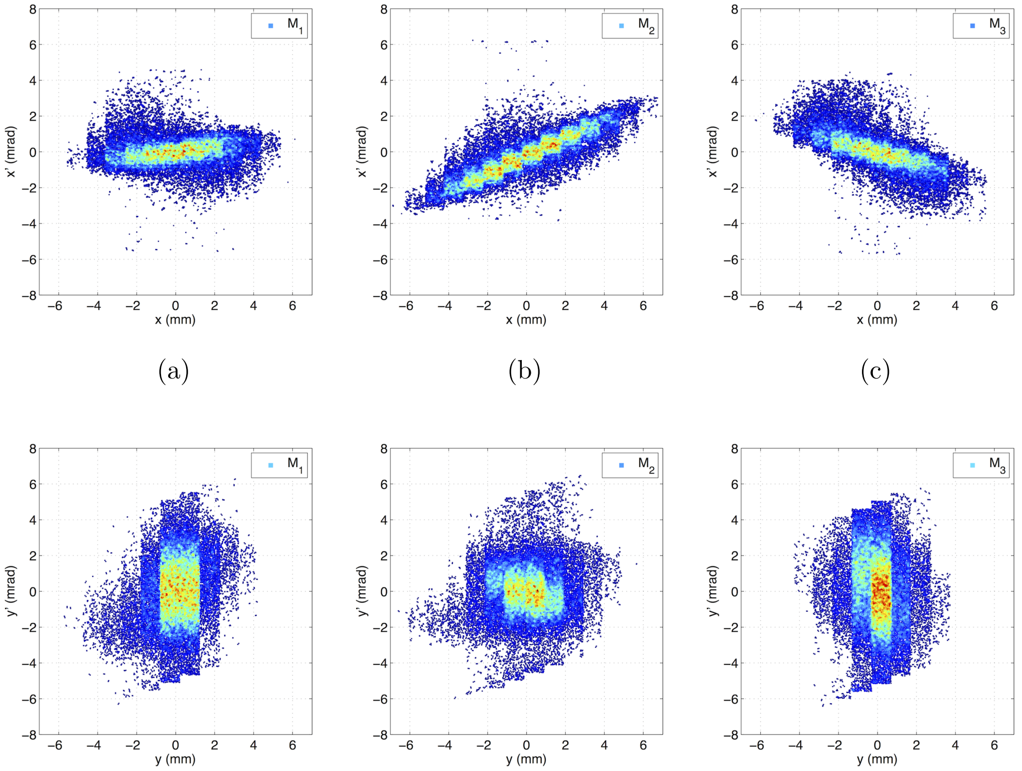

(a) (b) (c)

(d) (e) (f)

Figure 7.17. Measured phase space plots (first row: horizontal, second row: vertical) with different MEBT optics settings. M_1, M_2 and M_3 indicate the measurement number.

The longitudinal distribution of the generated beams were based on the simulations. The beam tracked through the RFQ was simulated further to the slit location. The longitudinal distribution of the simulated beam at the slit location was taken as a reference. The generated beams were backtracked from the slit location to the RFQ output plane by using the corresponding MEBT optics setting. The beam line from the RFQ output to the slit is around four meters long and contains 11 quadrupole magnets. Figure 7.18 shows the phase space plots of the backtracked beams at the RFQ output plane. As expected, the shape and orientation of the phase space plots are almost identical.

Having the same phase space plot for each beam after backtracking proves the MEBT quadrupole magnet calibrations, accuracy of the tracking code PATH and the

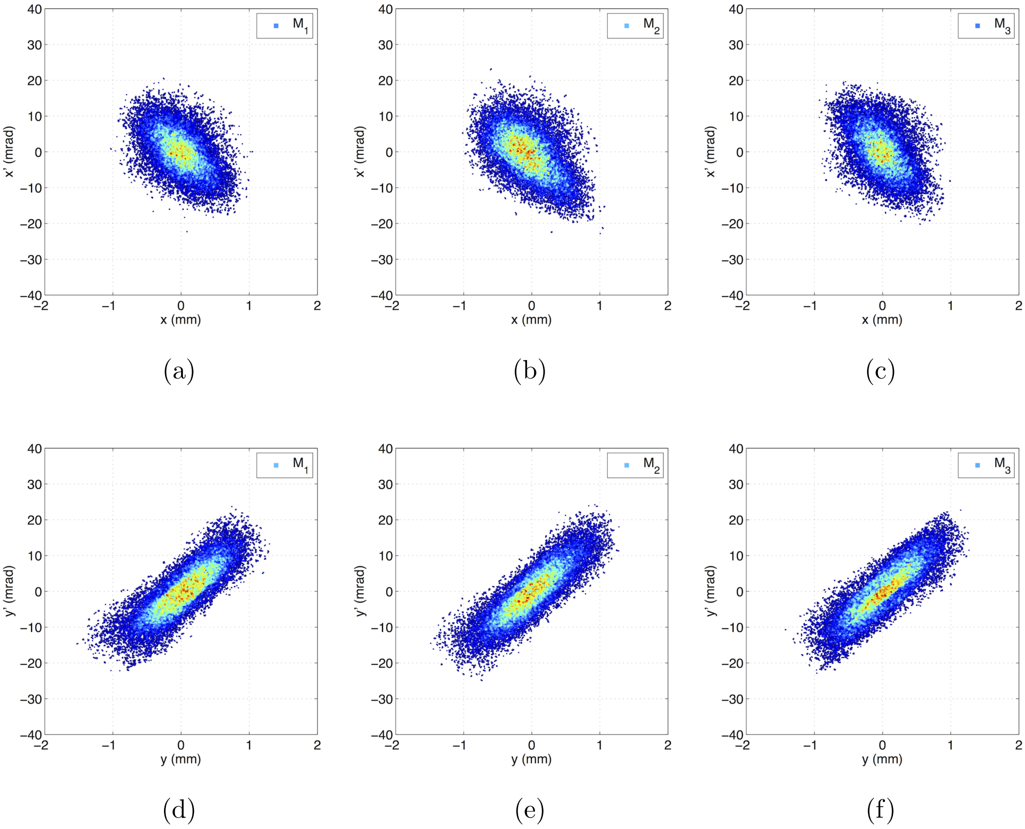

(a) (b) (c)

(d) (e) (f)

Figure 7.18. Phase space plots of the backtracked beams (first row: horizontal, second row: vertical) at the RFQ output plane.

power of the backtracking method. After backtracking, the particle distribution at the RFQ exit was obtained based on the measurements. This particle distribution can be used as an input to further beam dynamics simulations, for instance, tuning the MEBT for matching the beam to the first tank of the DTL.

The backtracked beam at the RFQ exit was compared with the beam obtained from the RFQ simulations. Figure 7.19 shows the comparison of the phase space plots of the beams from Parmteqm and backtracking (M_1 was used for the comparison). The backtracked beam has a smaller emittance, this can be partially explained by the particle losses along the MEBT line. The backtracked beam represents only the particles which could reach to the emittance meter.

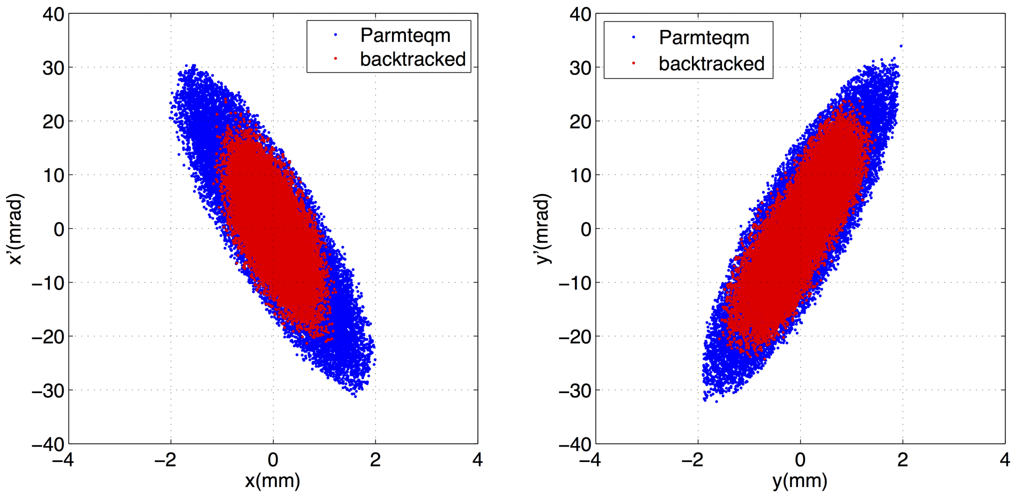

(a) (b)

Figure 7.19. Comparison of the transverse phase space plots of the beam from RFQ simulations and backtracking.

7.3.5.1. Crosschecking the Wire Scanner and Emittance Meter Results. The two wire scanners in the MEBT line will be the sole measurement devices available to investigate the transverse properties of the beam during the operation. Therefore, it was important to crosscheck the results of the wire scanner measurement with the results from another diagnostic instrument. The transverse beam sizes were measured with the two

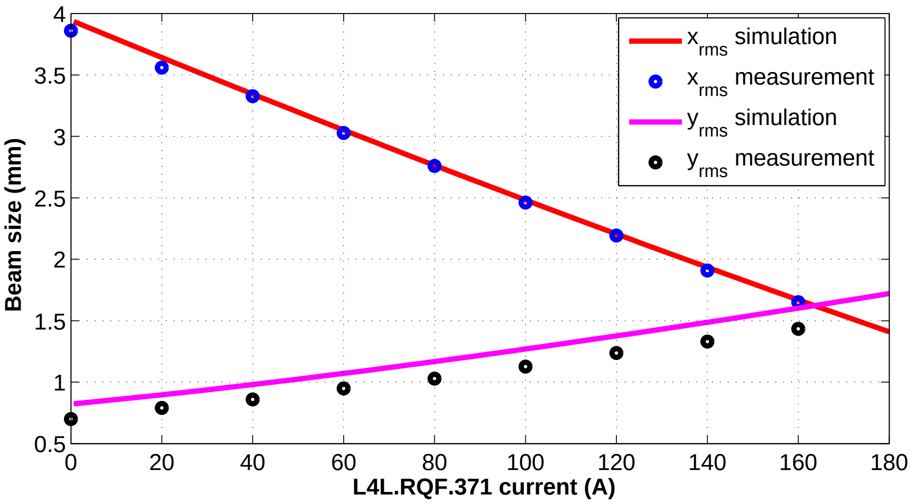

Figure 7.20. Beam size at the second wire scanner location as a function of L4L.RQF.371 current.

wire scanners while varying the current of a quadrupole magnet upstream of the wire scanner. The measurements were simulated using the backtracked beam as an input. Then, the simulation results were compared with the measurement data. Figure 7.20 shows the comparison of the transverse beam sizes on the second wire scanner as a function of L4L.RQF.371 (seventh MEBT quadruple magnet) current. The simulated and measured beam sizes were compared both at the first and second wire scanners by varying the currents of different quadruple magnets. Results showed a fair agreement between the measured and simulated beam sizes (see [35]).

7.3.5.2. Measuring the Beam Matched to the DTL. After fully characterizing the MEBT line and the beam properties, the settings of the quadrupoles and RF cavities, which match the beam to the DTL, were calculated. The currents of the MEBT quadrupoles and settings of the RF cavities were adjusted to the values found from the simulations and the beam transverse phase spaces were measured at the matching condition. Figure 7.21 shows the comparison of the transverse phase spaces from the measurement and simulation at the DTL injection plane.

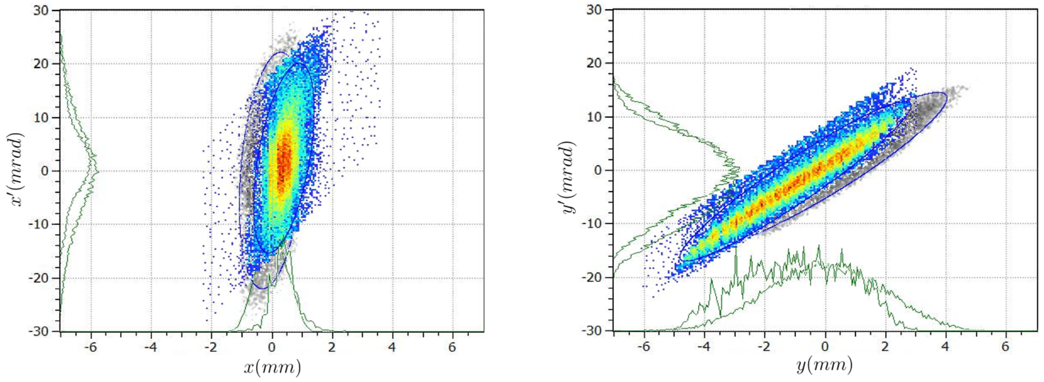

Figure 7.21. Transverse phase space plots of the beam matched to the DTL tank1 (color scale: measurement, grayscale: simulation).

8. 12 MeV COMMISSIONING STAGE

The first DTL tank, which will accelerate the beam to 12 MeV, was installed in the Linac4 tunnel in July 2014 and the diagnostic bench in Figure 7.1 was moved to the injection point of the second DTL tank [16]. Figure 8.1 shows a drawing of Linac4 during the 12 MeV commissioning stage.

The intertank between the first and second tanks of the DTL houses a Beam Position Monitor (BPM), a horizontal and vertical steering magnet and an electromagnetic quadrupole. Besides the instruments on the bench, these elements were also used during the commissioning.

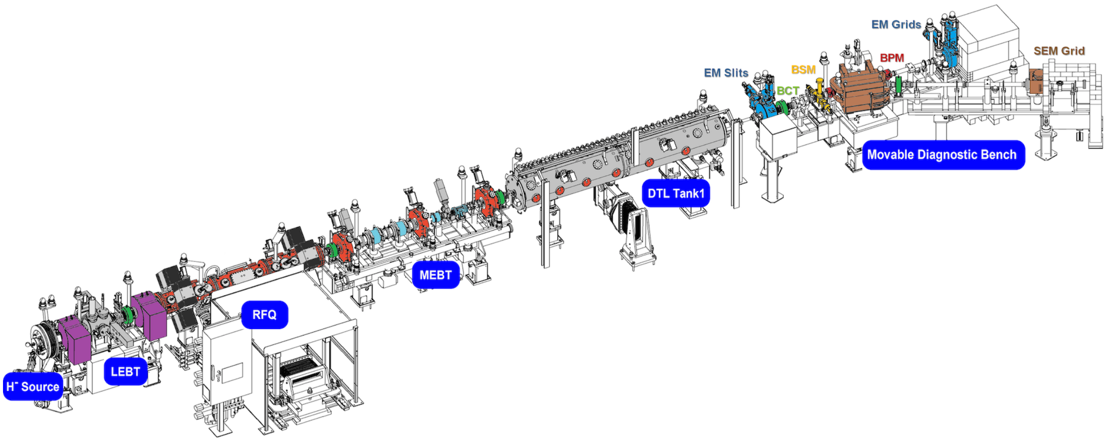

Figure 8.1. Linac4 during 12 MeV commissioning.

The main goals of the 12 MeV commissioning stage were to determine the operational values of the RF phase and the amplitude of the first DTL tank (DTL tank1), as well as to confirm the correct beam dynamics through the permanent magnet focusing system.

8.1. Setting the RF Phase with Acceptance Scans

The acceptance scan method is based on measuring the transmission through the tank as a function of RF phase. The acceptance scans were modeled with PATH by simulating the beam measured during the 3 MeV commissioning. The operational RF phase was determined by comparing the measured phase profile of transmission with the simulation results.

The DTL tank1 commissioning started with the MEBT RF cavities turned off and detuned. The cavities were turned on one by one and set to their operational phase (-90° for bunching) and amplitudes. At each step of acceptance scans, the status of the MEBT cavities were as follows:

- Step 1: All cavities were off and detuned.
- Step 2: First cavity was on, second and third cavities were off and detuned.
- Step 3: First and second cavities were on, third cavity was off and detuned.
- Step 4: All cavities were on.

For each step listed above, the MEBT quadrupoles were adjusted to satisfy the transverse matching of the beam to the DTL tank.

The longitudinal bunch size at the tank1 injection plane depends on the settings of the cavities. For each step listed above, the longitudinal phase space of the beam at the DTL entrance was compared with the longitudinal acceptance plot of tank1. Figure 8.2 shows the comparison for each case. As it can be seen in Figure 8.2a, when the MEBT cavities are off, the bucket is filled completely. The longitudinal size of the bunch gets shorter as the cavities are turned on. When all the MEBT cavities are on (Figure 8.2d), the phase space plot of the beam nicely fits into the acceptance plot of the tank.

For each MEBT cavity setting, the tank1 RF phase was scanned over a range of 360° and transmission was measured. This is similar to scanning the longitudinal acceptance plot of the tank across the phase space plot of the beam (in Figure 8.2) and counting the number of particles inside the intersection area of the two. Referring to Figure 8.2, the particles, which are outside of the longitudinal acceptance plot, will not be accelerated to the design output energy. Depending on their transverse coordinates,

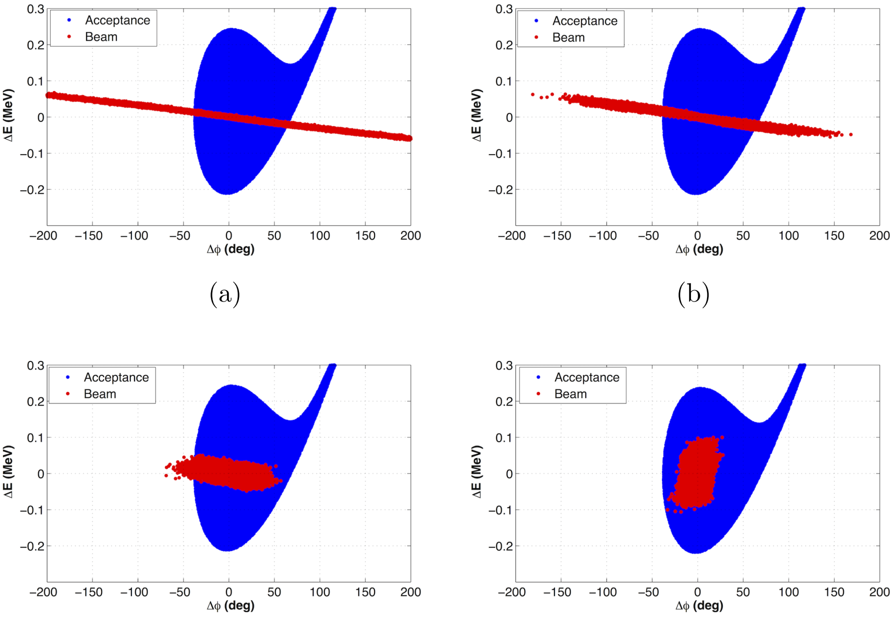

(a) (b)

(c) (d)

Figure 8.2. The comparison of longitudinal phase space plot of the injected beams and tank1 acceptance plot for (a) step 1, (b) step 2, (c) step 3 and (d) step 4.

they may be lost along the tank or they may come out but with a wrong energy and produce a tail in the longitudinal phase space. In order to clean the tail in the longitudinal phase space, an energy degrader can be used before measuring the beam current after the tank [64, 65]. This makes the measurement set-up more complicated. Instead, in Linac4, the beam current after the DTL tank was measured with a BCT without introducing a degrader. With an accurate modeling of the particle dynamics through the tank, this simple method was proved to be accurate enough to set the operational RF phase of tank1.

The comparison between the measured and expected profile of transmission from acceptance scans is given in Figure 8.3 for different settings of the MEBT cavities. As it can be seen from the plots, the measurement results agree well with what was expected from the simulations. It is worth noting that the simulation results shown in Figure 8.3 depend strongly on the input beam for the simulations and the accuracy of the dynamics calculations. Therefore, besides the accurate mechanical construction of the tank, the well described beam properties during the 3 MeV commissioning and tracking code PATH can be given credit for the agreement between the simulations and measurements at 12 MeV commissioning stage.

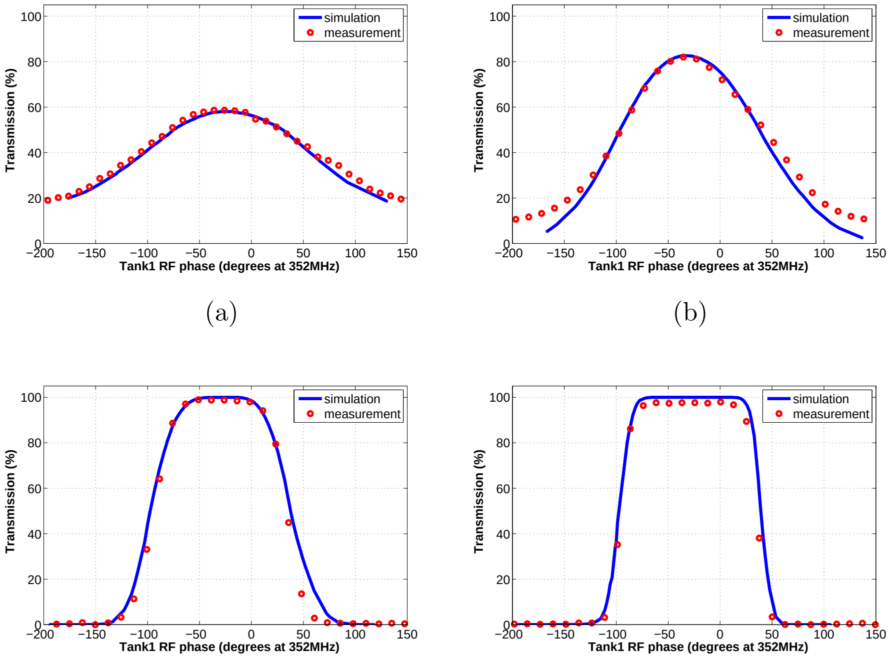

(a) (b)

(c) (d)

Figure 8.3. Simulated and measured transmission as a function of tank1 RF phase for (a) step 1, (b) step 2, (c) step 3 and (d) step 4

During the measurements, the RF amplitude of the tank was set to a value predicted to be the operational one with the RF measurements. Acceptance scans with different RF amplitudes showed that it was not possible to set the RF amplitude of the tank with an acceptable accuracy only with this method. Energy measurements with Time-of-Flight (ToF) method was used for setting the RF amplitude of the tank and confirming the RF phase setting determined by acceptance scans.

After setting the RF phase with acceptance scans, during the rest of the 12 MeV commissioning, all the MEBT cavities were kept operational at their nominal phase and amplitude.

8.2. Setting the RF Amplitude with ToF Measurements

The measurement of the tank1 output beam energy was the key for setting the RF amplitude and confirming the RF phase found by acceptance scans. The tank1 output energy was measured by ToF for different RF amplitudes by scanning the RF phase. The measured curve of energy as a function of RF phase was observed to be unique for each RF amplitude. By comparing the measured curves with the simulations, the setting of the RF phase was confirmed and the operational level of the RF amplitude was identified with an accuracy of better than ±1 per cent which is well within the static field error tolerance for the Linac4 DTL, ±2 per cent [31].

When the measurement and simulation results were compared, it was observed that, while the trend of the energy vs. tank1 RF phase curves agreed very well, the results from the measurements were consistently higher by 60keV. Figure 8.4 compares the measured curves with simulated curves for the nominal tank voltage (V_T) and the levels two per cent lower ($0.98V_T$) and five per cent above ($1.05V_T$) the nominal. As it can be seen in the figure, the transmission curve for each RF amplitude is distinct which makes it possible to identify the voltage levels.

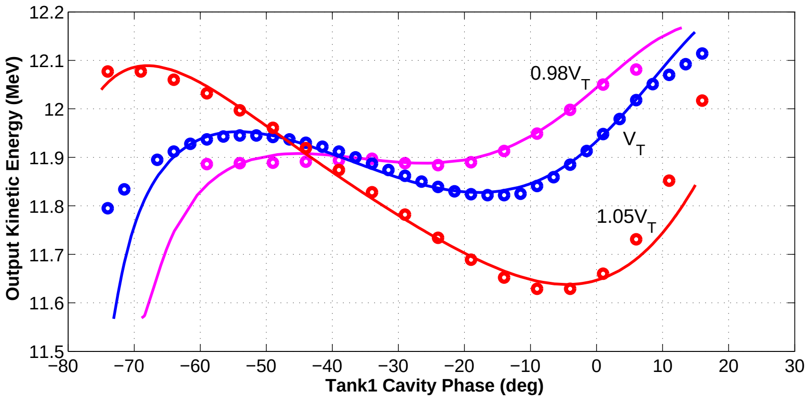

Figure 8.4. The comparison of measured (dots) and simulated (lines) kinetic energy as a function of tank1 RF phase for $0.98V_T$ (magenta), V_T (blue), $1.05V_T$ (red). The measured data are shifted by -60 keV for a better comparison of the trend.

Figure 8.5 shows the comparison of the measured and simulated curves for $0.99V_T$

V_T and $1.01V_T$. When Figures 8.4 and 8.5 are compared, it can be seen that, the curves are becoming similar for the amplitude levels which are close to each other. However, they are still distinct and easy to identify.

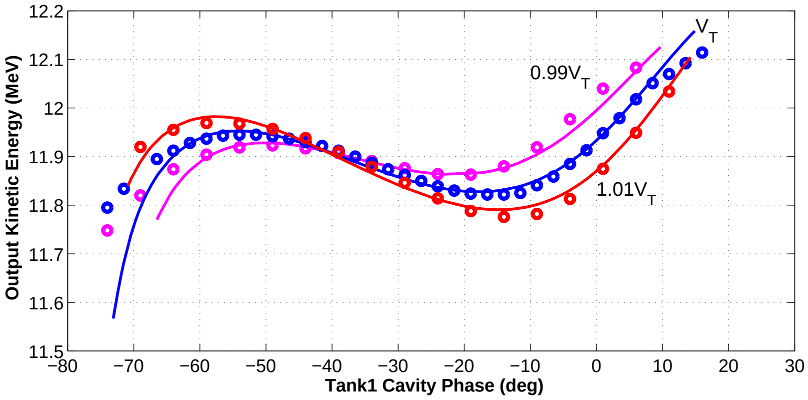

Figure 8.5. The comparison of measured (dots) and simulated (lines) kinetic energy as a function of tank1 RF phase for $0.99V_T$ (magenta), V_T (blue), $1.01V_T$ (red). The measured data are shifted by -60 keV for a better comparison of the trend.

Figure 8.6 shows the comparison of the measured and simulated curves for $0.995V_T$ V_T and $1.005V_T$. As it can be see in the figure, the curves are very close to each other and difficult to identify.

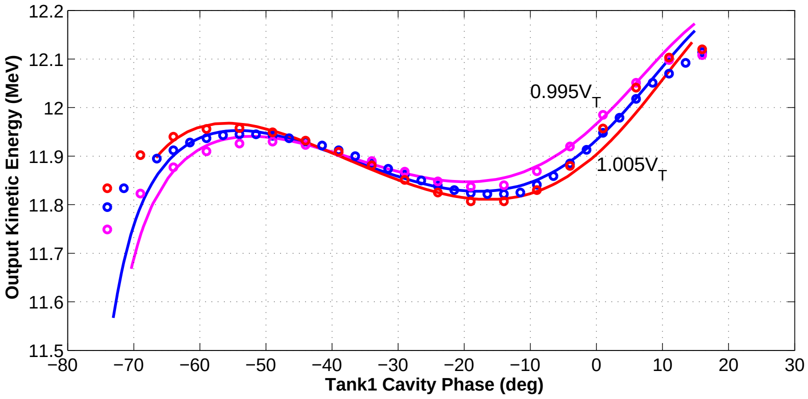

Figure 8.6. The comparison of measured (dots) and simulated (lines) kinetic energy as a function of tank1 RF phase for $0.995V_T$ (magenta), V_T (blue), $1.005V_T$ (red). The measured data are shifted by -60 keV for a better comparison of the trend.

8.3. Emittance Measurements

Extensive transverse emittance measurements were taken after tank1 with the slit-grid emittance meter, by varying the last MEBT quadrupole and the intertank quadrupole after the tank1. The measurement results agreed well with the simulations and, when the beam was matched to tank1, no emittance growth was observed through the tank. The agreement between the measurements and the simulations confirmed the correct beam dynamics design through the tank1 permanent magnet focusing channel and the calibration of the intertank quadrupole.

Figure 8.7 shows the measured and simulated phase space plots when the beam was matched to the tank.

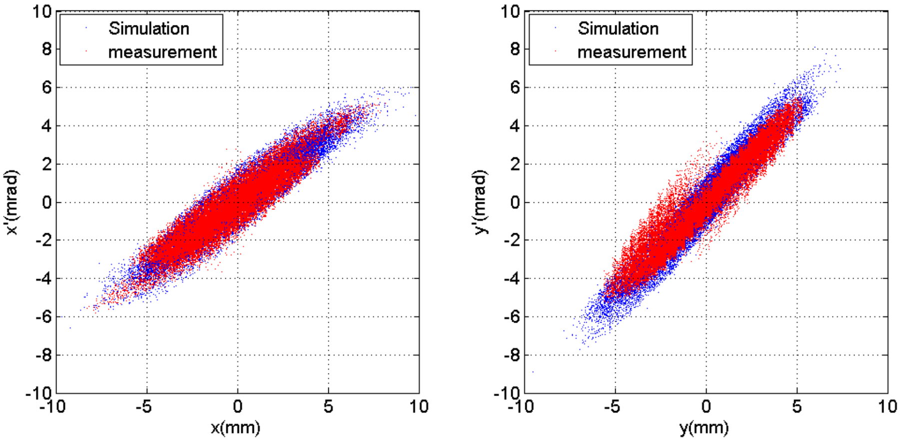

(a) (b)

Figure 8.7. The comparison of the (a) horizontal and (b) vertical phase space plots of the measured (red) and simulated (blue) beams after tank1.

8.4. Matching the Beam to Second DTL Tank

As a last step of the 12 MeV commissioning stage, the machine parameters were set to the operational values in order to match the beam to the second DTL tank. The parameters of the matched beam were confirmed with the slit-grid emittance meter, the BSM and the spectrometer. Figure 8.8 shows a comparison between the measured and simulated transverse phase space plots with an excellent agreement in orientation (the measurements were cut because of the limited angular acceptance of the emittance meter).

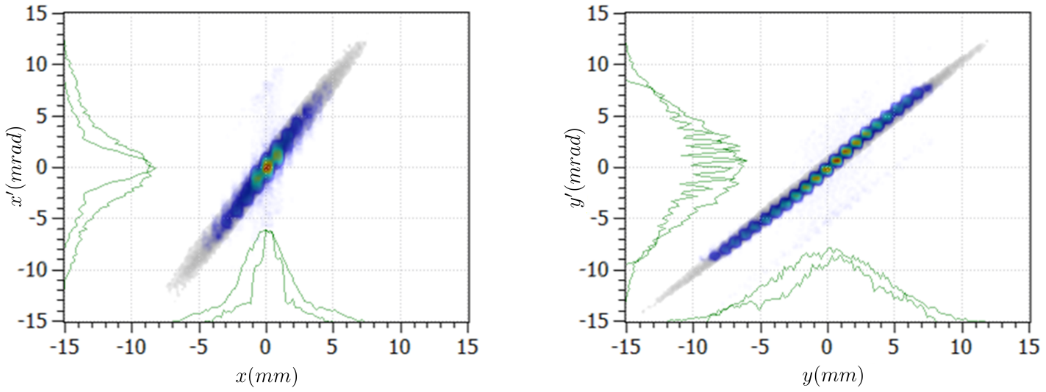

Figure 8.8. Transverse phase space plots of the beam matched to the second DTL tank (color scale: measurement, grayscale: simulation [16].

The rms energy spread and the longitudinal particle distribution of the matched beam were confirmed with the spectrometer and the BSM, respectively. Figure 8.9 shows the comparison between the measured and the simulated longitudinal particle distribution in a bunch.

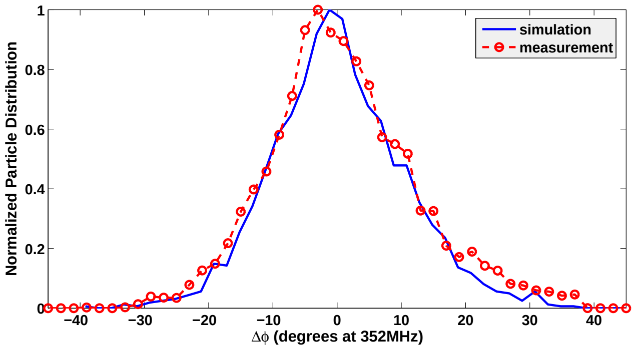

Figure 8.9. Transverse phase space plots of the beam matched to the second DTL tank (color scale: measurement, grayscale: simulation) [16].

9. CONCLUSION

The commissioning of Linac4 started at the 3 MeV test stand in 2013. After the commissioning of the 3 MeV front end, the accelerator parts were transported to their final location in the Linac4 tunnel. In November 2013, the commissioning of the linac started in the tunnel with the recommissioning of the RFQ and MEBT. By the end of 2014, the part of the linac up to 12 MeV was successfully commissioned with a temporary version of the ion source.

At each stage of the Linac4 commissioning, the beam properties were measured and their dependence on operation parameters were well understood. Based on the measurement data, multi-particle beams were generated and used as inputs for the simulations of the next commissioning stage. This process provided a good link between any two consecutive commissioning stages and facilitated the characterization of the structure being commissioned.

During the 45 keV commissioning stage, the transverse emittance of the beam was measured downstream of the first LEBT solenoid with a slit-grid emittance meter for different solenoid settings. Based on the measurement data, multi-particle beams were generated and backtracked to the source by varying the effective beam current. By comparing the backtracked beams, the calibration of the solenoids was confirmed, the space charge compensation factor in the LEBT was estimated and a particle distribution at the source exit was obtained. This particle distribution was used as an input for the simulations to determine the LEBT solenoid settings which match the beam to the RFQ.

Permanent diagnostic instruments and a movable diagnostic bench equipped with a spectrometer, a slit-grid emittance meter, a Bunch Shape Monitor and Beam Position Monitors was used for the beam commissioning at 3 MeV and 12 MeV. The bench was consecutively used after the RFQ, MEBT and the first tank of the DTL.

The goals during the 3 MeV commissioning stage were to confirm the RFQ performance, to validate the chopping system operation and to find the RF phase and amplitude setting of the MEBT cavities. The performance of the RFQ and the calibration of the RF amplitude were confirmed by varying the power in the RFQ and measuring the transmission. The correct operation of the chopping system was confirmed by measuring the transmission of the main and the chopped beam through the MEBT dump, for various settings of a quadrupole upstream of the dump. The spatial separation of the main and the chopped beams was also confirmed through the wire scanner measurements. The RF phase and the amplitude settings of each MEBT cavity were determined by varying the cavity parameters and measuring the energy gain with the spectrometer.

After the calibration of the MEBT RF cavities, the longitudinal emittance was reconstructed at the RFQ exit with the forward method. Transverse emittance measurements were taken downstream of the MEBT under different optics conditions. Multiparticle beams were generated using the measurement data, and then backtracked to the RFQ exit. The good agreement between the backtracked beams confirmed the correct calibration of the MEBT quadrupoles. Starting from the definition of the beam at the RFQ exit, the MEBT quadrupole magnet and RF cavity settings were optimized to match the beam to the DTL for the 12 MeV beam commissioning.

During the 12 MeV commissioning stage, the RF phase of the DTL tank1 was set using the acceptance scans. The kinetic energy after the tank was measured as a function of the RF phase with the Time-of-Flight method. By comparing the measurement and simulation results, the setting of the RF phase was confirmed and the operational level of the RF amplitude was identified. The beam dynamics design through DTL tank1 with the permanent magnet focusing channel was confirmed by emittance measurements.

APPENDIX A: EQUATION OF MOTION THROUGH A QUADRUPOLE MAGNET

Considering that there is no electric field and no acceleration, for a quadrupole magnet Equation 2.11 can be written as

$$\gamma_r m \frac{d\vec{v}}{dt} = q\vec{v} \times \vec{B} \tag{A.1}$$

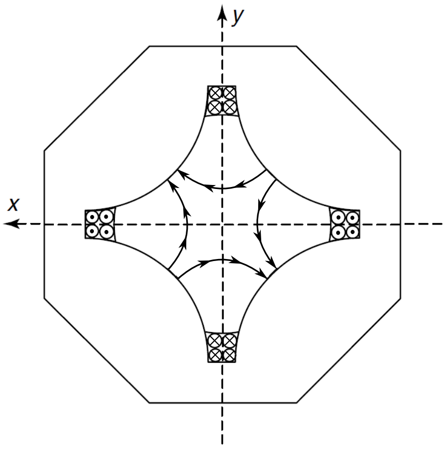

Figure A.1. A quadrupole magnet with the magnetic field pattern. Direction of z is into the page.

Figure A.1 shows a quadrupole magnet with the magnetic field pattern. The components of the field for a perfect quadrupole can be expressed as follows:

$$B_x = Gy \tag{A.2}$$

$$B_y = Gx \tag{A.3}$$

$$B_z = 0 \tag{A.4}$$

G is called quadrupole gradient and defined as $G = \frac{\partial B_x}{\partial y} = \frac{\partial B_y}{\partial x}$. Taking into account the field direction and strength, the equation of motion in the transverse planes can be written as in Equations A.5 and A.6.

$$\begin{aligned} \gamma_r m \frac{d^2x}{dt^2} &= -qv_zGx && \text{(A.5)} \\ \gamma_r m \frac{d^2y}{dt^2} &= qv_zGy && \text{(A.6)} \end{aligned}$$

One is simply interested in how the coordinates of the particles change along the accelerator. Therefore, it is more practical to use dz as an independent variable instead of dt. The first and second time derivative of x can be expressed as in the following equations.

$$\begin{aligned} \dot{x} &= \frac{dx}{dz}\frac{dz}{dt} = x'\dot{z} && \text{(A.7)} \\ \ddot{x} &= \dot{x}'\dot{z} + x'\ddot{z} = x''\dot{z}^2 + x'\ddot{z} && \text{(A.8)} \end{aligned}$$

Assuming that the velocity variation through the quadrupole magnet is very slow we can write $\ddot{z} \approx 0$. This simplifies Equation A.8 as in Equation A.9. Notice that the same equations hold also for y.

$$\ddot{x} = x''\dot{z}^2 \tag{A.9}$$

Inserting Equation A.9 into Equation A.5, equation of motion in horizontal plane can be expressed as in Equation A.10. Likewise, in vertical plane it can be written as in Equation A.11.

$$\begin{aligned} x'' + \frac{qG}{\gamma_r m v_z}x &= 0 && \text{(A.10)} \\ y'' - \frac{qG}{\gamma_r m v_z}y &= 0 && \text{(A.11)} \end{aligned}$$

By introducing a new variable k as in Equation A.12 the Equations A.10 and A.11 can be rewritten as in Equations A.13 and A.14

$$k^2 \equiv \left| \frac{qG}{\gamma_r m v_z} \right| \tag{A.12}$$

$$\begin{aligned} x'' + k^2 x &= 0 && \text{(A.13)} \\ y'' - k^2 y &= 0 && \text{(A.14)} \end{aligned}$$

REFERENCES

1. https://cds.cern.ch/record/1260465, *CERN PhotoLab*, July 2015.

2. Charmot, H., C. Dutriat, C.E. Hill, K. Langbein, A.M. Lombardi, M. O'Neil, E. Tanke and M. Vretenar, "Operational Experience with the CERN Hadron Linacs", *Proceedings of Linac1996*, Geneva, 1996.

3. Benedikt, M., P. Collier, V. Mertens, J. Poole and K. Schindl (editors), "LHC Design Report, Volume III, The LHC Injector Chain", *CERN Internal Notes*, CERN-2004-003-V-3, Geneva, 2004.

4. Gerigk, F. and M. Vretenar (editors), "Linac4 Technical Design Report", *CERN Internal Notes*, CERN-AB-2006-084 ABP/RF, Geneva, 2006.

5. Mahner, E., "Risk Analysis for Linac2 Vacuum System", *CERN Internal Notes*, ATS/Note/2011/051, Geneva, 2011.

6. Garoby, R. and M. Vretenar, "Status of the Proposal for a Superconducting Proton Linac at CERN", *CERN Internal Notes*, CERN-PS-99-064-RF, Geneva, 1999.

7. Vretenar, M. (editor), "Conceptual Design of the SPL, a High-power Superconducting H^- linac at CERN", *CERN Internal Notes*, CERN-2000-012, Geneva, 2000.

8. Benedikt, M, K. Cornelis, R. Garoby, E. Méteral, F. Ruggiero and M. Vretenar, "Report of the High Intensity Protons Working Group", *CERN Internal Notes*, CERN-AB-2004-022 OP/RF, Geneva, 2004.

9. Lombardi, A.M., "CERN Linac Upgrade Activities", *Proceedings of Linac2008*, Victoria, 2008.

10. Arnaudon, L., P. Baudrenghien, C. Bertone, Y. Body, J. Broere, O. Brunner, M. Buzio, C. Carli, F. Caspers, J.P. Corso, J. Coupard, A. Dallocchio, N. Dos Santos,

R. Garoby, F. Gerigk, L. Hammouti, K. Hanke, M. Jones, I. Kozsar, J. Lettry, J.B. Lallement, A. M. Lombardi, L.A. Lopez- Hernandez, C. Maglioni, S. Mathot, S. Maury, B. Mikulec, D. Nisbet, C. Noels, M. Paoluzzi, B. Puccio, U. Raich, S. Ramberger, C. Rossi, N. Schwerg, R. Scrivens, G. Vandoni, S. Weisz, J. Vollaire, M. Vretenar and T. Zickler, “The Linac4 Project at CERN”, *Proceedings of IPAC2011*, San Sebastiaán, 2011.

11. Lettry, J., D. Aguglia, P. Andersson, S. Bertolo, A. Butterworth, Y. Coutron, A. Dallocchio, E. Chaudet, J. Gil-Flores, R. Guida, J. Hansen, A. Hatayama, I. Koszar, E. Mahner, C. Mastrostefano, S. Mathot, S. Mattei, Ø. Midttun, P. Moyret, D. Nisbet, K. Nishida, M. ONeil, M. Ohta, M. Paoluzzi, C. Pasquino, H. Pereira, J. Rochez, J. Sanchez Alvarez, J. Sanchez Arias, R. Scrivens, T. Shibata, D. Steyaert, N. Thaus, and T. Yamamoto, “Status and Operation of the Linac4 Ion Source Prototypes”, *Review of Scientific Instruments*, Vol. 85, No. 02B122, 2014.

12. Rossi, C., P. Bourquin, S. Cazaux, O. Delferriere, M. Desmons, R. Duperrier, A. France, J-B. Lallement, D. Leboeuf, A. M. Lombardi, S. Mathot, O. Piquet, M. Timmins, G. Vandoni and M. Vretenar, “The Radio Frequency Quadrupole Accelerator for the Linac4”, *Proceedings of Linac2008*, Victoria, 2008.

13. Caspers, F., Y. Cuvet, J. Genest, M. Haase, M. Paoluzzi and A. Teixeira, “The CERN-SPL Chopper Concept and Final LAyout”, *CERN Internal Notes*, CERN-AB-2004-049, Geneva, 2004.

14. Ramberger, S., P. Bourquin, Y. Cuvet, A. Dallocchio, G. De Michele, F. Gerigk, J.M. Giguet, J.B. Lallement, A.M. Lombardi, E. Sargsyan and M. Vretenar, “Production Design of Drift Tube Linac for the CERN Linac4”, *Proceedings of Linac2010*, Tsukuba, 2010.

15. Favre, G., A. Cherif, A. Dallocchio, J.M. Geisser, L. Gentini, F. Gerigk, S. Mathot, M. Polini, S. Sgobba, T. Tardy and R. Wegner, “Manufacturing the Linac4 Pi-Mode Structure Prototype at CERN”, *Proceedings of IPAC2011*, San Sebastián, 2011.

16. Dimov, V. A., E. Belli, G. Bellodi, J.B. Lallement, A. M. Lombardi, M. Yarmohammadi Satri, “Beam Commissioning of Linac4 up to 12 MeV”, *Proceedings of IPAC2015*, Richmond, 2015.

17. Vretenar, M., A. Akroh, L. Arnaudon, P. Baudrenghien, G. Bellodi, J. Broere, O. Brunner, J.F. Comblin, J. Coupard, V.A. Dimov, J.F. Fuchs, A. Funken, F. Gerigk, E. Granemann Souza, K. Hanke, J. Hansen, I. Kozsar, J.B. Lallement, F. Lenardon, J. Lettry, A.M. Lombardi, C. Maglioni, Ø Midtun, B. Mikulec, D. Nisbet, M. Paoluzzi, U. Raich, S. Ramberger, F. Roncarolo, C. Rossi, J.L. Sanchez Alvarez, R. Scrivens, J. Tan, C.A. Valerio- Lizarraga, J. Vollaire, R. Wegner, S. Weisz, M. Yarmohammadi Satri and F. Zocca, “Status and Plans for LINAC4 Installation and Commissioning”, *Proceedings of IPAC2014*, Dresden, 2014.

18. Wangler, T. P., *RF Linear Accelerators*, 2nd edition, WILEY-VCH, Weinheim, 2008.

19. Crandall, K. R. and D. P. Rusthoi, “TRACE 3-D Documentation”, *LANL Internal Notes*, LA-UR-97-886, Los Alamos, 1997.

20. Lapostolle, P. M., “Quelques Proprietes Essentielles des Effets de la Charge D’espace dans de Faisceaux Continus”, *CERN Internal Notes*, CERN-ISR/DI-70-36 Geneva, 1970.

21. Sacherer, F. J., “RMS Envelope Equation with Space Charge”, *CERN Internal Notes*, CERN-SI/DL-70-12 Geneva, 1970.

22. Buon, J., “Beam Phase Space and Emittance”, *CERN Accelerator School Lecture Notes*, pp.30-52, Jülich, 1990.

23. Wiedemann, H., *Particle Accelerator Physics*, 3rd edition, Springer-Verlag, Berlin, 2007.

24. Wille, K., *The Physics of Particle Accelerators*, Oxford University Press , Oxford,

2000.

25. Crandall, K. R., T. P. Wangler, L. M. Young, J. H. Billen, G. H. Neuschaefer and D. L. Schrage, “RFQ Design Codes”, *LANL Internal Notes*, LA-UR-96-1836, Los Alamos, 2005.

26. Uriot, D., “TraceWin documentation”, *CEA/SACLAY Internal Notes*, Saclay, 2012.

27. Perrin, A., J.F. Amand, T. Mutze, J.B. Lallement, and S. Lanzone, “TRAVEL v4.07: User Manuel”, *CERN Internal Notes*, Geneva, 2007.

28. Mutze, T. and S. Lanzone, “Delta: User Manual”, *CERN Internal Notes*, Geneva, 2007.

29. Stovall. J and K. Crandall, “Quadrupole Law and Steering Options in the Linac4 DTL”, *CERN Internal Notes*, sLHC-Project-Note-0006, Geneva, 2009.

30. Dimov, V. and A. Lombardi, “Linac4 Transverse and Longitudinal Acceptance Studies”, *CERN Internal Notes*, CERN-ATS-Note-2013-020 TECH, Geneva, 2013.

31. Bellodi, G., M. Eshraqi,M. Garcia Tudela, L. Hein, J.B. Lallement, S. Lanzone, A.M. Lombardi, P. Posocco and E. Sargsyan, “Alignment and Field Error Tolerance in Linac4”, *CERN Internal Notes*, CERN-ATS-Note-2011-021, Geneva, 2011.

32. Kalvas, T., O. Tarvainen, T. Ropponen, O. Steczkiewicz, J. Arie and H. Clark, “IBSIMU: A Three-dimensional Simulation Software for Charged Particle Optics”, *Review of Scientific Instruments*, Vol. 81, No. 02B703, 2010.

33. Lallement, J.B., A. Akroh, G. Bellodi, J.F. Comblin, V.A. Dimov, E. Granemann Souza, J. Lettry, A.M. Lombardi, Ø. Midttun, E. Ovalle, U. Raich, F. Roncarolo, C. Rossi, J.L. Sanchez Alvarez, R. Scrivens, C.A. Valerio-Lizarraga, M. Vretenar and M. Yarmohammadi Satri, “First Commissioning Experience with the LINAC4 3MeV Front-end at CERN”, *Proceedings of PAC2013*, Pasadena, 2013.

34. Lombardi, A.M., “Commissioning of the Low-energy part of LINAC4”, *Proceedings of LINAC2014*, Geneva, 2014.

35. Yarmohammadi Satri, M., G. Bellodi, V. Dimov, J.B. Lallement, A. Lombardi, U. Raich, F. Roncarolo and F. Zocca, “Transverse Beam Profile Measurements in the LINAC4 Medium Energy Beam Transport”, *Proceedings of LINAC2014*, Geneva, 2014.

36. Malament, D. B., “On the Time Teversal Invariance of Classical Electromagnetic Theory”, *Studies in History and Philosophy of Modern Physics*, Vol. 35, pp. 295-315, 2004.

37. Erman, J., “What Time Reversal Invariance Is and Why It Matters”, *International Studies in the Philosophy of Science*, Vol. 16, No. 3, 2002.

38. Wilhelm. P. and E. Lohrmann, “Rounding Errors in Beam-tracking Calculations”, *Workshop on Orbital Dynamics and Applications to Accelerators*, Berkeley, 1985.

39. Raich, U., “Beam Diagnostics”, *CERN Accelerator School Lecture Notes*, pp.503-514, Senec, 2012.

40. Forck, P., “Lecture Notes on Beam Instrumentation and Diagnostics”, *Joint Universities Accelerator School*, Archamps, 2011.

41. http://cds.cern.ch/record/834935, *CERN PhotoLab*, November 2014.

42. Harasimowicz, J., *Development of Instrumentation for Low Energy Beams*, Ph.D. Thesis, University of Liverpool, 2013.

43. Tan, J., M. Sordet and L. Søby, “Beam Position Monitor System for the CERN LINAC4”, *Proceedings of DIPAC2011*, Hamburg, 2011.

44. Bellodi G., A. Akroh, O. Andreassen, J-F. Comblin, V. Dimov, J-B. Lallement, A. M. Lombardi, C. Martin, Ø. Midttun, E. Ovalle, U. Raich, F. Roncarolo, C. Rossi,

J-L. Sanchez Alvarez, R. Scrivens, J. Vollaire, M. Yarmohammadi Satri and F. Zocca, “3 MeV Test Stand Commissioning Report”, *CERN Internal Notes*, CERN-ACC-2013-0259, Geneva 2013.

45. Zocca, F., E. Bravin, M. Duraffourg, G. J. Focker, D. Gerard, U. Raich and F. Roncarolo, “Profile and Emittance Measurements at the CERN LINAC4 3MeV Test Stand”, *Proceedings of IBIC2013*, Oxford, 2013.

46. Zocca, F., J. C. Allica Santamaria, M. Duraffourg, A. Feshenko, G. J. Focker, D. Gerard, B. Kolad, F. Lenardon, M. Ludwig, U. Raich, F. Roncarolo, M. Sordet, J. Tan, J. Tassan-Viol and C. Vuitton, “Beam Diagnostics Measurements at 3MeV of the LINAC4 H^- Beam at CERN”, *Proceedings of IPAC2014*, Dresden, 2014.

47. Cheymol B., E. Bravin, C. Dutriat, A. Lokhovitsky, U. Raich, F. Roncarolo, R. Scrivens and E. Zorin, “Commissioning of the LINAC4 Ion Source Transverse Emittance Meter”, *CERN Internal Notes*, CERN-BE-2010-014 BI, Geneva 2010.

48. Lallement, JB., A. Lombardi and PA. Posocco, “Emittance Reconstruction Technique for the Linac4 High Energy Commissioning”, *CERN Internal Notes*, CERN-ATS-Note-2012-079 MD, Geneva, 2012.

49. Feschenko, A., V. Gaidash, Y. Kisselev, L. Kravchuk, A. Liyu, A. Menshov, A. Mirzojan, S. Assadi, W. Blokland, S. Henderson, D. O. Jeon and E. Tanke, “The First Results of Bunch Shape Measurements in the SNS Linac”, *Proceedings of LINAC2004*, Lübeck, 2004.

50. Ceymol, B., J.B. Lallement, A. Lokhovitsky, Ø. Midttun, U. Raich, F. Roncarolo, R. Scrivens and E. Zorin, “First Results from Beam Measurements at the 3MeV Test Stand for CERN LINAC4”, *Proceedings of DIPAC2011*, Hamburg, 2011.

51. Hein, L. M., G. Bellodi, J-B. Lallement, A. M. Lombardi, Ø. Midttun, P. Posocco and R. Scrivens “LINAC4 Low Energy Beam Measurements”, *Proceedings of IPAC2012*, New Orleans, 2012.

52. Bellodi, G., V. A. Dimov, L. M. Hein, J-B. Lallement, A. M. Lombardi, Ø. Midttun, P. A. Posocco and R. Scrivens “LINAC4 45 keV Proton Beam Measurements”, *Proceedings of LINAC2012*, Tel-Aviv, 2012.

53. Hein, L. M., *CERN Linac4 - The Space Charge Challenge*, Ph.D. Thesis, Humboldt-Universität zu Berlin, 2013.

54. Baconnier, Y., A. Poncet and P. Tavares, “Neutralisation of Accelerator Beams by Ionisation of the Residual Gas”, *CERN Internal Notes*, CERN/PS 94-40(LP),Geneva, 1995.

55. BenIsmaïl, A., R. Duperrier and D. Uriot, “Space Charge Compensation in Low Energy Proton Beams”, *Proceedings of LINAC2004*, Lübeck, 2004.

56. Valerio-Lizarraga, C. A., J-B. Lallement, I. Leon-Monzon, J. Lettry, Ø. Midttun and R. Scrivens, “Space Charge Compensation in the Linac4 Low Energy Beam Transport Line with Negative Hydrogen Ions”, *Review of Scientific Instruments*, Vol. 85, No. 02A505, 2014.

57. Valerio-Lizarraga, C. A., R. Scrivens and N. Chauvin, “Space Charge Compensation in Linac4 LEBT for Three Injected Gas Type”, *Proceedings of LINAC2014*, Geneva, 2014.

58. Guyard, J. and M. Weiss, “Use of Beam Emittance Measurements in Matching Problems”, *Proceedings of LINAC1976*, Chalk River, 1976.

59. Batygin, Y. K., C. Pillai and L. J. Rybarcyk, “Space-charge Neutralization of 750 keV H^- Beam at LANSCE”, *Proceedings of IPAC2014*, Dresden, 2014.

60. Scrivens, R., G. Bellodi, O. Crettiez, V. Dimov, D. Gerard, E. Granemann Souza, R. Guida, J. Hansen, J.-B. Lallement, J. Lettry, A. Lombardi, Ø. Midttun, C. Pasquino, U. Raich, B. Riffaud, F. Roncarolo, C. A. Valerio-Lizarraga, J. Wallner, M. Yarmohammadi Satri and T. Zickler “Linac4 Low Energy Beam Measure-

ments with Negative Hydrogen Ions", *Review of Scientific Instruments*, Vol. 85, No. 02A729, 2014.

61. Lallement, J.B., G. Bellodi, M. Eshraqi, M. Garcia Tudela, A.M. Lombardi, P. A. Posocco, E. Sargsyan and J. Stovall, "Linac4 Commissioning Strategy", *Proceedings of HB2010*, Morschach, 2010.

62. Lallement, J.B., G. Bellodi, V. A. Dimov, A.M. Lombardi and M. Yarmohammadi Satri, "Linac4 Transverse and Longitudinal Emittance Reconstruction in the Presence Space Charge", *Proceedings of Linac2014*, Geneva, 2014.

63. Bellodi, G., V.A. Dimov, J-B. Lallement, A.M. Lombardi, U. Raich, F. Roncorolo, M. Yarmohammadi Satri and F. Zocca, "Longitudinal Beam Profile Measurements in Linac4 Commissioning", *Proceedings of Linac2014*, Geneva, 2014.

64. Jeon, D., K. Crandal, R. Shafer and J. Stovall, "Longitudinal Tune-up of SNS Normal Conducting Linac", *Proceedings of Linac2002*, Gyeongju, 2002.

65. Cheymol, B. and E. Lundh, "Conceptudal Design of the ESS DTL Faraday Cup", *Proceedings of Linac2014*, Geneva, 2014.